LASER SPECTROSCOPIC STUDIES OF EUROPIUM-DOPED GLASSES AND EMERALD

By

GREGORY JAMES QUARLES

Bachelor of Science in Arts and Science
Oklahoma State University
Stillwater, Oklahoma
1983

Master of Science
Oklahoma State University
Stillwater, Oklahoma
1985

Submitted to the Faculty of the Graduate College
of the Oklahoma State University
in partial fulfillment of the requirements
for the Degree of
DOCTOR OF PHILOSOPHY
December, 1987

LASER SPECTROSCOPIC STUDIES OF

EUROPIUM-DOPED GLASSES

AND EMERALD

Thesis Approved:

Richard C. Powell
Thesis Adviser

[signature]

[signature]

[signature]

[signature]

Norman N. Durham
Dean of the Graduate College

ACKNOWLEDGMENTS

I would like to express my appreciation to all the people responsible for helping me during my studies at Oklahoma State University. Foremost among these is my thesis adviser, Dr. Richard C. Powell. I would like to thank him for giving me the chance to learn and work in his laboratory as both an undergraduate and graduate student, and also for his advice, support and encouragement. I would also like to thank the other members of my committee, Dr. William A. Sibley, Dr. George S. Dixon, Dr. Stephen W. McKeever, and Dr. Donald L. Thompson. I would also like to acknowledge my research adviser at the Air Force Weapons Laboratory, Dr. Mark A. Kramer. Special thanks are extended to my good friends, Dr. Andrzej Suchocki and Guy Gilliland, for their assistance in acquiring parts of the data and mostly for sharing their knowledge through insightful discussions. Further, I would like to thank Mrs. Dee Behrens for her expert typing of this thesis.

My thanks and love go to the people who have provided their love and support constantly, my parents, family, friends, and God. Finally, this work would not be complete if it were not for the love of the two most precious people in my life, my wife Connie and our son Brandon. My thanks especially go to Connie for she has provided me with the strength to finish this degree through her support, encouragement and patience.

Financial support for my graduate studies was provided by the Air Force Weapons Laboratory Graduate Research Fellowship Program.

Financial support for the research was provided by the U. S. Army Research Office under contract #DAAG 29-85-k-0056 and Rome Air Development Center under contract #19628-86-C-0138. The samples for this work were provided by Allied Corporation, Rome Air Development Center and Lawrence Livermore National Laboratory.

TABLE OF CONTENTS

LIST OF TABLES

LIST OF FIGURES

CHAPTER I

INTRODUCTION

For the past two decades the development and use of lasers as a scientific tool has expanded rapidly. More recently, there has been a growing trend to use a variety of different laser spectroscopy techniques to develop a better insight into the overall electro-optical properties of materials. In particular, the use of lasers has provided a better understanding of the spectroscopic properties of solids, including the study of higher-energy electronic states, multiphoton processes, fast radiationless decay processes, and energy migration. Characterizing these processes is important from both a basic science and a technological viewpoint, because obtaining information about the basic physical properties of solids leads to a better understanding of a materials technological applicability. The work presented in this thesis makes use of laser spectroscopy to characterize the optical properties of solids.

Statement of the Problem

The problem investigated here involves using distinctly different experimental techniques to investigate two types of materials. However, the overall motivation is the same; to investigate and characterize the optical properties of these samples through laser spectroscopy. The first type of material examined includes samples of oxide and heavy

metal fluoride glasses doped with trivalent europium. These glasses can be used as fibers for transmitting optical information. The research centers around time-resolved spectroscopy to obtain information about the two-photon absorption transitions and the radiative and radiationless decay processes occurring after high-power, picosecond-pulse excitation.

The second part of this thesis includes the study of energy transfer in a crystal of synthetic emerald, heavily doped with trivalent chromium. Characterizing spectral dynamics such as energy transfer is particularly important in materials, such as emerald, having potential applications in solid state lasers. Energy transfer can be either a benefit- or a loss-mechanism; it can enhance laser performance by increasing the pumping efficiency of the active ions or it can decrease the efficiency through concentration quenching mechanisms. Thus, in both of these studies, laser spectroscopy is used to characterize materials with present and potential uses in high-technology applications.

Summary of Thesis

The second chapter of this thesis will describe the results of multiphoton spectroscopy using high-power, picosecond-pulsed excitation in the Eu^{3+} doped fluoride glass. This work includes the use of the Judd-Ofelt (1,2) analysis of the optical spectra to determine the branching ratios, nonradiative and radiative decay rates, as well as calculations of the two-photon absorption cross-sections. This work extends previous research of this type performed on Nd^{3+}-doped crystalline and glass materials (3-5). There are two major differences from the previous case. The first difference involves the initial and final states of

the multiphoton transition. For Eu^{3+}, the final state is a broad band with different parity from the initial state, whereas, for Nd^{3+}, the final state is a narrow band with the same parity as the initial state. The change in parity for the Eu^{3+} transition provides an insight into the selection rules which suggest that in this case there is a more highly allowed transition. This is reflected in a larger value for the Eu^{3+} two-photon absorption (TPA) cross-section than those found previously for Nd^{3+}. The second difference involves the intermediate state of the transition and it's role in the determination of the TPA cross-section. For Eu^{3+} the intermediate state is the metastable $^5D_1$ level, whereas for Nd^{3+} this state was not metastable and the cross-section was dependent upon the fast, nonradiative decay of the state. However, for Eu^{3+} in this fluoride glass, it was necessary to include the possibilities of a virtual transition through a nearby, nonresonant, intermediate state as well as a real intermediate state. It was determined that for this case the cross-section is dependent upon the dephasing time of the intermediate state and not on the longer lifetime associated with the fluorescence decay from a metastable state. The results of the TPA spectroscopy for Eu^{3+} in the fluoride glass are then compared with those for Eu^{3+} in the oxide glass host.

Chapter III describes the results of the characterization of the optical properties of emerald using four-wave mixing (FWM) and time-resolved site-selection spectroscopy (TRSSS) techniques. The transfer of electronic excitation energy among Cr^{3+} ions was studied using these two complimentary experimental techniques. The FWM spectroscopy probes the spatial energy migration, and the TRSSS probes the spectral energy transfer. The first part of Chapter III describes the details of the

basic spectroscopy of emerald, including fluorescence, absorption and fluorensence lifetime versus temperature studies, as well as a discussion of the crystal structure. The second part of the chapter describes the models of energy transfer used in the evaluation of the time-resolved, site-selection spectroscopy (TRSSS) data, including details of the Chow-Powell (6) theory, which is shown to be a more relevant model than that of Yokota-Tanimoto (7). The mechanisms for spectral energy transfer are then analyzed by using two methods; one involves monitoring the decay kinetics of the intensity in time and the second uses a rate-equation fit of the time dependence of the ratios of the integrated intensities of the activator and sensitizer fluorescence. The next part of the chapter describes the FWM experiment in which two strong pump beams write a holographic grating in the crystal, and a weaker probe beam reads this grating. The write beams resonantly pump a Cr^{3+} absorption band, and the interference of these two beams establishes a population grating. By studying the time evolution of the grating decay, important information can be obtained about the spatial energy migration. The grating decay curves are evaluated using Kenkre's model (8) for partially-coherent exciton migration, and the results show a long range migration process exists in emerald.

Included in Chapter III is a description of a study of relative scattering efficiency of the FWM signal. The FWM signal efficiency versus crossing angle provides important information about the contribution to the laser-induced grating from the modulation of the absorption and dispersion components of the complex refractive index. The analysis of this data is made using a simple two-level model for the atomic system.

The results of this analysis also provide information about the dephasing time of the excited state.

Finally, a summary and comparison of results obtained through TRSSS and FWM on emerald is given at the end of Chapter III.

Chapter IV presents the summary and conclusions for the material given in this thesis. Included in this chapter are suggestions for future work that needs to be undertaken to arrive at a better understanding of the physical processes taking place in both the glass and emerald samples. Finally, an appendix is included that gives a more complete development and summary of the Judd-Ofelt analysis for electric dipole, magnetic dipole and electric quadrupole transitions in rare-earth doped solids.

CHAPTER II

MULTIPHOTON SPECTROSCOPY OF Eu^{3+}-DOPED FLUORIDE AND OXIDE GLASSES

Introduction

Time-resolved spectroscopy, using high-power, picosecond-pulse excitation, has been shown to be an important technique for studying the spectral dynamics of trivalent rare earth ions in solids (3-5,9-13). Reported in this chapter are the results of a detailed investigation of the spectroscopic properties of BZLT fluoride glass doped with Eu^{3+} ions using the picosecond pulses from the primary and various harmonics of the output of a Nd:YAG laser as the source of excitation. In addition, similar measurements were made on Eu^{3+}-doped lithium phosphate (LP) oxide glass to determine the effects of the host lattice on the spectroscopic properties with this type of excitation. The time-resolved fluorescence spectra, fluorescence lifetimes, and risetimes were measured as a function of laser power for the various excitation frequencies. The spectral properties are analyzed in terms of single- and two-photon absorption processes and fluorescence from four different metastable states. These results are especially interesting since little spectroscopic work has been reported on rare earth ions in this type of fluoride glass host. The results obtained on the oxide glass

differ greatly from those obtained on the fluoride glass due the higher efficiency of radiationless decay in the former type of material.

Attempts to excite fluorescence of the BZLT:Eu^{3+} glass with multiphoton absorption of the primary 1064 nm radiation were unsuccessful. The doubled output at 532.0 nm resulted in single-photon absorption to the $^5D_1$ level and two-photon absorption into the 5d configuration band for this sample. The quadrupled output at 266.0 nm results in single photon absorption into the 5d configuration band of this sample and no observed two-photon absorption. The tripled output at 354.7 nm gives a single-photon absorption into the 5d configuration band followed by multiphoton absorption above the band edge of the fluoride sample. For the oxide host, essentially no multiphoton processes were detected for any of the different excitation conditions. For the doubled, tripled, and quadrupled Nd-YAG laser excitation, the observed fluorescence of LP:Eu^{3+} originated almost entirely from the $^5D_0$ metastable state with very little higher energy emission even for the u.v. pumping. The fluorescence spectra and lifetimes observed with the various pumping wavelengths are described in the following sections.

These results on two-photon absorption processes in Eu^{3+} ions are significantly different than those reported previously for Nd^{3+}. This is due to the fact that the initial and final states of the transition are of the same parity in the latter case but not in the former one, and thus different types of intermediate states play an important role. Also, the final state for the two types of ions are different. For Eu^{3+} the final state is the broad band 5d configurational band, whereas for Nd^{3+}, the final state is the $^2(F2)_{5/2}$ metastable state, which is much

narrower. This gives rise to a smaller density of final states for Nd^{3+}, and this gives rise to a larger TPA cross-section for Eu^{3+}.

The nomenclature for different types of multiphoton absorption processes has become somewhat confusing. In this work we use STEP to refer to a sequential two-photon excitation process in which the first photon causes a transition to a real intermediate state and before relaxation can occur the second photon excites the ion from this state to a higher state. VTEP is used for virtual two-photon excitation processes in which the intermediate state is a virtual state of the system. Finally, ESA is used to refer to excited state absorption which occurs when the first photon excites the ion to a real level but relaxation to a metastable state occurs before the second photon is absorbed. Figure 1 illustrates the three different types of possible processes. All three types of processes have been observed in trivalent rare earth ions in solids and it is important to identify the specific type of process in order to determine the cross section for TPA.

The cross section for TPA processes can be expressed through second-order perturbation theory as (14)

$$\sigma = 2\pi\rho_f(E) \sum_{\alpha,\beta} \left| \sum_j \frac{\langle f|p_\alpha|j\rangle\langle j|p_\beta|0\rangle}{\hbar[\Delta\omega_j - i\Gamma_j]} \right|^2 \qquad (2\text{-}1)$$

where $\rho_f(E)$ is the density of final states, p is the electron momentum operator, α,β represent the states of polarization, $\Delta\omega_j$ is the detuning of the laser frequency from the peak of the transition from the ground state $|0\rangle$ to the intermediate state $|j\rangle$, and Γ_j is the natural linewidth of the intermediate state. The absolute magnitude of the denominator represents the upper limit of the interaction time for the TPA

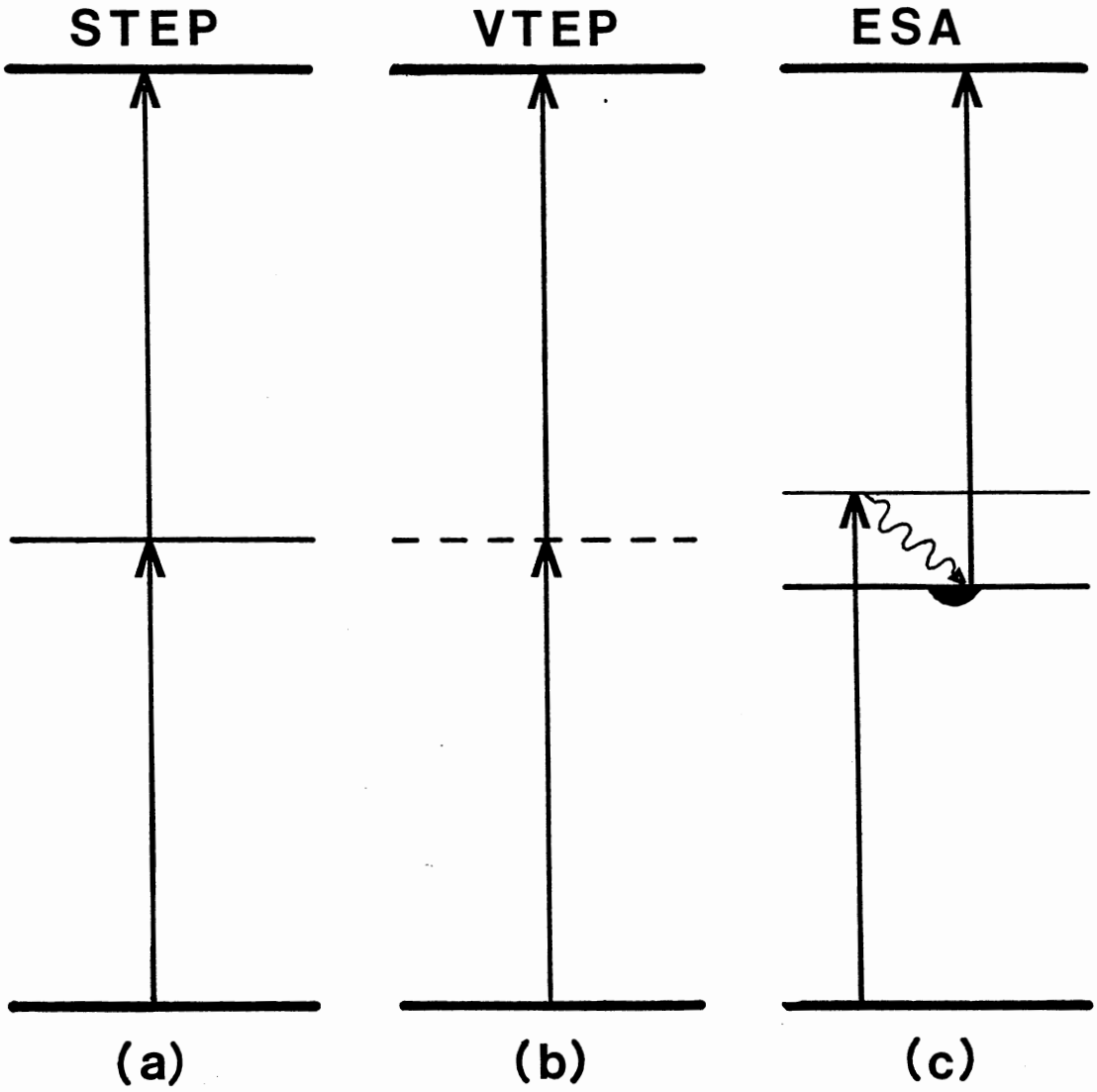

Figure 1. Models Depicting the Three Different Types of Multiphoton Processes, (a) Sequential Two-Photon Excitation Process (STEP), (b) Virtual Two-Photon Excitation Process (VTEP), and (c) Excited State Absorption Process (ESA). The Semicircle Denotes a Metastable State

process. The type of process involved in TPA to a specific final state is determined by the matrix elements and interaction times involved with the different possible intermediate states included in the sum over $|j>$. For trivalent rare earth ions, the initial state has a $4f^n$ electron configuration and the final state can either be another state of the same configuration or a state of the $4f^{n-1}5d$ configuration. For the former case, parity selection rules strongly favor virtual transitions to 5d intermediate states despite close resonances of real transitions to 4f intermediate states. However, if the final state is part of the $4f^{n-1}5d$ configuration, real transitions to resonant 4f intermediate states or virtual transitions to 4f intermediate states with small detuning parameters can be important in the sum over $|j>$. In this case the matrix elements are approximately the same for the different types of intermediate states and the dominant terms in the sum depend on the interaction times. For virtual intermediate states this is determined by the detuning from resonance and is typically of the order (14) of 10^{-14} to 10^{-15} sec. For real resonant intermediate states the maximum interaction time can range between 10^{-5} to 10^{-9} sec. If coherence is important in the overall TPA process, it is the dephasing time of the intermediate state that determines the maximum interaction time instead of the fluorescence lifetime of the level. Finally, if the laser excitation pulse is shorter than the maximum interaction, then the interaction time of the TPA process is given by the temporal pulse width of the laser. Each of these possibilities must be considered in determining the specific type of process involved in a TPA transition.

Samples and Experimental Processes

The fluoride glass sample investigated in this work had dimensions of 1.82 cm x 1.25 cm x 0.18 cm. Its composition (15) in mole percent was 27 ZnF_2, 19 BaF_2, 26 LuF_3, 27 ThF_4, and 1 EuF_3. The common designation for this glass is BZLT:Eu^{3+}. The oxide glass sample used for comparative studies had the dimensions 1.46 cm x 1.25 cm x 0.36 cm. The composition of this sample in mole percent is 30 Li_2O, 52.3 P_2O_5, 10 CaO, 4.7 Al_2O_3, and 3.0 Eu_2O_3. It is designated as LP:Eu^{3+}.

The first step of this experiment, and of any similar experiment, was to determine the room temperature absorption and fluorescence spectra of the Eu^{3+} glass samples. The absorption spectra were recorded using a Perkin-Elmer Model 330 Spectrophotometer, with special attention being given to the regions corresponding to the laser's four excitation wavelengths. Shown in Figure 2 is the absorption spectra for Eu^{3+} ions in the BZLT glass, with the positions of the various laser frequencies used for pumping shown as solid, vertical arrows. For this sample, we are able to construct the energy levels associated with the $4f^6$ and $4f^5 5d$ electron configurations of Eu^{3+}, shown in Figure 3. The lower sharp levels are associated with states of the $4f^6$ electron configuration. The broad, overlapping bands above 27,000 cm^{-1} may either be due to states of the $4f^5 5d$ electron configuration or to charge transfer states. For the fluoride glass host studied here, the former seems more likely. The charge transfer bands should be very close to the band edge while the 5d bands have been previously identified in Eu^{3+}-doped crystals with their peaks near 200 and 240 nm (16). The latter is in agreement with the bands observed in this fluoride glass and thus

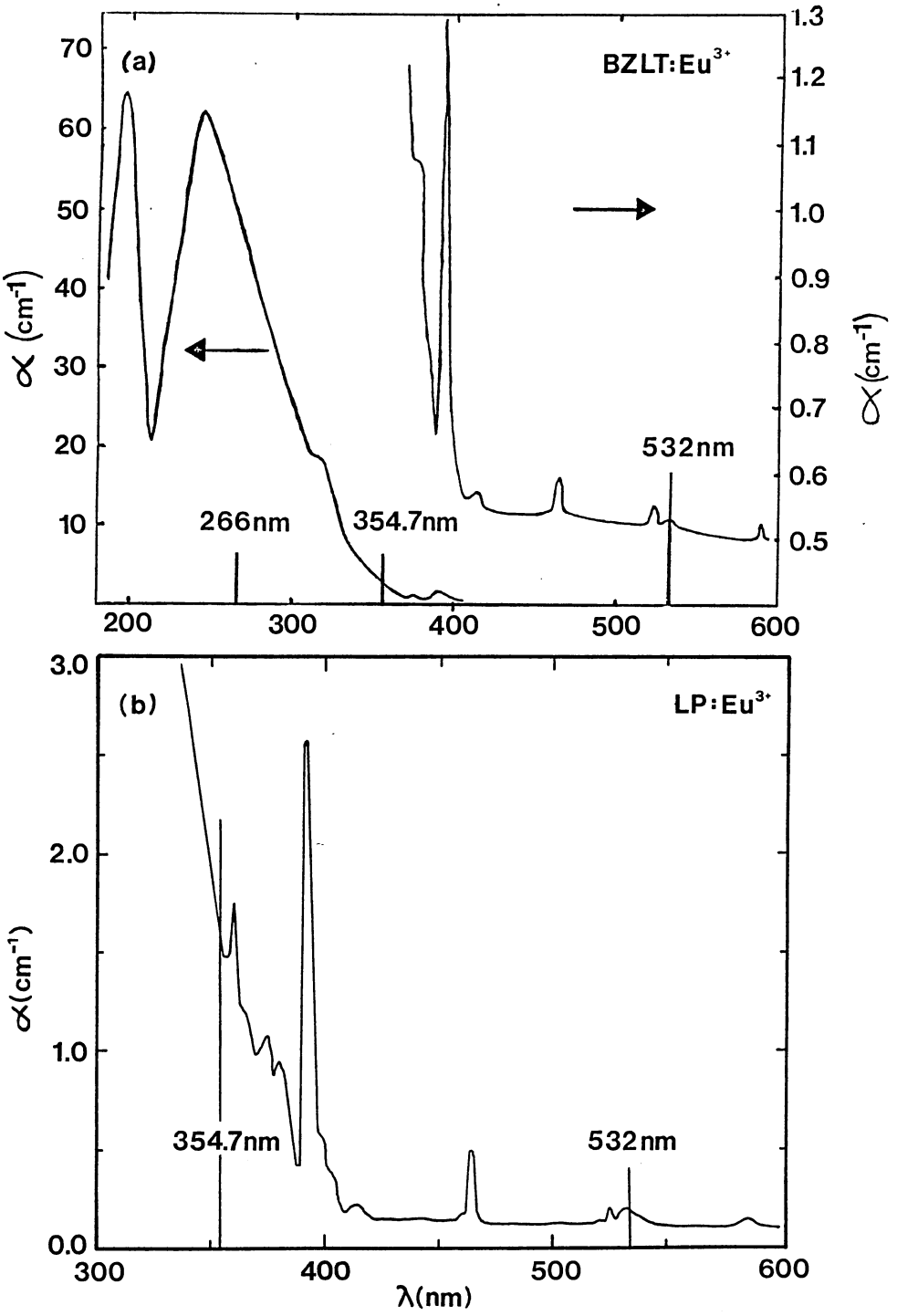

Figure 2. Room Temperature Absorption Spectrum of (a) BZLT:Eu^{3+} and (b) LP:Eu^{3+} with the Positions of the Various Laser Excitation Wavelengths Shown

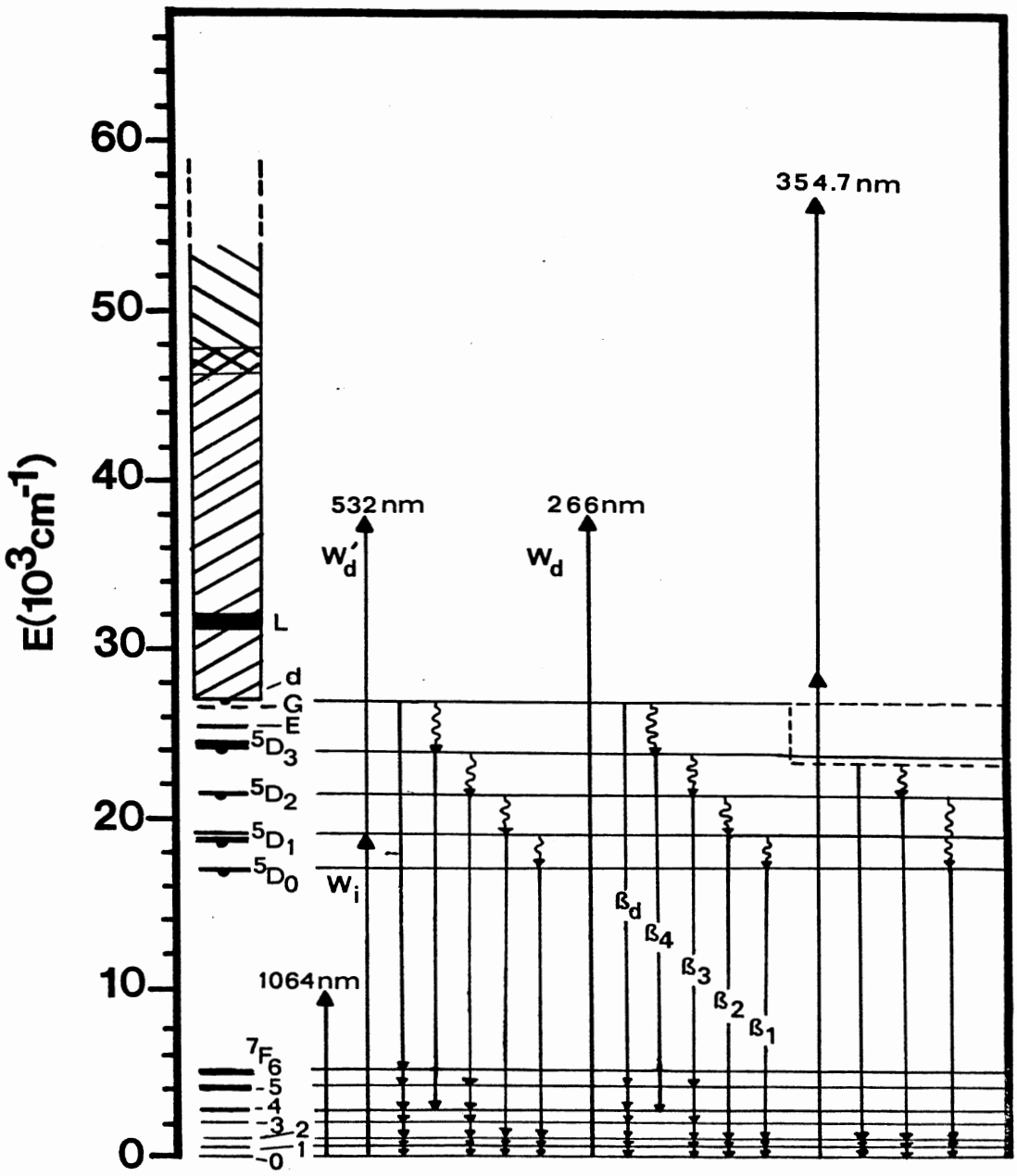

Figure 3. Energy Levels of the $4f^6$ and $4f^5 5d$ Configurations of Eu^{3+} in BZLT Glass with Transitions for Different Excitation Wavelengths Shown

we refer to these bands as 5d bands, although the charge transfer assignment cannot be ruled out at this time. The absorption spectra for Eu^{3+} in the oxide glass in the visible region of the spectrum is similar to the fluoride glass. However, in this case the host band edge is at lower energy and thus the charge transfer bands are shifted below the 5d bands (17) and appear as bands above 24,500 cm^{-1}. The four Nd-YAG-laser harmonic lines used for pumping are also shown in Figure 3. Also labeled are the important multiplets, the approximate crystal-field splittings indicated by the linewidths, and the observed metastable states in the BZLT glass indicated as semicircles. The important absorption and emission transitions for the different excitation wavelengths used in this work are also shown. The solid arrows with straight shafts represent radiative transitions, and those with wavy shafts represent radiationless transitions.

The fluorescence spectra were obtained using Quantel's Series YG400, passively mode-locked, Nd-YAG laser as the excitation source. The laser oscillator provides a train of pulses, and from this train the pulse-switching network will slice a single pulse from the train. After passing through the pulse slicer, the pulse is sent through an amplifier, resulting in a pulse of about 25 picoseconds in duration and with 25 mJ of energy. The primary laser excitation produced is 1064 nm. With the addition of frequency-doubling, -tripling, and -quadrupling crystals and harmonic generators, it is possible to obtain wavelengths of 532.0 nm, 354.7 nm, and 266.0 nm respectively. The characteristics of the emitted beam include an approximate 0.6 milliradian divergence and a stability of $\pm$ 20% on the mode-locked shots. However, the two most important characteristics of the pulsed output are, first, the lasing action takes

place in the TEM_{00} mode with a Gaussian pulse shape, and secondly, it is possible to reach pulse-peak powers on the order of one terawatt. For the two-photon absorption to occur, the use of the high-energy picosecond, Gaussian-shaped pulse is of extreme importance.

Another appealing aspect of the YAG laser was the ability to vary the temporal pulse width by using a variable output mirror at the exit of the cavity. On the particular model used, there existed the capabilities of selecting pulse widths of 25, 50, 100 or 200 picoseconds in duration. The use of varied pulse widths was instrumental in providing information concerning the interaction times if a sequential two-photon excitation processes (STEP) were taking place. By examining the two-photon absorption cross sections with different pulse widths, it was possible to verify that the interaction time is fast compared to that of the pulse width.

Another important feature of the YAG laser was its selectivity of power for each pulse. A moderate range of power selectivity was available at the power supply unit by the adjustment of the amount of high voltage supplied to the flashlamp heads. When an even broader range of laser power was needed, it was possible to vary the power by using a series of polarizers and glass plates. It was also possible to monitor the exact laser power by picking off part of the laser beam with a beam splitter and a Quantel photodiode detector, and then monitoring the detected power versus the intensity of the pulse. This was accomplished by feeding the signal from the photodiode detector into an EG&G Princeton Applied Research Corp. Model 4202 Signal Averager and averaging over a large number of pulses, and then printing out the average pulse intensity

on a Houston Instruments Omniscribe Series D5000 strip chart recorder. Next, a Scientech, Inc. Model 36-2002 Power and Energy Indicator was used to monitor the average energy of the pulses, and this signal was likewise sent to the strip chart recorder. By varying the laser power, we were able to calibrate the laser pulse intensity as a function of power per pulse. So finally, it was possible to measure fluorescence intensities and monitor the calibrated, shot-to-shot intensities in terms of power per pulse. This technique proved to be very useful in verification of two-photon absorption.

The major scope of the experimental procedure was the use of previously developed time-resolved spectroscopy techniques (3-5) to monitor and record the fluorescence spectra of the glass at different times after the pulse. The method of excitation and detection was a fairly straightforward, and highly effective set up. The pulsed output from the YAG laser was focused onto a polished face of the sample with a 35cm focal length lens. The fluorescence from the sample was then detected from the front face of the sample, at an angle of 90^{o} to the incoming pulse. This fluorescence was then focused onto the variable slits of a monochromator using an appropriate combination of one collimating lens, used to collect the fluorescence, and two converging lens. It was also found that mounting a mirror against the back face of the sample helped to collect the fluorescence that was being given off in the opposite direction of the monochromator. The sample fluorescence was measured using two different techniques and experimental apparatuses. The first technique involved using a 1/3-m Instruments S.A., Inc. Monochromator and an RCA C31034 photomultiplier tube to analyze the fluorescence. The signal from the phototube was processed by an EG&G

Princeton Applied Research Crop. Model 162 Boxcar Averager with two Model 164 gated integrator modules. The Boxcar was triggered by picking off part of the laser pulse with the photodiode and was used to obtain the time-resolved spectra. The signal-to-noise ratio was improved by using the signal averager before displaying the results on the chart recorder. As stated before, a photodiode detector was used to monitor the shot-to-shot intensity variation of the laser. A block diagram of this experimental setup is shown in Figure 4. The second technique involved the use of an EG&G Princeton Applied Research, Corp. Optical Multichannel Analyzer II (OMA II) System. The OMA II system includes the Model 1215 computer-operated control console, the Model 1218 detector controller, the Model 1211 high voltage pulse generator, and the Model 1420 intensified silicon diode array detector. The Model 1211 was used to gate the diode array detector to monitor the time after pulse spectra. The delay time range for the 1211 is from 30 ns to 1 sec after the pulse, and this unit is also triggered by either the laser or a fast-response photodiode detector. The Model 1215 comes with computer disk drives, a keyboard, and software that has the capabilities of subtracting off background noise and integrating the fluorescence intensity areas. The fluorescence spectra were analyzed by a 1/3-m Instruments S. A., Inc. Model Hr320 Czerny-Turner type monochromator and the nitrogen-purged water-cooled, diode array. In this case, the spectra were dumped from the computer files and plotted on a Houston-Instruments Omnigraphic Series 2000 X-Y Recorder. These recorded spectra and integrated intensities duplicated almost exactly those recorded using the Boxcar system, thus providing a verification of earlier recorded data, and secondly, a fast and equally precise system of detection.

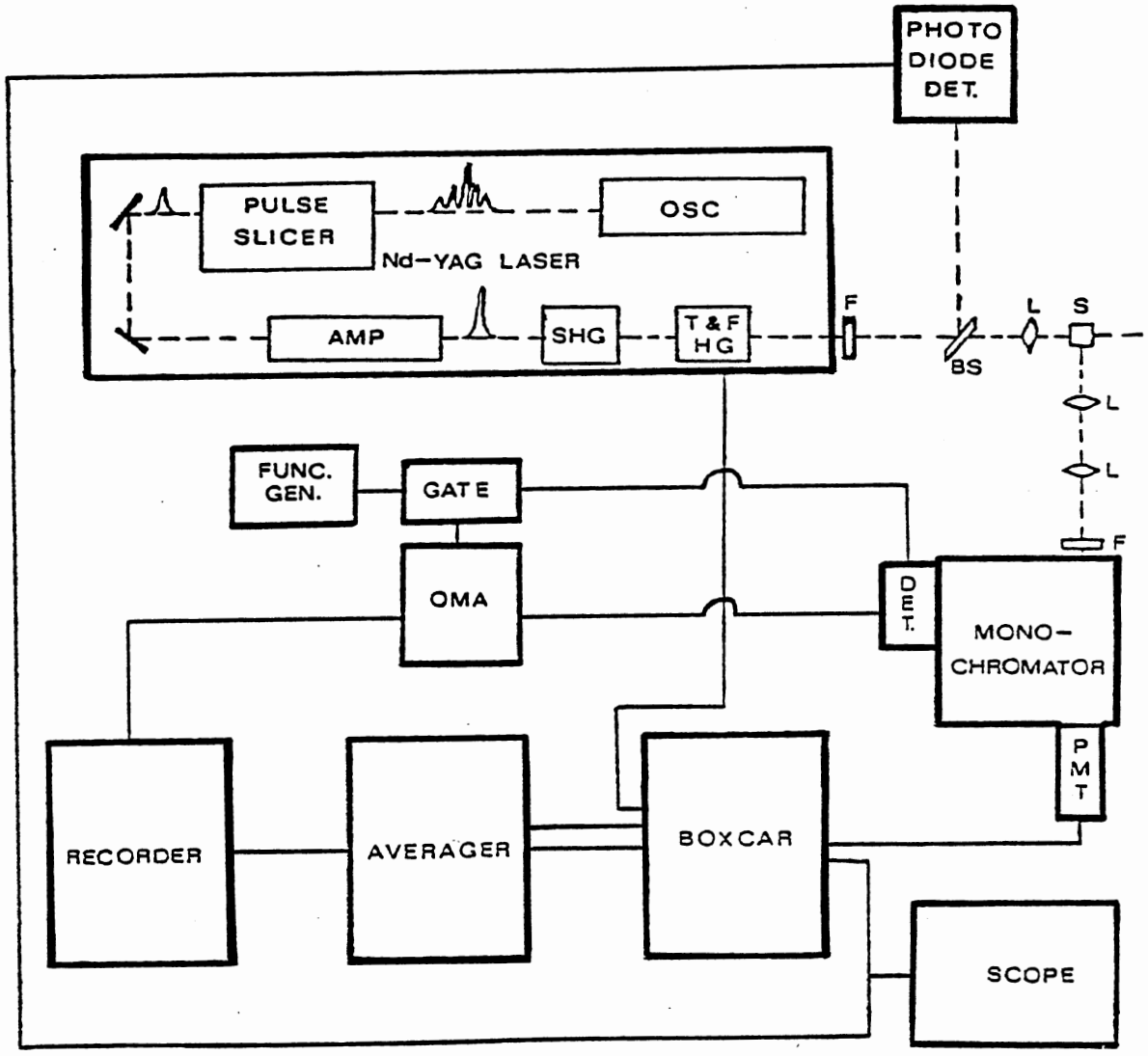

Figure 4. Experimental Apparatus for High-Power, Picosecond Pulse Excitation Experiments

The ISA monochromator used has two separate exit slits, mounted at 90^{o} to one another, that can be used by inserting or removing an exit mirror. Thus, it is possible to use the same monochromator with both the diode array detector and photomultiplier tube attached. This becomes important when it is necessary to monitor the fluorescent lifetimes and risetimes of the different emissions. To monitor these, a Thorn EMI Gencom Inc. Model 3000R power supply was used to supply high voltage to the C31034 phototube. The lifetimes were also measured using two methods. For one, the signal from the phototube was fed into the Boxcar to be analyzed, and the lifetimes were then plotted on the chart recorder. The second method involved feeding the signal from the phototube into the one meg-ohm input of an oscilloscope, in parallel with a variable resistor. The scope used was a Tektronix Model 7834 Storage Oscilloscope with a Model 7A16A amplifier and a Model 7B92A dual time base unit that has a 0.5 ns time per division minimum scale. With this small of a time base scale, it was possible to observe the extremely fast lifetimes and risetimes. After making sure that there was no distortion due to the input load resistor, the storage function could be used to store the lifetime or risetime on the screen. After that, it was possible to accurately calculate the appropriate lifetime or risetime. Once again, the results of the two different methods of detection and recording of the signal gave almost the exact same measurements. One concluding note should be made; all measurements, including absorption, fluorescence, and fluorescence lifetimes, were made at room temperature.

Judd-Ofelt Analysis

The formulation of crystal field induced electric dipole transitions in the $4f^n$ configurations, as developed by Judd (1) and Ofelt (2), was applied to the room temperature absorption spectrum of the BZLT sample to determine parameters useful in the modeling of multiphoton spectroscopy. These parameters include the branching ratios, oscillator strengths, and radiative decay rates. A more complete derivation of the Judd-Ofelt theory is given in the appendix. The oscillator strength of a given transition of average energy, $\sigma(cm^{-1})$, from a level J to a level J´ is expressed as

$$f(aJ;bJ') = \left[\frac{8\pi^2 mc\sigma}{3h}\right] \frac{1}{(2J+1)} \left[\chi S_{ed}(aJ;bJ') + \chi' S_{md}(aJ;bJ')\right] \tag{2-2}$$

where the electric dipole and magnetic dipole line strengths are

$$S_{ed}(aJ;bJ') = \sum_{\lambda=2,4,6} \Omega_\lambda \left|\langle f^n J|| \overleftrightarrow{U}^{(\lambda)} ||f^n J'\rangle\right|^2 \tag{2-3}$$

and

$$S_{md}(aJ;bJ') = \left(\frac{h}{2mc}\right)^2 \left|\langle f^n J|| \vec{L}+2\vec{S} ||f^n J'\rangle\right|^2 , \tag{2-4}$$

respectively. Here a and b represent other quantum numbers designating the states, f^n represents the electronic configuration, $\overleftrightarrow{U}^{(t)}$ is the tensor operator for electric dipole transitions, $\vec{L}+2\vec{S}$ is the operator for magnetic dipole transitions, and the Ω_λ are the Judd-Ofelt parameters that are associated with the crystal field environment of the ion in the host lattice (they are determined by the analysis of the absorption spectrum). χ and χ' are the correction terms for the effective field in the crystal for electric dipole and magnetic dipole

transitions, defined respectively as

$$\chi = \frac{n(n^2+2)^2}{9}$$

and

$$\chi' = n^3$$

with n being the index of refraction of the host at the associated transition frequency. The values for the index of refraction of the BZLT glass have been determined previously (15), and in the visible region of interest these values range from 1.535 at 577 nm to 1.570 at 380 nm. As can be seen from Equations (2-3) and (2-4), to calculate the line strengths it is necessary to know the appropriate values of the square of the matrix element involving the electric dipole tensor operators, $\overleftrightarrow{U}^{(t)}$. The values of the tensor operators and line strengths used in this work are listed in Table I. These reduced matrix elements have been calculated previously (18-20) and are essentially invarient from host to host.

It is extremely difficult to make use of the Judd-Ofelt treatment for Eu^{3+} ions because of the exceedingly weak absorption and the number of bands associated with parity forbidden and electric dipole forbidden transitions. Because of the limited number of weak absorption peaks in the fluoride glass sample, the Judd-Ofelt parameters for a very similar Eu^{3+} doped fluoride glass were used in this evaluation (18). These were found to be $\Omega_2=0.93\text{x}10^{-20}$ cm^2, $\Omega_4=2.61\text{x}10^{-20}$ cm^2, and $\Omega_6=2.17\text{x}10^{-20}$ cm^2. Using these results, the spontaneous emission probability can be obtained for each transition from

$$A(aJ;bJ') = \left[\frac{(8\pi^2 e)^2}{3h}\right]\sigma^3\left[\chi S_{ed}(aJ;bJ') + \chi' S_{md}(aJ;bJ')\right](2J+1)^{-1} \qquad (2\text{-}5)$$

TABLE I

SQUARED MATRIX ELEMENTS OF THE JUDD-OFELT TENSOR AND LINE STRENGTHS, S, FOR Eu^{3+} IN BZLT GLASS

Transition	$\|U_2\|^2$	$\|U_4\|^2$	$\|U_6\|^2$	$S(10^{-23}cm^2)$
$^5D_3 \rightarrow {}^5D_2$	0.0351	0.0126	0.0	65.529
$^5D_1$	0.0183	0.0059	0.0	32.418
$^5D_0$	0.0	0.0	0.0	0.0
$^7F_6$	0.0	0.0	0.0	0.0
$^7F_5$	0.0001	0.0013	0.0	3.486
$^7F_4$	0.0035	0.0002	0.0001	3.994
$^7F_3$	0.0010	0.0005	0.0001	2.452
$^7F_2$	0.0002	0.0018	0.0	4.884
$^7F_1$	0.0004	0.0011	0.0	3.243
$^7F_0$	0.0	0.0	0.0	0.0
$^5D_2 \rightarrow {}^5D_1$	0.0122	0.0	0.0	11.346
$^5D_0$	0.0142	0.0	0.0	13.206
$^7F_6$	0.0	0.0	0.0001	0.217
$^7F_5$	0.0	0.0014	0.0	3.654
$^7F_4$	0.0018	0.0004	0.0	2.718
$^7F_3$	0.0021	0.0024	0.0	8.217
$^7F_2$	0.0016	0.0013	0.0	4.881
$^7F_1$	0.0001	0.0	0.0	0.093
$^7F_0$	0.0007	0.0	0.0	0.651

TABLE I (Continued)

Transition	$\|U_2\|^2$	$\|U_4\|^2$	$\|U_6\|^2$	$S(10^{-23}cm^2)$
$^5D_1 \longrightarrow {}^5D_0$	0.0415	0.0	0.0	38.571
$^7F_6$	0.0	0.0	0.0030	0.279
$^7F_5$	0.0	0.0006	0.0	1.566
$^7F_4$	0.0	0.0024	0.0	6.264
$^7F_3$	0.0033	0.0016	0.0	7.245
$^7F_2$	0.0007	0.0	0.0	0.651
$^7F_1$	0.0023	0.0	0.0	2.139
$^7F_0$	0.0	0.0	0.0	0.0
$^5D_0 \longrightarrow {}^7F_6$	0.0	0.0	0.0002	0.434
$^7F_5$	0.0	0.0	0.0	0.0
$^7F_4$	0.0	0.0023	0.0	6.003
$^7F_3$	0.0	0.0	0.0	0.0
$^7F_2$	0.0032	0.0	0.0	2.976
$^7F_1$	0.0	0.0020*	0.0	5.199
$^7F_0$	0.0	0.0	0.0	0.0

*$^5D_0 \longrightarrow {}^7F_1$ is a magnetic dipole transition and this value is actually the value of $\vec{L} + 2\vec{S}$ for this transition.

The branching ratios for transitions from each emitting level can then be related to the spontaneous emission coefficient through

$$\beta_{i,j} = \frac{A_{i,j}}{\sum_j A_{i,j}} \tag{2-6}$$

where the summation is over electric and magnetic dipole transitions to the final states j. The radiative lifetime for each emitting level can then be determined from

$$(\tau_i^{rad})^{-1} = \sum_j A_{i,j} \, . \tag{2-7}$$

Table II lists the branching ratios, spontaneous emission coefficients, and the radiative lifetimes of the excited states of Eu^{3+} ions in the fluoride glass.

Results for 266.0 nm Pumping

Figure 5 shows the BZLT:Eu^{3+} fluorescence spectra obtained at two different times after the 25 ps excitation pulse for quadrupled Nd:YAG laser pumping at 266.0 nm. The spectral resolution of the laser lines used for excitation is approximately $\pm$ 1 cm^{-1}. Observation of the emission intensity for all lines shows a linear dependence with pump power, thus indicating that single-photon absorption is responsible for exciting all of these transitions. The fluorescence emission includes transitions originating from all the various ^5D_J levels, as well as from the 5d configuration level. Each of the five groups of lines in Figure 5, corresponding to the five different fluorescing states, has its own characteristic lifetime.

TABLE II

SPECTROSCOPIC PARAMETERS OF Eu^{3+} IN BZLT FLUORIDE GLASS (λ- ENERGY OF THE TRANSITION; f-OSCILLATOR STRENGTH: $A_{i,j}$-SPONTANEOUS EMISSION COEFFICIENT; β-BRANCHING RATIO; τ^{rad}-RADIATIVE LIFETIME)

Transition	$\lambda(10^4\ cm^{-1})$	$f(10^{-8})$	$A_{i,j}(s^{-1})$	β	$\tau^{rad}(10^{-3}s)$
$^5D_3 \rightarrow {}^5D_2$	3.4862	9.8906	0.532	0.0070	
$^5D_1$	1.8275	9.3340	1.827	0.0244	
$^5D_0$	1.3839	0.0	0.0	0.0	
$^7F_6$	0.5086	0.0	0.0	0.0	
$^7F_5$	0.4827	3.8003	10.662	0.1427	
$^7F_4$	0.4599	4.5697	14.122	0.1890	
$^7F_3$	0.4405	2.9289	9.866	0.1320	
$^7F_2$	0.4248	6.0498	21.914	0.2933	
$^7F_1$	0.4133	4.1287	15.797	0.2114	
$^7F_0$	0.4070	0.0	0.0	0.0	13.383
$^5D_2 \rightarrow {}^5D_1$	3.8408	2.0972	0.095	0.0013	
$^5D_0$	2.2949	4.0854	0.516	0.0070	
$^7F_6$	0.5955	0.2587	0.485	0.0066	
$^7F_5$	0.5602	4.6304	9.820	0.1331	
$^7F_4$	0.5298	3.6422	8.638	0.1171	
$^7F_3$	0.5042	11.5690	30.290	0.4105	
$^7F_2$	0.4837	7.1636	20.378	0.2762	
$^7F_1$	0.4689	0.1408	0.426	0.0058	
$^7F_0$	0.4609	1.0028	3.143	0.0426	13.552

TABLE II (Continued)

Transition	$\lambda(10^4\ cm^{-1})$	$f(10^{-8})$	$A_{i,j}(s^{-1})$	β	$\tau^{rad}(10^{-3}s)$
$^5D_1 \longrightarrow {}^5D_0$	5.7015	7.9553	0.163	0.0024	
$^7F_6$	0.7048	0.4655	0.624	0.0090	
$^7F_5$	0.6559	2.8075	4.344	0.0627	
$^7F_4$	0.6146	11.9860	21.124	0.3050	
$^7F_3$	0.5804	14.6780	29.002	0.4188	
$^7F_2$	0.5534	1.3832	3.006	0.0434	
$^7F_1$	0.5341	4.7093	10.988	0.1587	
$^7F_0$	0.5237	0.0	0.0	0.0	14.440
$^5D_0 \longrightarrow {}^7F_6$	0.8042	1.8959	1.951	0.0138	
$^7F_5$	0.7412	0.0	0.0	0.0	
$^7F_4$	0.6888	30.6190	42.958	0.3038	
$^7F_3$	0.6462	0.0	0.0	0.0	
$^7F_2$	0.6129	17.0590	30.224	0.2137	
$^7F_1$	0.5893	34.6360	66.384	0.4694	
$^7F_0$	0.5767	0.0	0.0	0.0	37.267

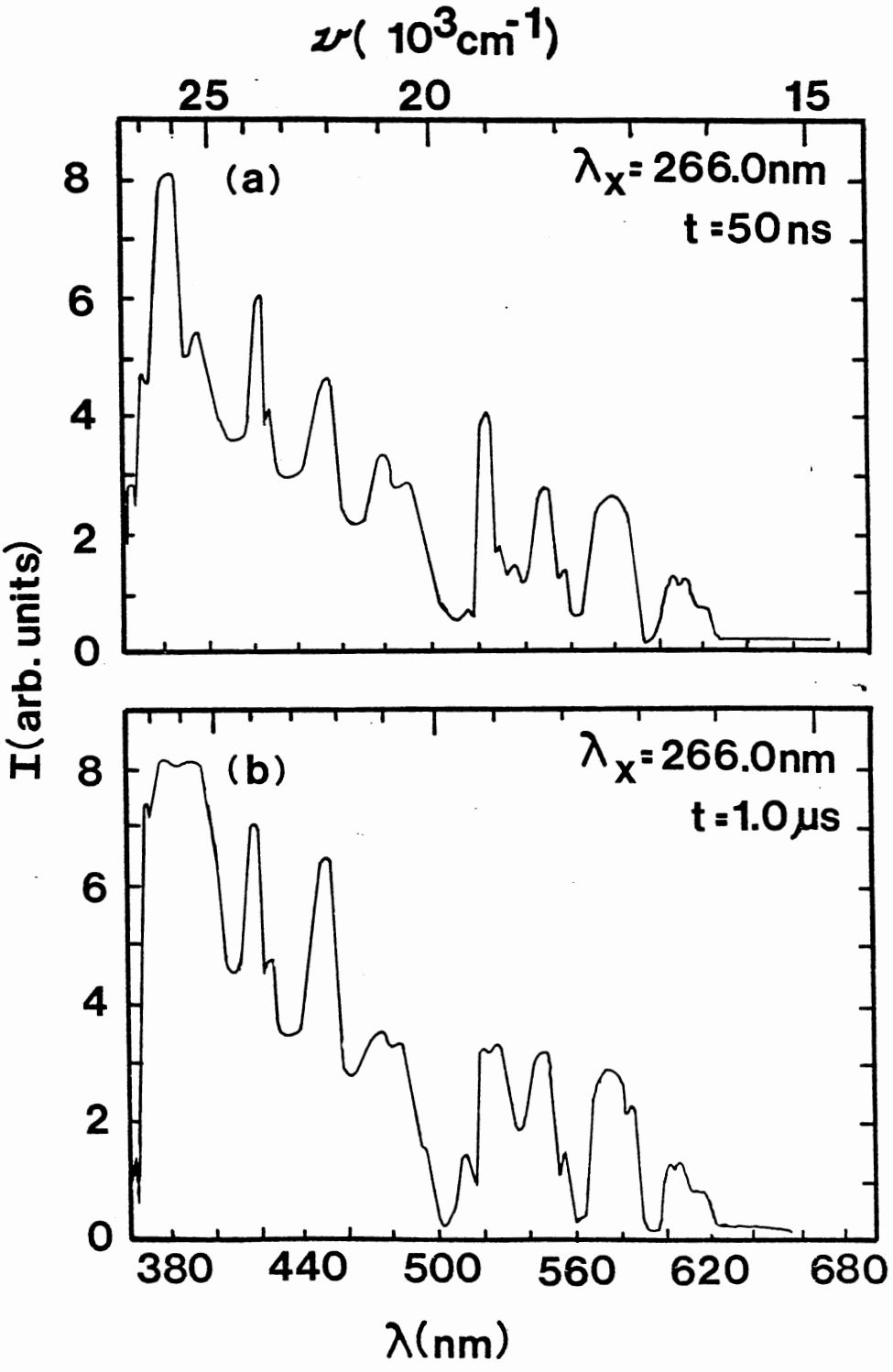

Figure 5. Fluorescence Spectra of BZLT:Eu^{3+} Glass at Two Times after the Excitation Pulse at 266.0 nm, (a) 50 ns and (b) 1.0 μs

Figures 2 and 3 show that the 266.0 nm excitation directly pumps the 5d configuration level. Part of the excitation energy decays radiatively from the 5d level to the various ^7F_J multiplets of the ground state term while the rest of the excitation energy cascades down to the ^5D_J levels by fast radiationless relaxation processes. The fluorescence lifetime of the 5d level is measured to be 70 ns. The $^5D_{3,2,1,0}$ levels all have radiative transitions to the ground state multiplets with fluorescence lifetimes of 1.57 μs, 1.42 μs, 1.24 μs, and 5.94 ms, respectively. All of the lifetimes plotted were single exponential over two decades and have maximum error bars of ±2%. The lifetimes of the ^5D_J metastable states measured here are consistent with the values found previously (19) in a similar heavy metal fluoride glass doped with Eu^{3+}. The fast nonradiative decay rate from $^5D_3$ to $^5D_2$ is determined from the rate equations described below to be 6.1×10^5 s^{-1}. This value is almost identical to the rate of 6.3×10^5 s^{-1} given by the Judd-Ofelt analysis. For 266.0 nm pumping, a rise time of approximately 2 μs occurs when observing the $^5D_0 \rightarrow {}^7F_2$ emission transitions. Using Weber's model (20) for a cascading decay process, the theoretical estimate of this rise time should be <10 μs which is consistent with the observed result. Fluorescence from the $^5D_{2,1,0}$ levels of Eu^{3+} is well known in other hosts, but the observation of fluorescence from the $^5D_3$ and 5d levels is unusual. The fluorescence lifetimes and risetimes for each of the metastable states for these pumping conditions are listed in Table III.

The evolution of the fluorescence spectra shown in Figure 5 can be described by the general rate model shown in Figure 1 or by the more specific model shown in Figure 6. The rate equations describing

TABLE III

CHARACTERISTICS OF METASTABLE STATES OF Eu^{3+} IN BZLT
(Δt=25 ps; T=300 K)

Parameter	Level				
	$^5D_0$	$^5D_1$	$^5D_2$	$^5D_3$	5d
	Fluorescence Lifetimes				
τ_f (μs)					
λ_{ex}=266 or 532 nm	5940	1.24	1.42	1.57	0.07
λ_{ex}=354.7 nm*	0.57 0.26		0.71 0.34		0.82 0.18
	Fluorescence Risetimes				
t_m (μs)					
λ_{ex}=266	1.8	<0.35	0.28	0.06	0.03
532 nm	2100				0.03
λ_{ex}=354.7 nm	-		0.05		0.03

*The fluorescence consisted of the superposition of sharp lines and a broad band.

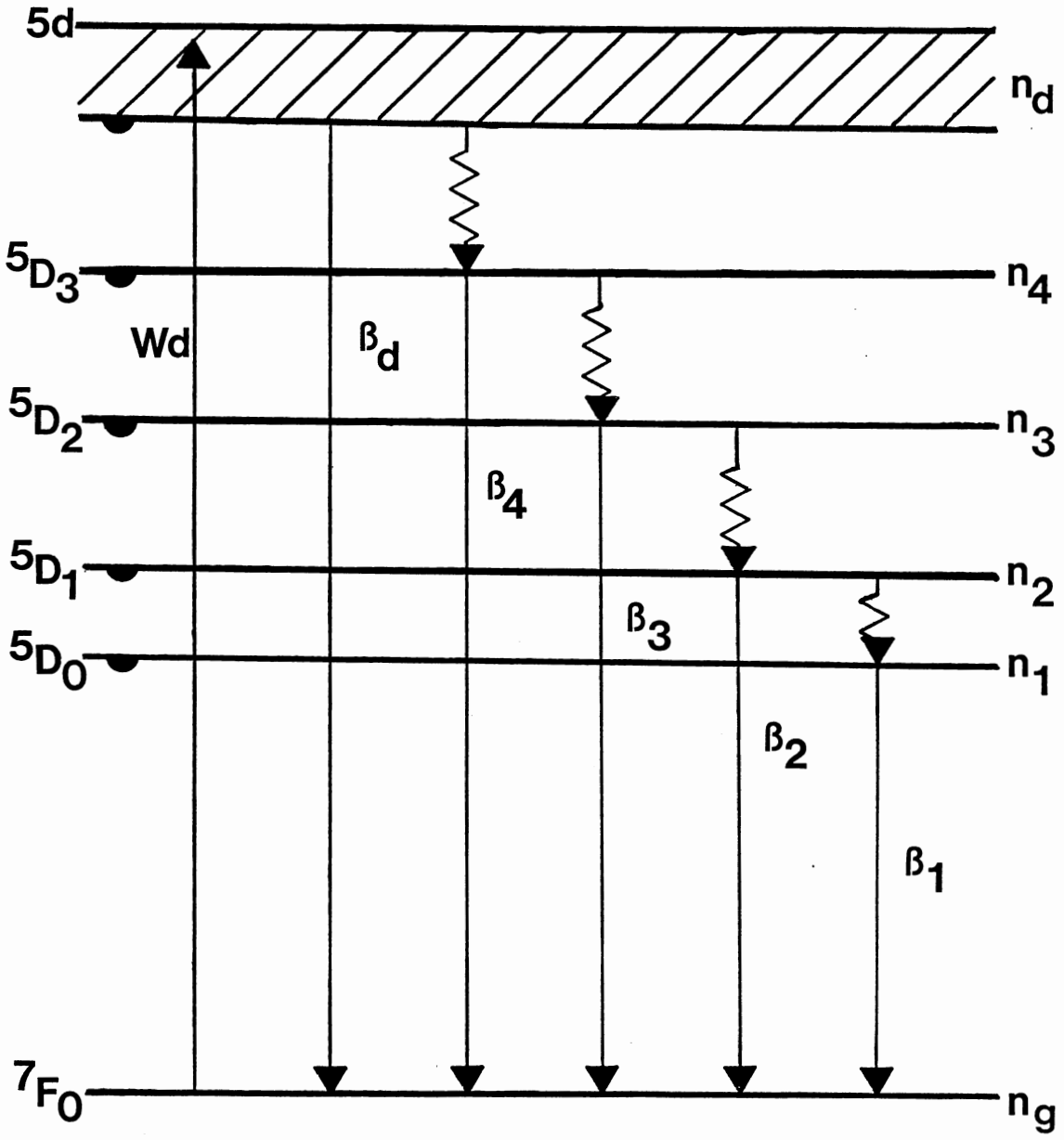

Figure 6. Model for Explaining Observed Spectral Dynamics after 266.0 nm Excitation

the time evolution of the excited state populations are given by

$$\frac{dn_d}{dt} = W_d - \beta_d n_d \tag{2-8}$$

$$\frac{dn_4}{dt} = \beta_d^{nr} n_d - \beta_4 n_4 \tag{2-9}$$

$$\frac{dn_3}{dt} = \beta_4^{nr} n_4 - \beta_3 n_3 \tag{2-10}$$

$$\frac{dn_2}{dt} = \beta_3^{nr} n_3 - \beta_2 n_2 \tag{2-11}$$

$$\frac{dn_1}{dt} = \beta_2^{nr} n_2 - \beta_1 n_1 \quad . \tag{2-12}$$

The n_i's represent the concentrations of ions in the various excited states, the β_i's are the fluorescence decay rates of these levels, the β_i^{nr}'s refer to the nonradiative decay rates, and W_d is the pumping rate of the 5d configuration level. Table II shows from the Judd-Ofelt analysis that nonradiative decay is dominant between the $^5D_3$, $^5D_2$, and $^5D_1$ metastable states whereas radiative decay is the dominant process from the $^5D_0$ state to the ground state components.

Assuming a delta function excitation pulse, these equations can be solved to give the time evolution of the excited state populations. The observed fluorescence intensities from the ith level can be expressed as the product of the population of the level and its radiative decay rate β_i^r. The solution of Equations (2-8) and (2-9) gives the ratio of intensities of the 5d and $^5D_3$ levels as

$$\frac{I_d(t)}{I_4(t)} = K(\beta_4-\beta_d)\left\{1-\exp\left[(\beta_d-\beta_4)t\right]\right\}^{-1} \tag{2-13}$$

where

$$K = \frac{\beta_d r}{\beta_d nr \beta_4 r} \quad .$$

Figure 7 shows the ratios of the integrated fluorescence intensities of all of the 5d transitions to the ground state and the visible transitions from the $^5D_3$ metastable state. By fitting Equation (2-13) to the measured time evolution of the ratios of the fluorescence intensities, after correcting for quantum efficiencies and the spectral sensitivity of the equipment, the value of K can be determined. The best fit shown by a solid line in Figure 7 was obtained with a value of $K=3.4 \times 10^{-6}$ s.

From the value of K obtained from the TRS results it is possible to obtain the radiative decay rate from the 5d configuration level. The values needed for evaluation are the branching ratios for the $^5D_3$ metastable state, and these are available through the Judd-Ofelt analysis of the absorption spectrum. Using the branching ratios, along with the measured value of the fluorescence lifetime of the 5d level, gives an estimate for the radiative decay rate for the 5d level of $9.72 \pm 2.14 \times 10^6$ s^{-1}.

It has been shown previously (3-5), that for certain rare-earth doped solids it is possible to predict the radiative branching ratios from measurements of the total integrated areas of the fluorescence spectra. Such calculations were attempted here, but after a comparison with the Judd-Ofelt predictions and actual fluorescence lifetimes, it was deemed unsatisfactory. The model used for these calculations assumed that any fluorescence from the ^5D_J levels, after 266.0 nm excitation, was due strictly to nonradiative decay from the level immediately above. However, for Eu^{3+} this is not always the case (21),

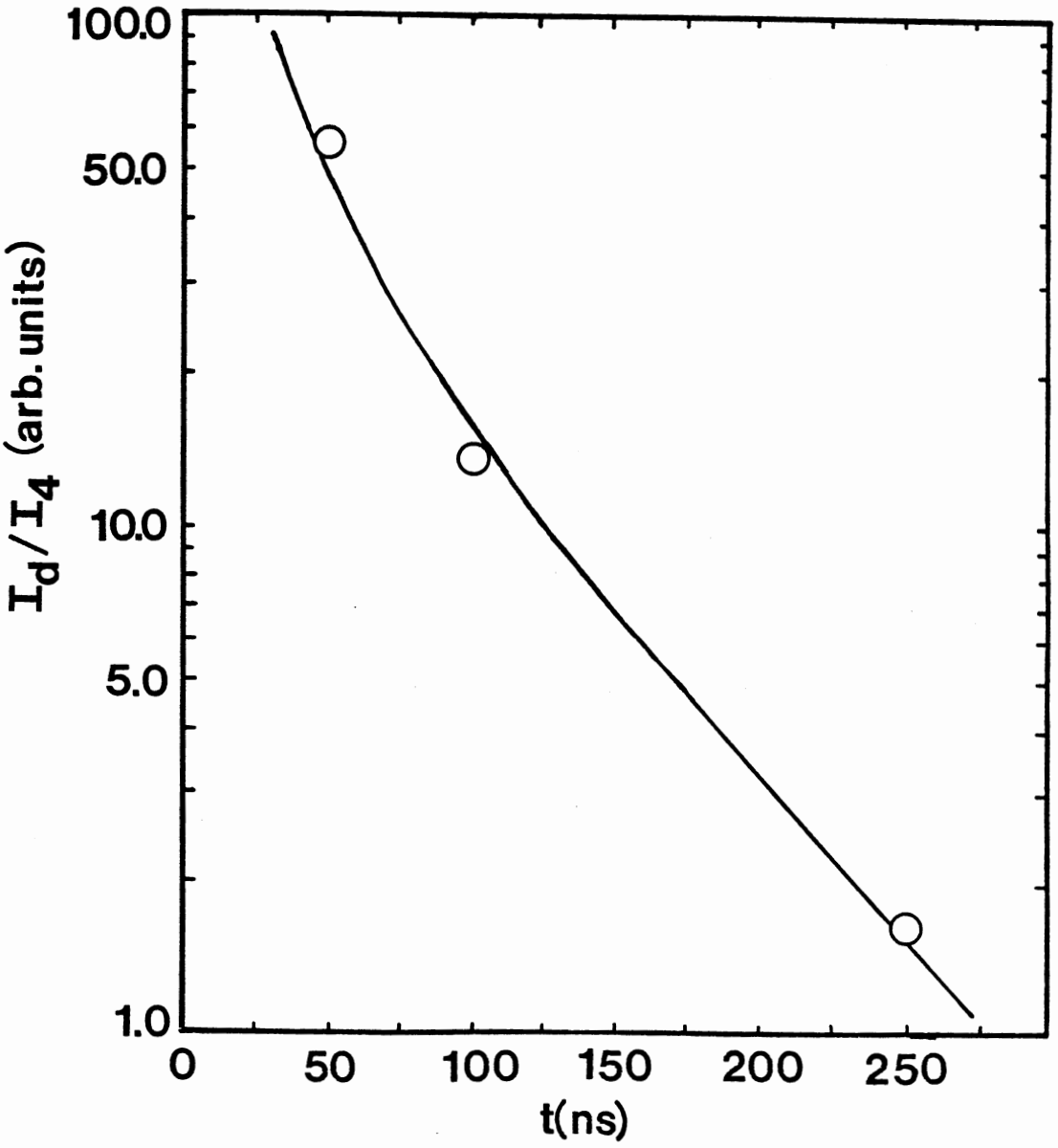

Figure 7. Theoretical Fitting and Experimental Points for the Time Evolution of the Ratios of the Integrated Fluorescence Intensities of the Emission from the 5d Level and the $^5D_3$ Metastable State after 266.0 nm Excitation

as some nonradiateve decay from the $^5D_3$ level has been shown to bypass the $^5D_2$ and $^5D_1$ levels and terminate directly on the $^5D_0$ level. This would cause the step-by-step cascade model to predict inconsistent results for the radiative branching ratios when measuring only fluorescence areas. The analysis of the radiative branching ratios of rare-earth doped solids from the integrated fluorescence spectra and the Judd-Ofelt analysis of the absorption spectra should give the same results if the decay model is a pure cascade process. However, for the case of BZLT:Eu^{3+}, where some nonradiative decay can bypass certain levels, the comparison of results shows differences which can be attributed to a more complex mechanism for decay.

Figure 8a shows the LP:Eu^{3+} fluorescence spectrum at 50 μs after the 266.0 nm excitation pulse. The fluorescence from the $^5D_0$ metastable state to the $^7F_{0,1,2,3,4}$ multiplets of the ground term is much stronger in the oxide glass than in the fluoride glass. The measured fluorescence lifetime of the $^5D_0$ level is 3.15 ms for this sample and is also purely single exponential. There is some very weak fluorescence from the $^5D_2$ and $^5D_1$ metastable states as well as some weak broad band fluorescence at higher energies which may be associated with charge transfer transitions. This is typical for oxides, where previous results (22,23) have shown that the charge transfer states feed instantaneously the $^5D_2$ and $^5D_1$ levels, bypassing the $^5D_3$ and higher levels. The signal from the weak fluorescence transitions was too small to obtain accurate fluorescence lifetime measurements. A comparison of the Eu^{3+} fluorescence in the oxide and fluoride glass hosts for this type of excitation shows that radiationless relaxation processes are more efficient in the

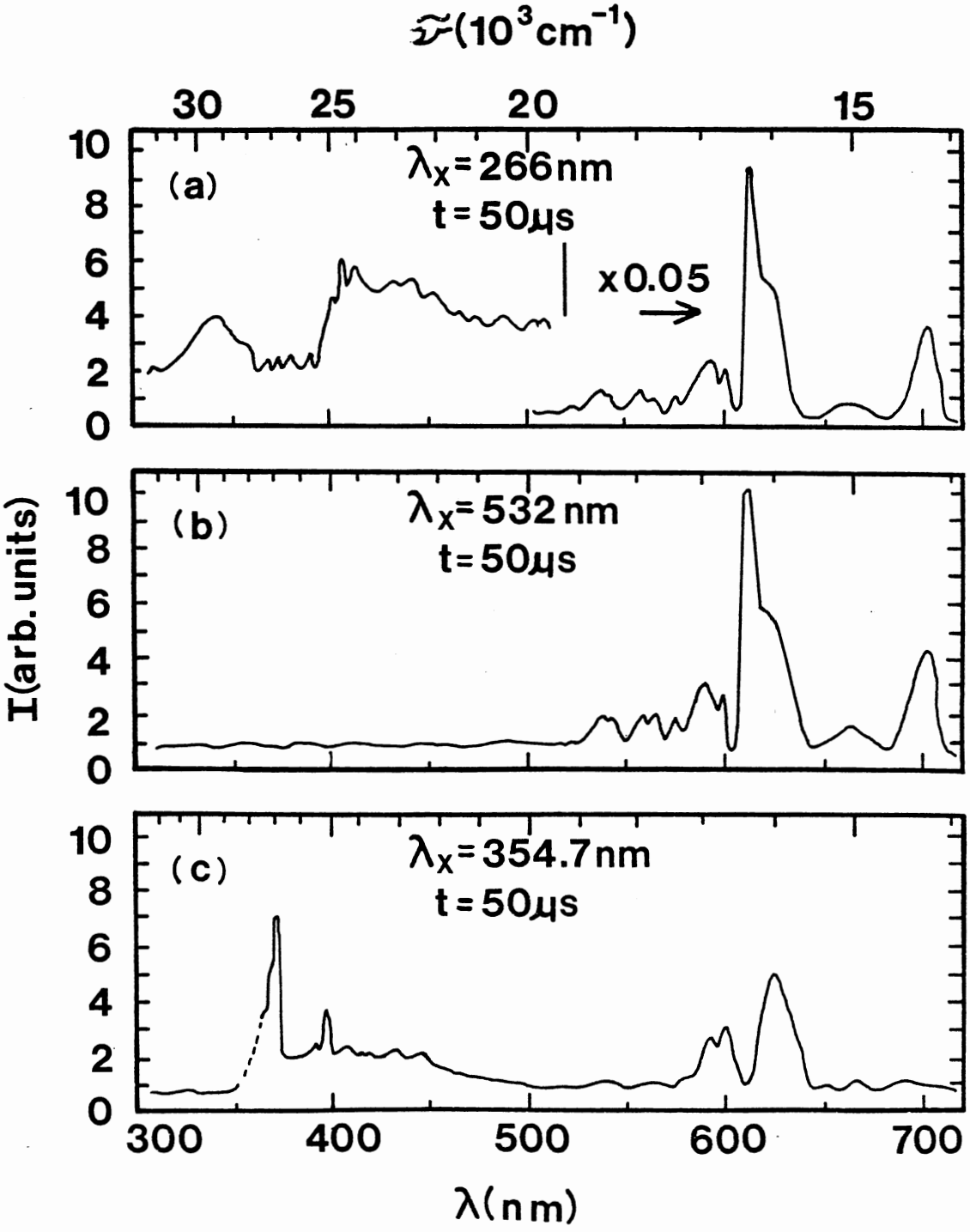

Figure 8. Fluorescence Spectra of LP:Eu^{3+} Glass at 50 μs after the Pulse for Excitation at (a) 266.0 nm; (b) 532.0 nm; and (c) 354.7 nm

oxide glass which is consistent with previous results obtained using other types of excitation (24-26).

Results for 532.0 nm Pumping

Figure 9 shows the fluorescence spectra at two different times after the laser excitation pulse for doubled Nd:YAG laser pumping at 532.0 nm. The same lines appear in the spectra as seen in Figure 5, but their relative intensities are different and change with excitation power. Figure 10 shows the variation in the integrated fluorescence intensity of the emission line near 515.0 nm as a function of excitation energy per pulse, with corresponding measured values listed in Table IV. The observed quadratic dependence indicates that this fluorescence transition is excited under these pumping conditions by two-photon absorption terminating on a level of the 5d configuration. This quadratic dependence is predicted theoretically by using Equation (2-1), which can be rewritten in terms of the electric field, $\vec{E}_o$ and the dipole moment operator, $\vec{\mu}$, to give the probability per unit time as (27,28):

$$W^{(2)}(E) = \frac{2\pi}{\hbar^2}\rho(E)\sum_j \left| \frac{\langle f|\vec{E}_o\cdot\vec{\mu}|j\rangle\langle j|\vec{E}_o\cdot\mu|o\rangle}{\Delta\omega_j - i\Gamma_j} \right|^2 \qquad (2\text{-}14)$$

$$\simeq \frac{2\pi}{\hbar^2}\rho(E)\sum_j \left| |E_o|^2 \frac{\langle f|\vec{\mu}|j\rangle\langle j|\vec{\mu}|o\rangle}{\Delta\omega_j - i\Gamma_j} \right|^2$$

$$\simeq \frac{2\pi}{\hbar^2}\rho(E)|E_o|^4\sum_j \left| \frac{\langle f|\vec{\mu}|j\rangle\langle j|\vec{\mu}|o\rangle}{\Delta\omega_j - i\Gamma_j} \right|^2 .$$

Now, making use of the fact that the intensity of the laser, I, is proportional to the square of the electric field, the probability becomes

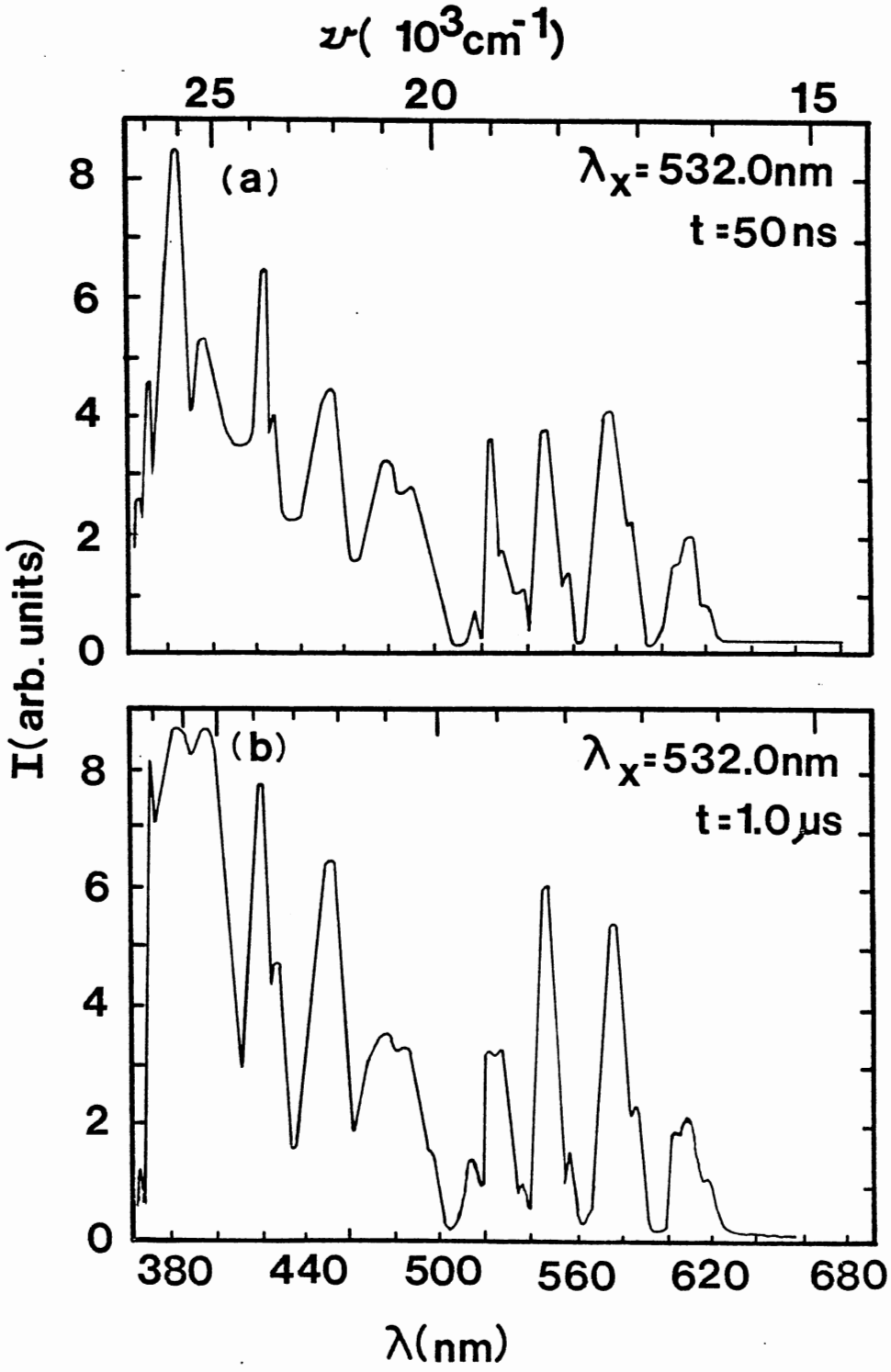

Figure 9. Fluorescence Spectra of BZLT:Eu^{3+} Glass at Two Different Times after the Excitation Pulse at 532.0 nm, (a) 50 ns and (b) 1.0 μs

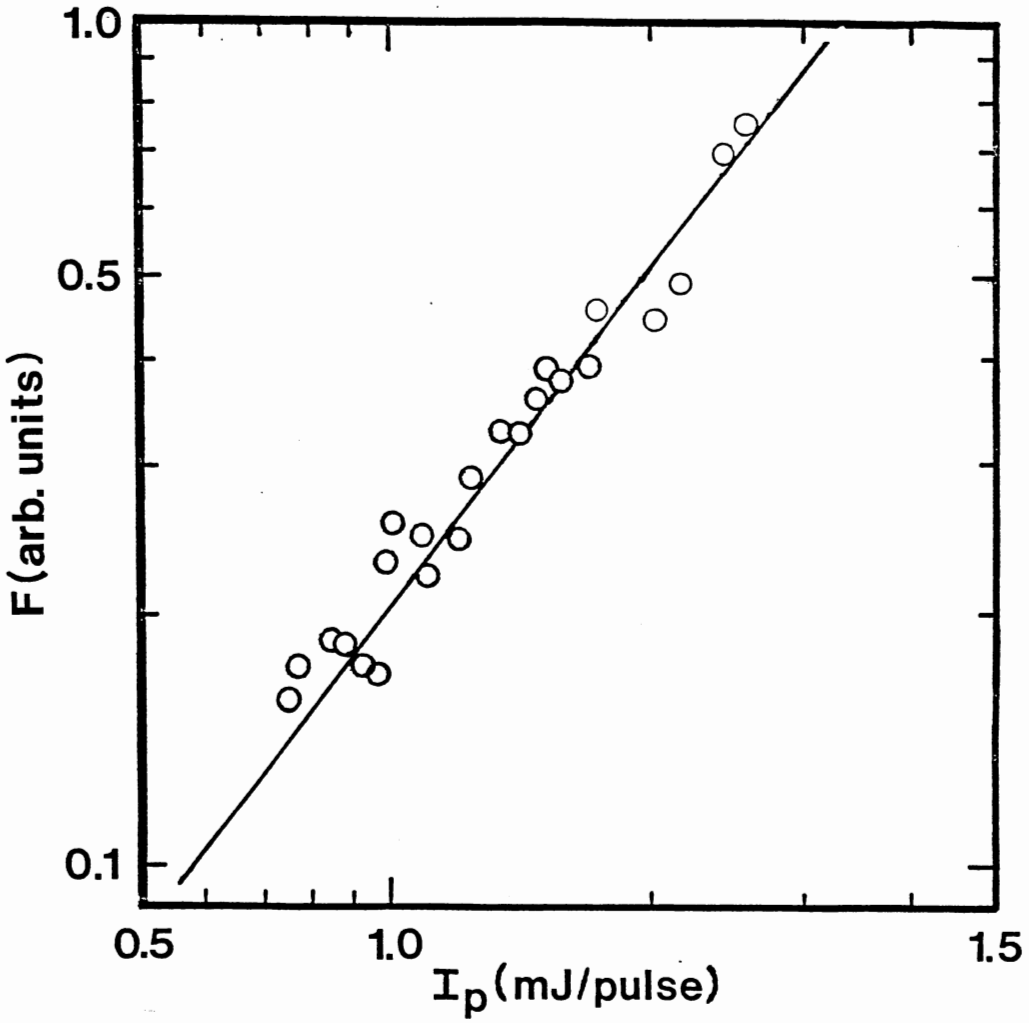

Figure 10. Integrated Fluorescence Intensity of the 515.0 nm Spectral Line as a Function of Laser Energy at 532.0 nm Excitation with a 25 ps pulse

TABLE IV

INTEGRATED FLUORESCENCE INTENSITIES OF THE 515.0 nm SPECTRAL LINE IN BZLT:Eu^{3+} AS A FUNCTION OF LASER POWER AT 532.0 nm EXCITATION

F(arb. units)	I_p(mJ/pulse)
0.160	0.755
0.175	0.772
0.187	0.848
0.185	0.882
0.176	0.940
0.170	0.978
0.233	0.985
0.257	1.000
0.250	1.010
0.224	1.013
0.248	1.022
0.290	1.025
0.335	1.035
0.331	1.042
0.358	1.050
0.392	1.054
0.381	1.059
0.395	1.072
0.464	1.077
0.448	1.105
0.488	1.120
0.702	1.144
0.750	1.158

$$W^{(2)}(E) = C\left(\frac{2\pi}{\hbar^2}\right)\rho(E)\ I^2 \sum_j \left| \frac{\langle f|\vec{\mu}|j\rangle\langle j|\vec{\mu}|o\rangle}{\Delta\omega_j - i\Gamma_j} \right|^2 \qquad (2\text{-}15)$$

where C is a constant taking into account all proportionality factors, and thus the fluorescence of a two-photon transition should be proportional to the square of the laser intensity. The fluorescence transitions from all of the metastable states are the same as those discussed in the preceding section following single photon pumping of the 5d level. As seen in Figure 2, the intermediate state for this two-photon transition is one of the Stark components of the $^5D_1$ level, which can be directly pumped through one-photon absorption processes at this excitation wavelength. Only part of the ions excited to this intermediate state will absorb a second photon while the rest will decay either radiatively to the ground state or radiationlessly to the $^5D_0$ level from which fluorescence emission occurs to the ground state multiplets.

As is shown in Table III, the risetime of the fluorescence decay profiles for the $^5D_0 \rightarrow {}^7F_2$ transition is measured to be 2.1 ms, with a 5.9 ms decay time. The decays occuring after the initial rise were observed to be single exponential. The observed risetime is much longer than expected for a direct nonradiative transition from the $^5D_1$ level. Longer than normal risetimes of fluorescence from the $^5D_0$ level have been observed previously (26,29) and attributed to intersite energy transfer. Similar processes could also be important for the glass host investigated here. The laser excitation in resonance with the absorption transition to the $^5D_1$ level can selectively excite ions in specific host environments (29). This is possible since

the laser linewidth (<0.5 Å) is much less than the widths of the excited electronic levels (approximately 100 Å). The long risetime was found to be independent of the power of the laser excitation indicating that it is not specifically associated with multiphoton processes.

Figure 8b shows the LP:Eu^{3+} fluorescence spectrum at 50 μs after the 532.0 nm excitation pulse. As with 266.0 nm excitation, there is a strong fluorescence from the $^5D_0$ level and only weak emission from the $^5D_1$ level. No fluorescence were observed from any of the higher levels indicating that no multiphoton absorption processes are occurring. The fluorescence lifetime of the $^5D_0$ levels is 3.15 ms, also found to be single exponential, and the risetime is 600 μs. The latter is again anomalously long for a simple radiationless relaxation processes. The LP glass and a similar Eu^{3+}-doped fluoride glass were studied previously (30) under different excitation conditions. The results indicated that the lifetimes remained single exponential and fairly constant across the fluorescence band. The measured energy transfer among the Eu^{3+} ions is weak and thus does not strongly affect the observed decay kinetics, although it can contribute to the initial rise of the fluorescence.

A simplified rate diagram to describe the pumping and decay dynamics under these excitation conditions is shown in Figure 11, and is similar to that for 266 nm pumping, which is shown in Figure 5. The parameters are the same as those previously used except there are the additional parameters W_i to describe the initial single-photon pumping rate of the $^5D_1$ level, and the second photon pumping rate of the 5d level given by W_d'. Thus, Equations (2-8) and (2-11) now become

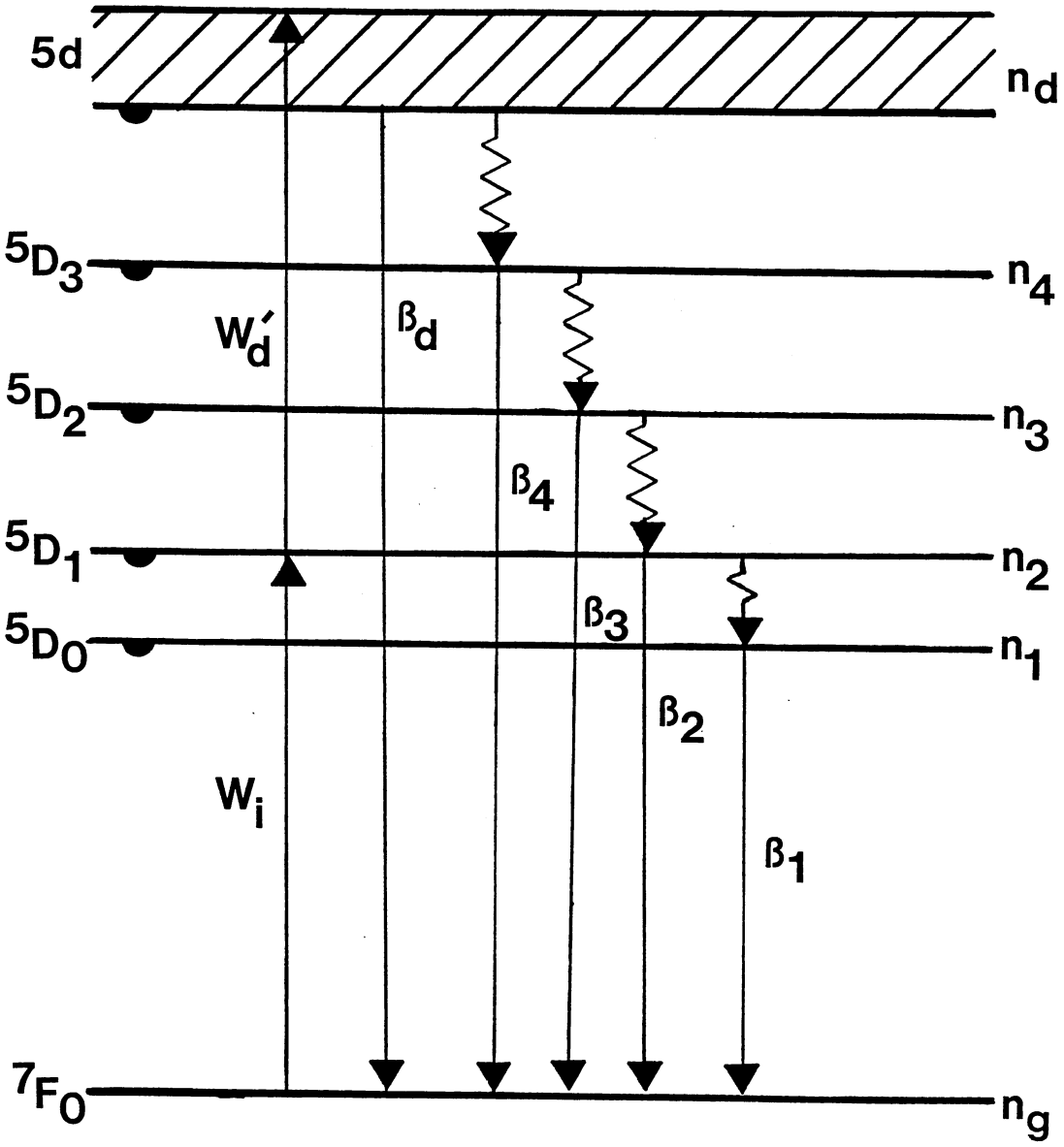

Figure 11. Model for Explaining Observed Spectral Dynamics after 532.0 nm Excitations

$$\frac{dn_d}{dt} = W_d' - \beta_d n_d \tag{2-16}$$

$$\frac{dn_2}{dt} = W_i + \beta_3^{nr} n_3 - \beta_2 n_2 \tag{2-17}$$

with Equations (2-19), (2-10), and (2-11) remaining the same. Once again, the solutions of Equations (2-16) and (2-17) for δ-function excitation can be related to the measured relative fluorescence intensity ratios through

$$\frac{I_2(t)}{I_3(t)} = \frac{A+B}{C} \tag{2-18}$$

where the variables A, B, and C are given by:

$$A = n_2(0)\beta_2^{r}\exp(-\beta_2 t) \tag{2-19}$$

$$B = n_d(0)\beta_2^{r}\beta_3^{nr}\beta_4^{nr}\beta_d^{nr}\left\{\frac{\exp(-\beta_3 t)}{(\beta_2-\beta_3)(\beta_4-\beta_3)(\beta_d-\beta_3)}\right\} + \left\{\frac{\exp(-\beta_4 t)}{(\beta_2-\beta_4)(\beta_3-\beta_4)(\beta_d-\beta_4)}\right\} + \left\{\frac{\exp(-\beta_d t)}{(\beta_2-\beta_d)(\beta_3-\beta_d)(\beta_4-\beta_d)}\right\} \tag{2-20}$$

$$C = n_d(0)\beta_3^{r}\beta_4^{nr}\beta_d^{nr}\left\{\frac{\exp(-\beta_3 t)}{(\beta_d-\beta_2)(\beta_4-\beta_3)}\right\} + \left\{\frac{\exp(-\beta_4 t)}{(\beta_3-\beta_4)(\beta_d-\beta_4)}\right\} + \left\{\frac{\exp(-\beta_d t)}{(\beta_3-\beta_d)(\beta_4-\beta_d)}\right\} \tag{2-21}$$

A simplified expression describing the ratio of the initial populations of the 5d and the $^5D_1$ levels is given by evaluating Equation (2-18) at long times after the excitation pulse. This evaluation is made possible with a few minor assumptions. Since it is experimentally determined that $\beta_2 \tilde{\approx} \beta_3 \tilde{\approx} \beta_4 << \beta_d$, then as $t \to \infty$ the exponentials involving β_d will become negligible and we can assume that $\beta_2 \doteq \beta_3 \doteq \beta_4$. Likewise, since $\beta_2 \tilde{\approx} \beta_3$ and the Judd-Ofelt analysis shows that $(\beta_2^r / \beta_3^r) \approx 1$, our expression simplifies to

$$\left| \frac{I_3(t)}{I_2(t)} \right|_{t \to \infty} = \gamma \beta_d^{nr} \beta_4^{nr} \left[\left(\frac{n_d(0)}{n_2(0)} \right) - \alpha \beta_3^{nr} \right] \qquad (2\text{-}22)$$

where $\gamma = 3.9 \times 10^{-15}$ s^2 and $\alpha = 3.7 \times 10^{-2}$ s. We may then use the values of the intensity ratios at long times after the pulse to find the initial populations of the levels.

Figure 12 shows the ratios of the integrated fluorescence intensities of all of the 5d transitions and the visible transitions from the $^5D_1$ level in the fluoride glass for the four different pulse widths. The data, which are given in Table V, indicate that the relative values of the inital populations of the 5d and $^5D_1$ levels are approximately independent of the excitation pulse width. This indicates either that the maximum possible interaction time for the TPA process is much longer than the laser pulse width so that no change in the intermediate state occurs during the time of the experiment, or that any transient changes in the properties of the intermediate state occur very rapidly with respect to the excitation pulse width.

Using the measured asymptotic values for the intensity ratios and Equation (2-22), the inital population ratios are determined. These

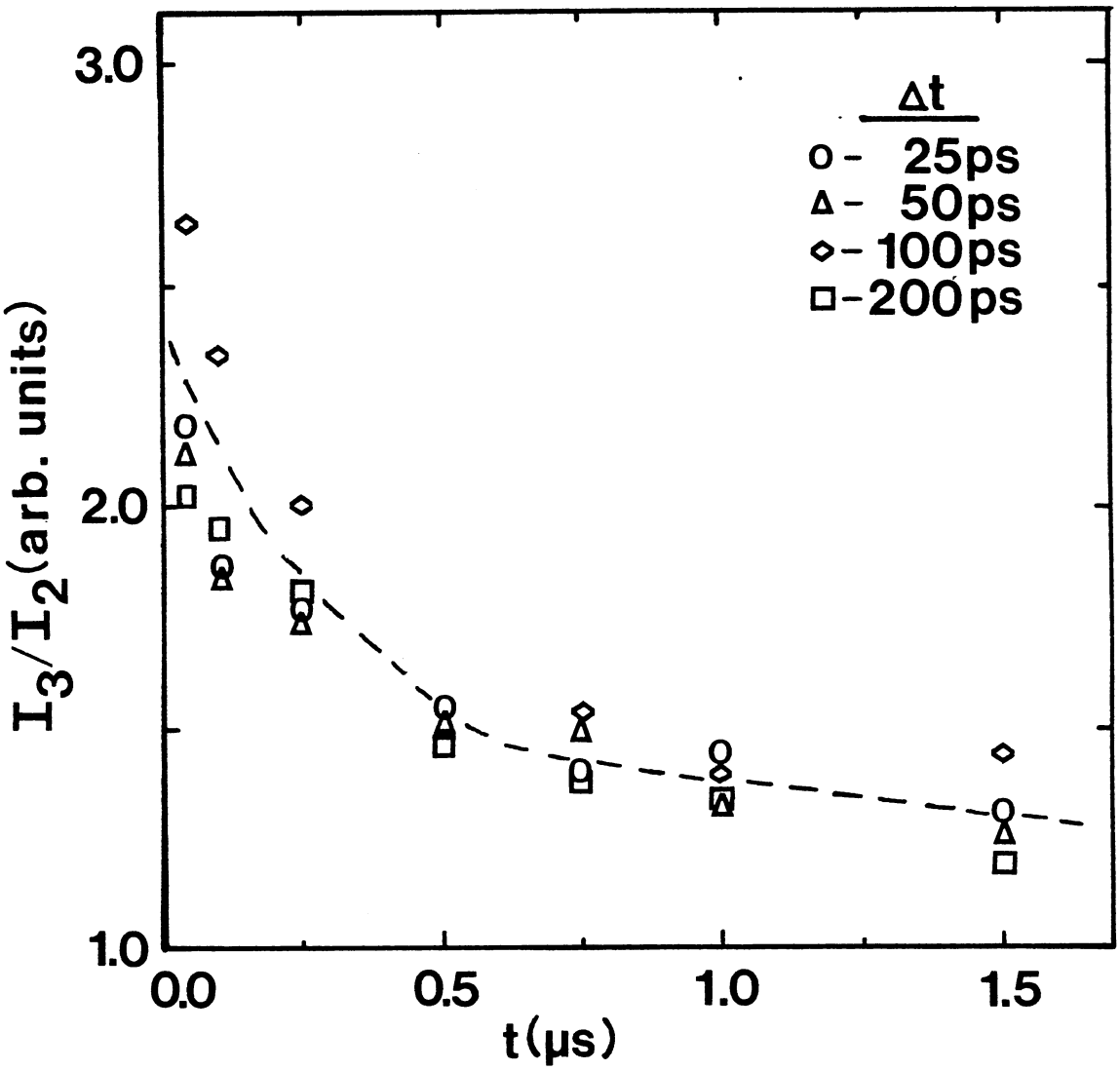

Figure 12. Time Evolution of the Ratios of the Integrated Fluorescence Intensities of the Emission from the $^5D_2$ and $^5D_1$ Metastable States after 532.0 nm Excitation, for Four Different Pulse Widths Δt

TABLE V

TIME EVOLUTION OF THE RATIOS OF THE INTEGRATED INTENSITIES OF BZLT:Eu^{3+} FOR DIFFERENT EXCITATION WAVELENGTHS AND PULSE WIDTHS

			Time After Pulse						
λ_x(nm)	Δt(ps)	I_i/I_j	50 ns	100 ns	250 ns	500 ns	750 ns	1.0 µs	1.5 µs
266 nm	25	I_d/I_4	56.55	13.51	1.59	--	--	--	--
532 nm	25	I_3/I_2	2.18	1.84	1.74	1.56	1.46	1.48	1.30
	50	I_3/I_2	2.13	1.83	1.78	1.50	1.50	1.38	1.27
	100	I_3/I_2	2.64	2.35	2.02	1.58	1.56	1.44	1.40
	200	I_3/I_2	2.00	1.97	1.83	1.47	1.44	1.38	1.23

values of the initial population ratios can then be used to calculate the cross section for the second part of the TPA transition. The expresssion for this is (3)

$$\sigma_{2d}(cm^2) = \frac{n_d(0)}{n_2(0)}\left(\frac{h\nu_2}{h\nu_d}\right)\left\{\frac{\Delta t}{0.375 I_p}\right\}\{\xi\} \qquad (2\text{-}23)$$

where Δt is the laser pulse width, and I_p is the photon flux per pulse. A major simplification used in Equation (2-23) is the expression $P(t)=(0.375/\Delta t)$ for the pulse-time dependence instead of the full Gaussian expression

$$P(t) = \left(\frac{0.375}{\Delta t}\right) \exp\left[-2.77\left(\frac{(t-t_o)}{\Delta t}\right)\right]^2 . \qquad (2\text{-}24)$$

In order to evaluate the cross-section for the second step in the TPA process, it is necessary to estimate a value for the rate of interaction in the intermediate state, ξ. The fluorescence lifetimes of the ^5D_J metastable states are all much greater than the laser pulse widths. Using either these lifetimes or the time of the laser pulse as the effective interaction time gives values for the cross sections which are several orders of magnitude smaller than the values expected for f-f transitions. Thus ESA and STEP transitions with incoherent intermediate states can be eliminated as the type of TPA process. For a transition involving a virtual intermediate or a coherent TPA process with a real resonant intermediate state the coherence times have been found to be in the range 10^{-12} to 10^{-15} s (27). This can be estimated by considering the spectral line shape of the absorption transition from the ground state to the possible intermediate states. According to Equation (2-1), the dephasing time will then be the maximum interaction

time for TPA involving a real intermediate state. For transitions involving virtual intermediate states, the maximum interaction time is less than the coherence time by an amount determined by the detuning from resonance. In our case the single photon absorption terminates on the edge of an absorption band due to a transition terminating on one of the Stark-split components of the $^5D_1$ metastable state. However, there are other levels with small detuning parameters, such as the other Stark components of $^5D_1$, which can have interaction times equal to or greater than that of the resonant interaction and thus cannot be neglected in the sum over intermediate states in Equation (2-1). The measured transition linewidths in the absorption spectrum were used to estimate the coherence times.

This analysis gives a value of $\xi = 4.6 \times 10^{13}$ Hz for the resonant transition, which provides an upper limit for the interaction time, since at room temperature the linewidths should be a combination of homogeneous broadening due to phonon processes and inhomogeneous broadening due to the glass host. For nearby off-resonance transitions, the measured coherence time is somewhat greater but inclusion of the detuning parameter leads to similar interaction times. Thus the value found for ξ is used as an estimate of the interaction time. Using this value of ξ along with the values of the population ratios obtained from Equation (2-23) and the excitation pulse intensity and pulse width, Equation (2-24) gives the values of the cross-sections for the second transitions in the TPA processes. The magnitudes are somewhat larger than those of ground state absorption transitions because they are parity allowed. This indicates that the TPA processes are either VTEP processes or a coherent STEP process in which fast phonon dephasing processes that broaden the

intermediate level without shortening its lifetime are important in determining the cross section of the second step in the TPA processes.

Figure 13 shows the variation of σ_{2d} with excitation pulse width for the BZLT sample, with Table VI listing the values of σ_{2d} and I_p for each pulse width. Experimental error in determining the corrected values of the intensities limits the accuracy of the σ_{2d} values to $\pm$ 2×10^{-19} cm^2. The linear relationship between the cross section and the laser pulse width is consistent with Equation (2-23) and the magnitude is consistent with a fast interaction time compared to the pulse width.

Results for 354.7 nm Pumping

Figure 14 shows the fluorescence spectra at two different times after the excitation pulse for tripled Nd:YAG laser pumping at 354.7 nm. The lifetimes of the transitions are listed in Table III. This emission is quite different from that observed with 532.0 nm or 266.0 nm pumping. The wavelength of the emission transitions are at different positions and the lifetimes are different. Each of the three sets of fluorescence peaks involves a double exponential decay with a very fast risetime. For example, the 410 nm peaks have a longer decay component of 819 ns, a faster component of 179 ns, and a risetime of approximately 30 ns. The other two sets of peaks show similar lifetimes and risetimes which are listed in Table III.

The double exponential decays, the risetimes, the shift in transition wavelengths, and the reduction in the number of emission peaks indicates that there is a change in the configuration coordinates describing the energy levels for these pumping conditions. This may be associated with a multiphoton excitation process terminating at an energy far above

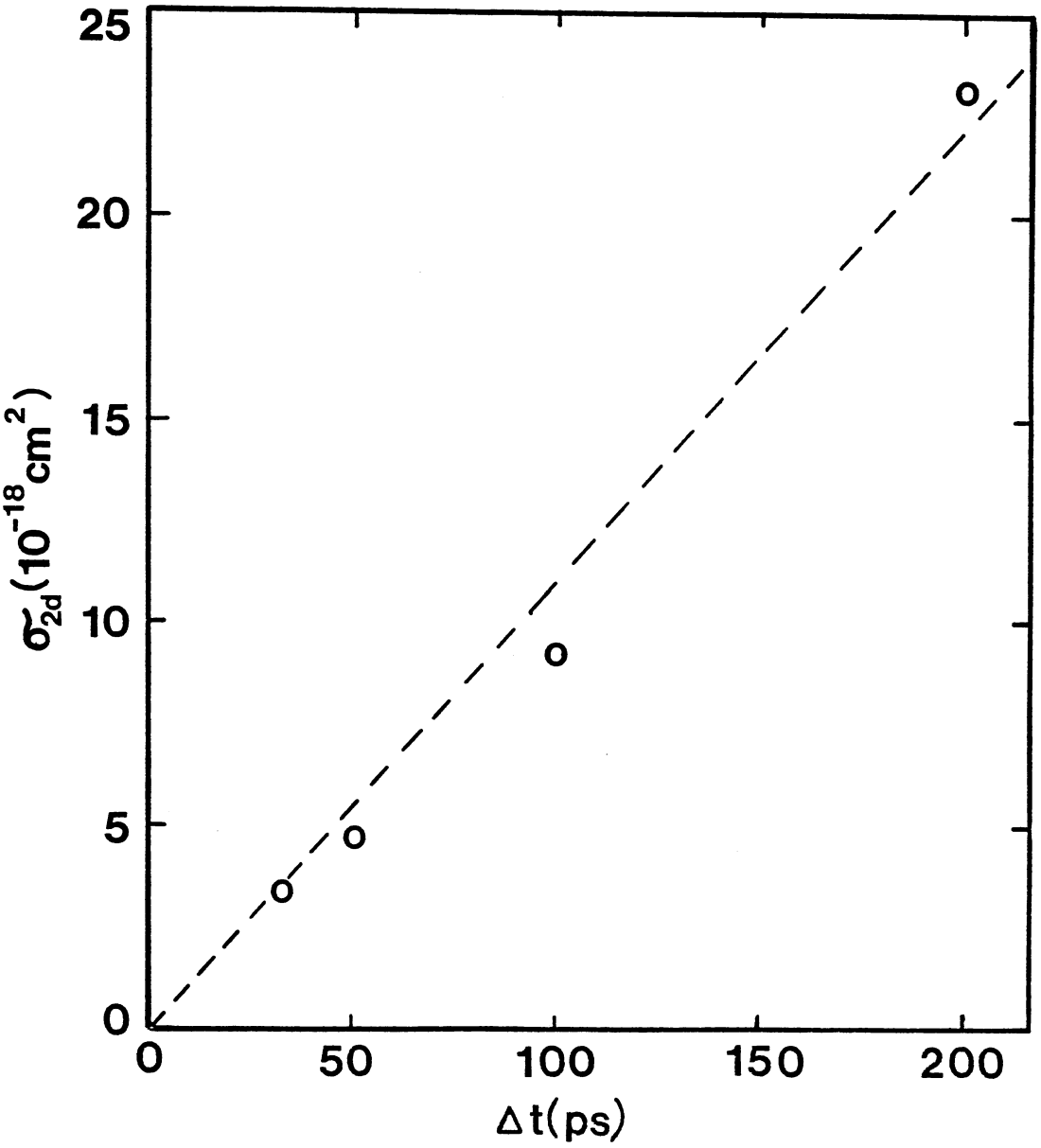

Figure 13. Variation of the Absorption Cross Section, σ_{2d}, of the Excited State Part of the STEP Transition Versus Laser Pulse Width for 532.0 nm Excitation

TABLE VI

TWO-PHOTON ABSORPTION CROSS SECTIONS AND PHOTON FLUX PER PULSE FOR VARIOUS PULSE WIDTHS FOR BZLT:Eu^{3+} UNDER 532 nm EXCITATION

Δt(ps)	σ_{2d}(cm^2)	I_p(photons/cm^2)
25	3.717×10^{-18}	4.365×10^{18}
50	4.703×10^{-18}	5.747×10^{18}
100	9.288×10^{-18}	5.820×10^{18}
200	2.322×10^{-17}	4.656×10^{18}

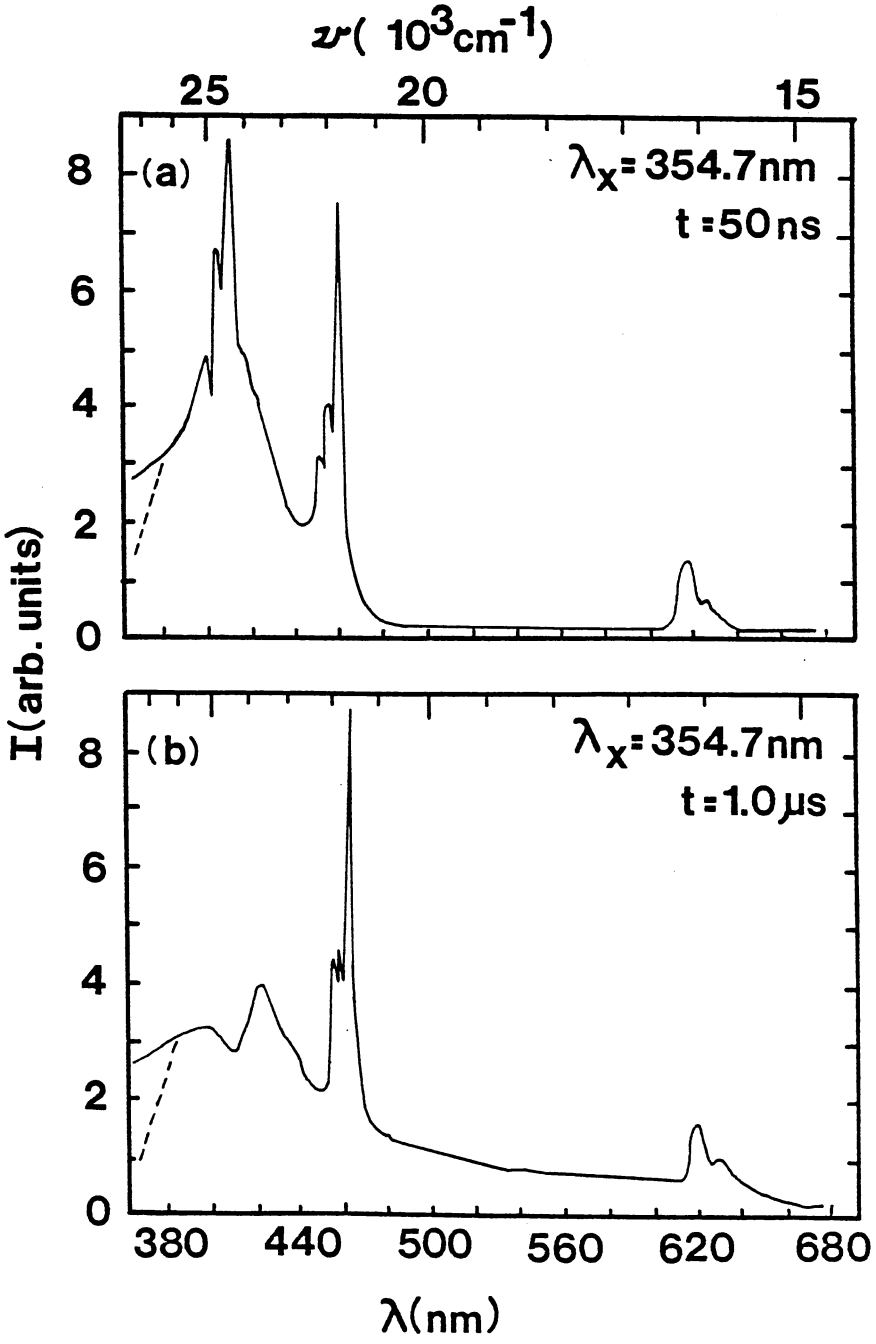

Figure 14. Fluorescence Spectra of BZLT:Eu^{3+} Glass at Two Different Times after the Excitation Pulse at 354.7 nm, (a) 50 ns and (b) 1.0 μs. The Dashed Line on the High Energy Edge Denotes the Corrected Spectra after the Overlap with the 354.7 nm Exciting Light is Taken into Account

the band edge. During the time the electron is in this highly excited state, the interaction of the ion with its surroundings will change through local polarization effects. The electron decays back down to the various metastable states and fluorescence occurs before the surrounding lattice has time to relax back to its equilibrium condition. It appears that in this polarized state of the local site of the ion, the 5d configuration level is shifted so that the bottom of its potential well falls below that of the $^5D_3$ metastable state. With these conditions no fluorescence comes from the latter level. Likewise, it is possible that multiphoton excitation with 354.7 nm lifts the electron into the charge transfer band located above 200 nm. Following this excitation, radiative transitions come from either the charge transfer states of the 5d band in addition to the ^5D_J levels. If there is a combination of radiative relaxation from both the charge transfer states and 5d bands, this could account for the double exponential decay curves observed with each transitions. Single photon excitation by 354.7 nm light in the LP:Eu^{3+} glass directly pumps the charge transfer state and gives a similar spectra to that seen in the fluoride glass. This spectrum shown in Figure 8c is taken at 50 μs after the 25 ps pulse. One difference is that the lifetimes in the oxide glass remain single exponential, indicating that there is no transfer or overlap between the 5d and charge transfer states. A schematic drawing of this model describing the change in the configuration coordinates is shown in Figure 15. This model is a qualitative model for describing the changes after 354.7 nm excitation. More work needs to be done to better understand the shifts in emission and changes in lifetimes. Future work is planned when the addition of a picosecond dye laser attachment is completed.

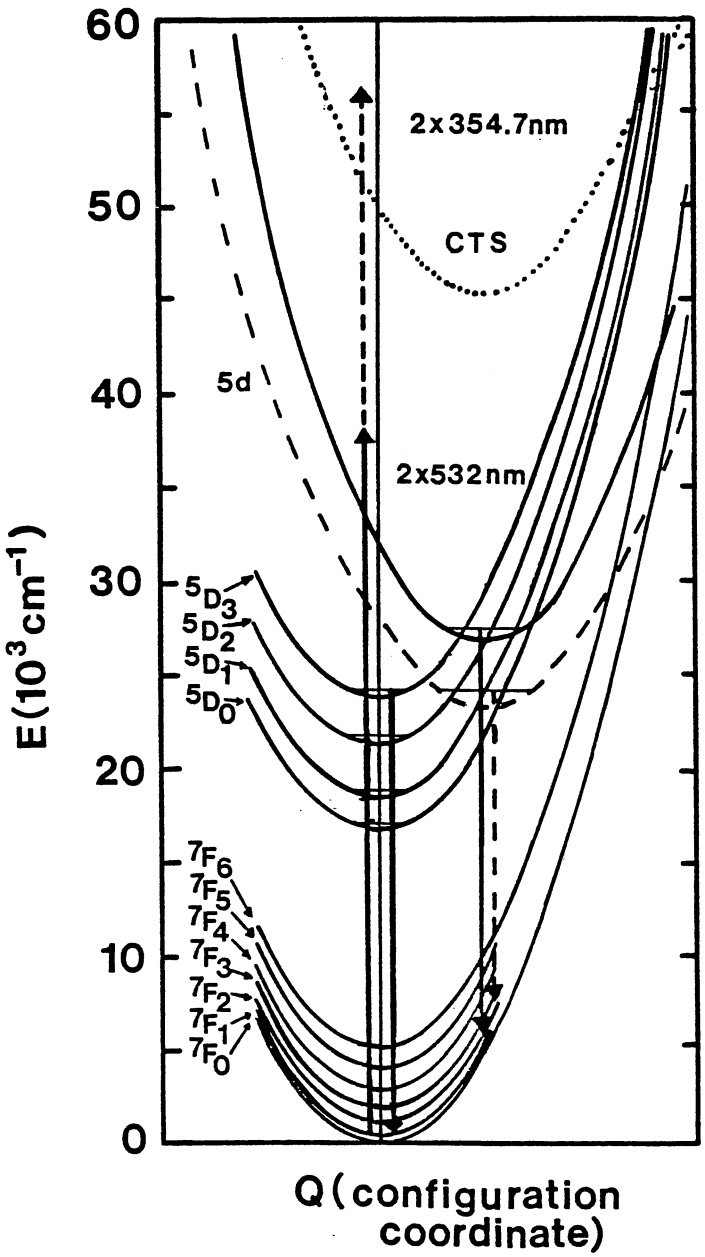

Figure 15. Configuration Coordinate Diagram Describing the Changes in the BZLT:Eu^{3+} Fluorescence after Multiphoton, 354.7 nm Pumping. The Solid Lines Represent the Location of the Levels after 266.0 nm and 532.0 nm Excitation. The Broken Line Represents Schematically the Shift in the 5d Potential Well Due to Local Polarization Effects Following the Multiphoton 354.7 nm Pumping. The Dotted Line Indicates the Position of the Charge Transfer Band Above the 5d Level

Discussion and Conclusions

Picosecond-pulse excitation is an important experimental method for characterizing the spectral dynamics of ions in solids. The time-resolved spectroscopy technique used here provides a useful means by which two-photon absorption cross-sections can be determined. These results, coupled with measurements of the excitation pulse width dependence of the cross section, allows the mechanism of two-photon absorption to be identified.

The results reported here show that Eu^{3+} ions in BZLT fluoride glass emit fluorescence from higher metastable states of the $4f^6$ configuration and from the lowest level of the 5d configuration. This implies weak electron-phonon interaction in BZLT:Eu^{3+} compared to many oxide glass hosts which exhibit fluorescence only from the $^5D_0$ level, or the $^5D_1$ and $^5D_0$ levels after radiationless relaxation from higher excited states (31). Layne and Weber (25) have shown that the weaker ion-phonon coupling decreases the rate of multiphonon emission in fluoride glasses, thus more fluorescence is observed from the rare earth levels in fluoride glasses than in oxide glasses. They claim that in their fluoride glass studies, the local fields at the rare-earth sites are weaker than in the oxide glasses, simply because in oxide glasses there is a larger charge and the bonding is typically more covalent.

Characterizing the properties of the $4f^5 5d$-$4f^6$ interconfigurational transition is especially interesting since this has not been extensively studied, whereas the CTS of oxide glasses similar to the LP glass have typically been more closely studied. High-power, picosecond-pulse excitation produces two-photon absorption in the BZLT glass which was shown to take place through a mechanism involving a coherent intermediate

state. The cross section for the second photon absorption in the TPA process is found to be significantly greater than that of the first photon absorption. This is because the former involves a f-d transition with a large density of final states while the latter is an f-f transition with a small density of final states (32). The results obtained on Eu^{3+} in the oxide glass provide less information on the spectral dynamics associated with high power, picosecond pumping. This is due to the fact that the faster radiationless decay processes in the oxide host result in strong fluorescence emission only in the lowest metastable state. This demonstrates one limiting aspect of the time-resolved spectroscopy technique used here, it depends on having fluorescence emission from levels pumped only by two-photon absorption transitions as well as emission from levels pumped by one-photon absorption.

No evidence of ESA processes was found for the fluoride glasses under these excitation conditions, and no VTEP were observed when the excitation wavelength was not very close to resonance with a real single photon transition. Multiphoton excitation to energies well above the band gap of the host allow a local distortion of the lattice to occur which leads to Eu^{3+} fluorescence from a distorted crystal field environment giving rise to very different spectral properties. These types of spectral shifts and lifetime changes have been observed in other types of materials under conditions of high energy excitation (33).

Comparing the results obtained on Eu^{3+} with those reported previously on Nd^{3+} shows that the type of TPA process taking place in trivalent rare earth ions under similar excitation conditions can be quite different depending on the nature of the final state of the transition. For the case of Nd^{3+} in $Y_3Al_5O_{12}$ (YAG) an f-f transition was

observed between the $^4I_{9/2}$ ground state and the $^2(F2)_{5/2}$ final state. The intermediate state for this TPA transition was the $^4G_{9/2}$ state, which is a real f intermediate state. This intermediate state was found to dominate the sum over intermediate states in the expression for the TPA cross section. Likewise, for TPA in Nd^{3+}, the $^4G_{7/2}$ level is not a metastable state and it was shown that the decay rate term, ξ, in the TPA cross-section equation is actually the fast nonradiative decay rate associated with that level. For a 25 ps pulse and 532 nm excitation, the TPA cross-section for Nd-YAG was calculated as 2.1×10^{-19} cm^2, whereas for BZLT:Eu the value of the TPA cross-section is 3.7×10^{-18} cm^2. There are several possible explanations for the higher value of σ_{2d} for BZLT:Eu^{3+}. First, TPA for Eu^{3+} involves an f-d transition, with a larger density of final states than the f-f transition for Nd^{3+}. Finally, the coherence time is typically faster than a nonradiative decay rate, thus the virtual or coherent real f intermediate states for Eu^{3+} were found to be important in the TPA transition.

CHAPTER III

STUDIES OF SPECTRAL AND SPATIAL ENERGY TRANSFER IN EMERALD

Introduction

The potential use of emerald as a highly efficient tunable solid state laser material (34-39) has generated renewed interest in understanding the details of the spectroscopic properties of this crystal. Although the general optical spectroscopic properties of emerald have been characterized (40-45), there are still important unanswered questions concerning the presence of multiple sites for the Cr^{3+} ions, the characteristics of energy transfer among the Cr^{3+} ions, and the details of radiationless transitions in the material. Reported in this chapter are the results of investigating the optical properties of emerald using several different spectroscopic techniques including time-resolved site-selection spectroscopy (TRSSS) and four-wave mixing (FWM). There are two main areas of consideration in this investigation: energy transfer and radiationless decay processes. The results presented here show that two very different types of energy transfer processes take place in this material. The first is a short range, nonresonant process between icns in nonequivalent crystal field sites while the second is a resonant, long range migration process. The radiationless transitions distributing the population of excited ions among the $^4T_2$ and ^2E levels are shown to be responsible for

the temperature dependence of the fluorescence intensity and lifetime for the dephasing time of the four-wave mixing signal.

Sample and Experimental Procedure

The emerald sample investigated in this work was rectangular with dimensions 7.5 mm x 13.0 mm x 3.8 mm and was dark green in color. The chemical composition of emerald is $Be_3Al_2(SiO_3)_6:Cr^{3+}$. Our sample was grown by the hydrothermal method and contained approximately 3% at. Cr^{3+} ions, which gives the number of Cr^{3+} ions per cubic centimeter in our sample to be $N_o = 1.77 \times 10^{20} cm^{-3}$. Emerald has the beryl structure with the Cr^{3+} ions substituting for the Al^{3+} ions and sitting at the center of a slightly distorted octahedral site, as is seen in Figure 16. The diameter of the Cr^{3+} ion is approximately 0.70 Å, which is 0.09 Å larger than the Al^{3+} ion (46), so the octahedral site is somewhat more distorted when the Cr^{3+} substitutes for the Al^{3+} ion. The site symmetry of Cr^{3+} in this lattice is (47,48) D_3 with a space group designated as P6/mcc and two molecules per unit cell (49). The dominant structure in beryl is the Si_6O_{18} rings which are linked by Be and Al. It is noted in Figure 16 that the first and second nearest neighbor distances for the Cr^{3+} sites are 4.6 Å and 5.3 Å, respectively (49). This is much larger than the 2.65 Å or 2.7 Å first nearest neighbor distances found in similar vibronic laser materials, ruby (50) and alexandrite (51). These larger distances between Cr^{3+} ions in emerald allow for high concentrations without appreciable concentration quenching of the fluorescence. However, the trade off is that the density of available sites for Cr^{3+} in beryl is $5.9 \times 10^{21} cm^{-3}$, which is approximately 12% of that in the corundum (ruby) lattice (45). For emerald doped with 3% at. Cr^{3+}, there

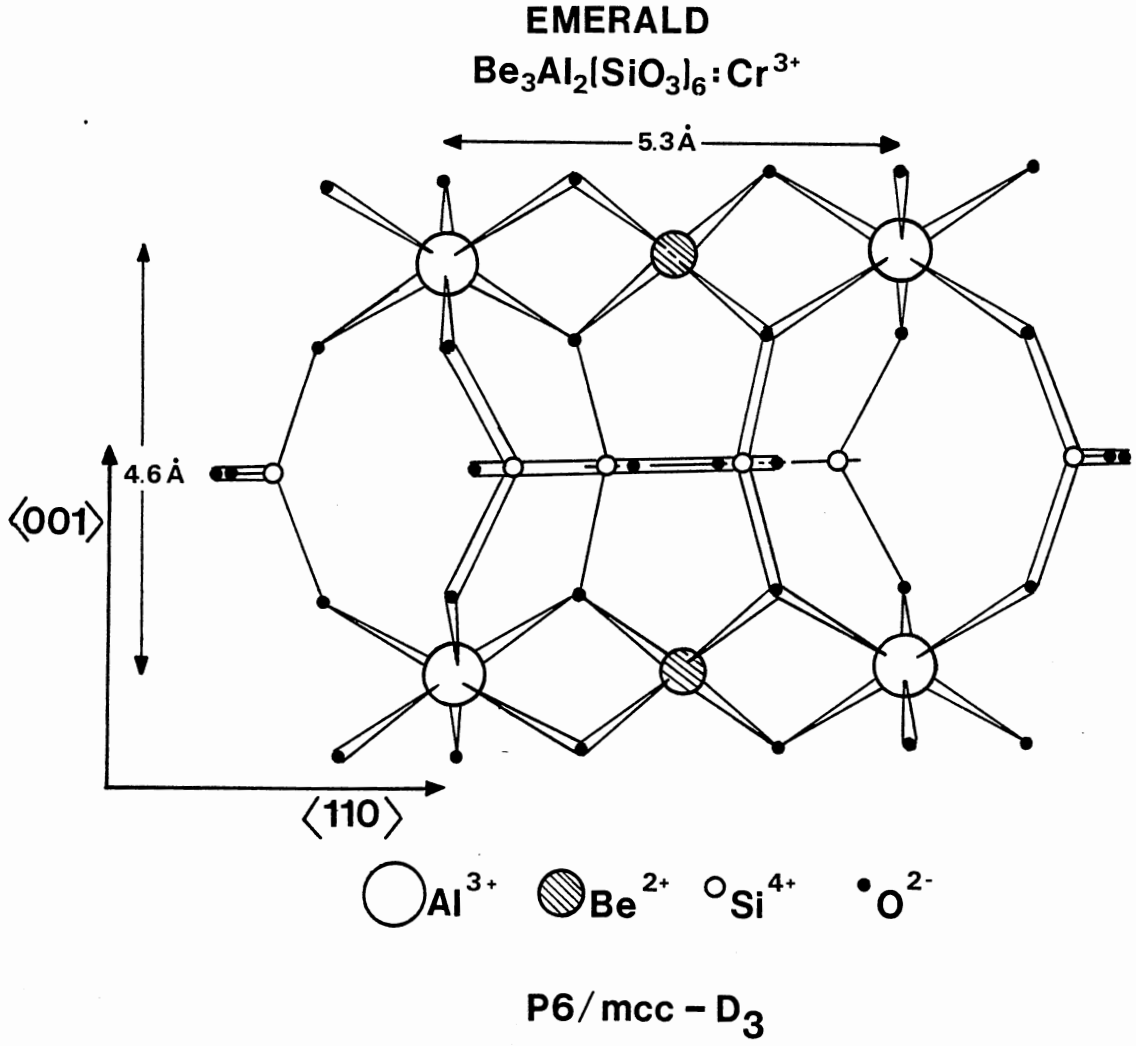

Figure 16. Crystal Structure of Beryl Projected onto a (100) Plane. Taken from Reference 49

is evidence for the presence of exchange coupled pairs of Cr^{3+} ions at this high level of concentration (49). In addition, there is also evidence for different types of nonequivalent crystal field sites for doping ions in this host (52).

The room temperature and low temperature absorption spectra for our sample were recorded using two different spectrophotometers, so that we could correlate the two measurements to determine the accuracy of the positions of the sharp lines. The absorption spectra were recorded using a Perkin-Elmer Model 330 Spectrophotometer and an IBM 9430 UV-Visible Spectrophotometer. The calibration of these instruments was checked using the lines from an Oriel Model 6032 neon lamp.

The experimental setup for the TRSSS is shown schematically in Figure 17. A Molectron UV-14 Nitrogen Laser and Dye Laser were used as the wavelength tunable source. This laser has a pulse width of approximately 10 ns and a variable repetition rate up to 20 Hz. The dye used for the TRSSS experiments was an Oxazine 720 Perchlorate dye, obtained from Exciton Chemical Company. The dye was a 1.0×10^{-3} M solution of 0 x 720P in a solvent of 40 ml ethanol. This involved using approximately 17.27 mg of the powdered dye. This dye lased in a wavelength range that was tunable from 660 nm to 720 nm. Through continuous tuning, the full-width at half maximum (FWHM) of the dye laser output was maintained at less than 0.6 Å in the region of interest. The output from the nitrogen-dye laser was focused on the sample, which was mounted on the cold finger of an Air Products Model DE202 refrigerator with a Model CS-202 compressor unit. This is a closed cycle helium refrigerator with the capability of continuously varying the sample temperature from about 12 K to above room temperature. The temperature on the sample was monitored and

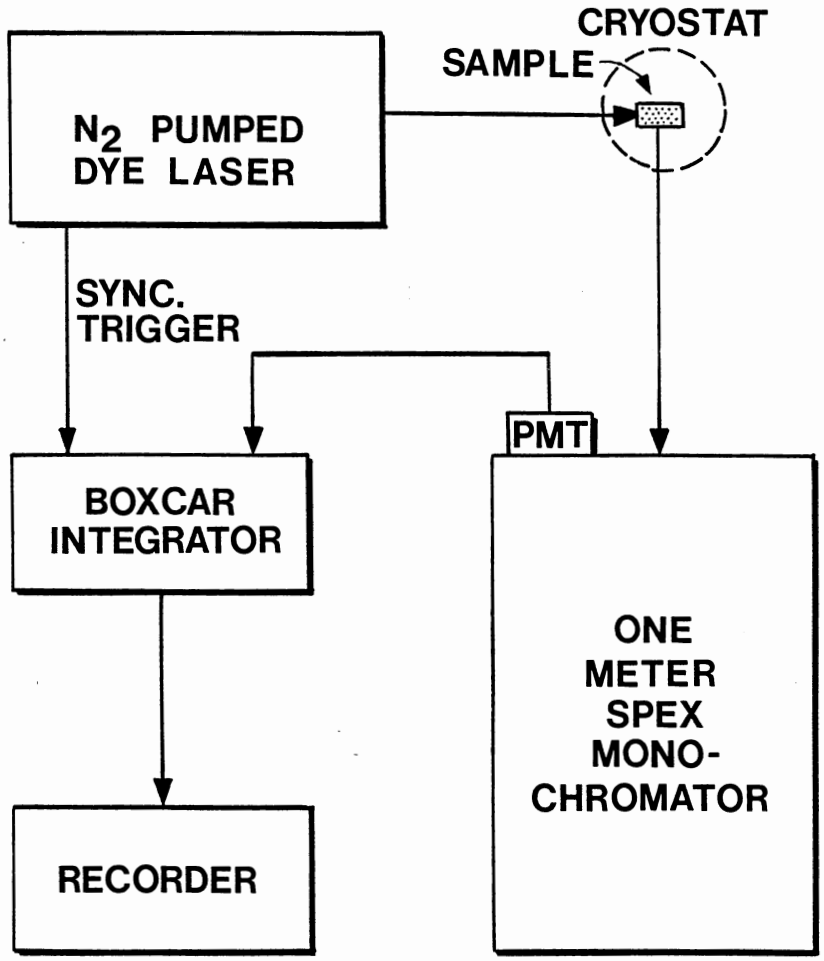

Figure 17. Experimental Apparatus for Time-Resolved Site-Selection Spectroscopy and Fluorescence Lifetime Measurements

varied using an Air Products Model 3700-APD-E Digital Temperature Indicator/Controller. Thermal contact between the sample and cold finger was aided by the application of a small amount of conducting grease. The temperature of the sample was measured by an Omega gold-constantan thermocouple.

The fluorescence of the sample was collected at a 90° angle with respect to the laser beam and was focused onto the entrance slit of a Spex one meter Czerny-Tuener spectrometer, Model 1704. This spectrometer has a 4 Å per mm dispersion with ultimate resolution of better than 0.1 Å in first order. For the TRSSS measurements, the input and output slits were maintained at 100 μm to insure a resolution of $\leq$0.4 Å in the region of interest. For the measurements of the position and FWHM of the laser line, the slits we held at <1 μm to insure a resolution of $\leq$0.1 Å. The output of the spectrometer was detected by an RCA-C31034 phototube operated at 1735VDC and purged with air. The phototube was cooled by a Products for Research Thermoelectric Refrigerated Chamber at about -20°C in order to minimize the dark current.

The output of the phototube was processed by a Princeton Applied Research Corp. model 162 Boxcar Averager with models 164 and 165 Processor Modules to form a gated signal recovery system. The Boxcar was triggered directly from the synchronous output from the nitrogen laser. The Boxcar has a time apperature that can be continuously adjustable from 10 ns to 5 ms and can be set fixed or scanned along a delay range from 3% to 100% of the range. The delay range is adjustable from 0.1 ns to 50 ms and the scanning time can be set anywhere from 10^{-2} s to 10^{5} s. For the time resolved fluorescence spectra an input load of 500 kΩ was used and held constant for all the fluorescence spectra.

Fluorescence lifetime and risetime measurements for the TRSSS experiment, were performed using the same experimental apparatus described above. By setting the spectrometer on a fixed frequency, whose lifetime is to be measured, and scanning the aperature along a properly selected delay range at each given small time interval after the laser pulse, the aperature of the boxcar determines the average magnitude of the fluorescence signal at the same small time interval after the laser pulse. So, by allowing the aperature to scan, it was possible to record the average shape in time of the fluorescence signal and thus measure the lifetime. Again, a variable input load resistor was used to minimize the response time of the system. This input load was typically set at $\leq$138 kΩ for the time resolved fluorescence lifetime and risetime measurements.

The experimental apparatus for the nondegenerate FWM spectroscopy setup is shown schematically in Figure 18. The source of the "write" beams is a Spectra Physics Model 164 argon-ion laser which pumps a Spectra Physics Model 380 ring-dye laser. The dye used in this work was a Rhodamine 6G Dye, which was tuned to pump resonantly the $^4T_2$ band at 588.0 nm. The output of the ring-dye laser is split with a 50% beam splitter (BS) and then is focused onto the sample using concave mirrors (M). The two write beams are denoted as beams $\vec{E}_1$ and $\vec{E}_2$ in Figure 19. The crossing angle of the two "write" beams is defined as 2θ and their interference forms a sine wave pattern which acts as an index of refraction grating. The emerald sample is mounted in a CTI Cryogenics Model 22 Refrigerator with a Model SC Compressor. Again the temperature is controlled and monitored using the same equipment described previously. The write beams are chopped by an HMS Model 221 Lightbeam Chopper and are

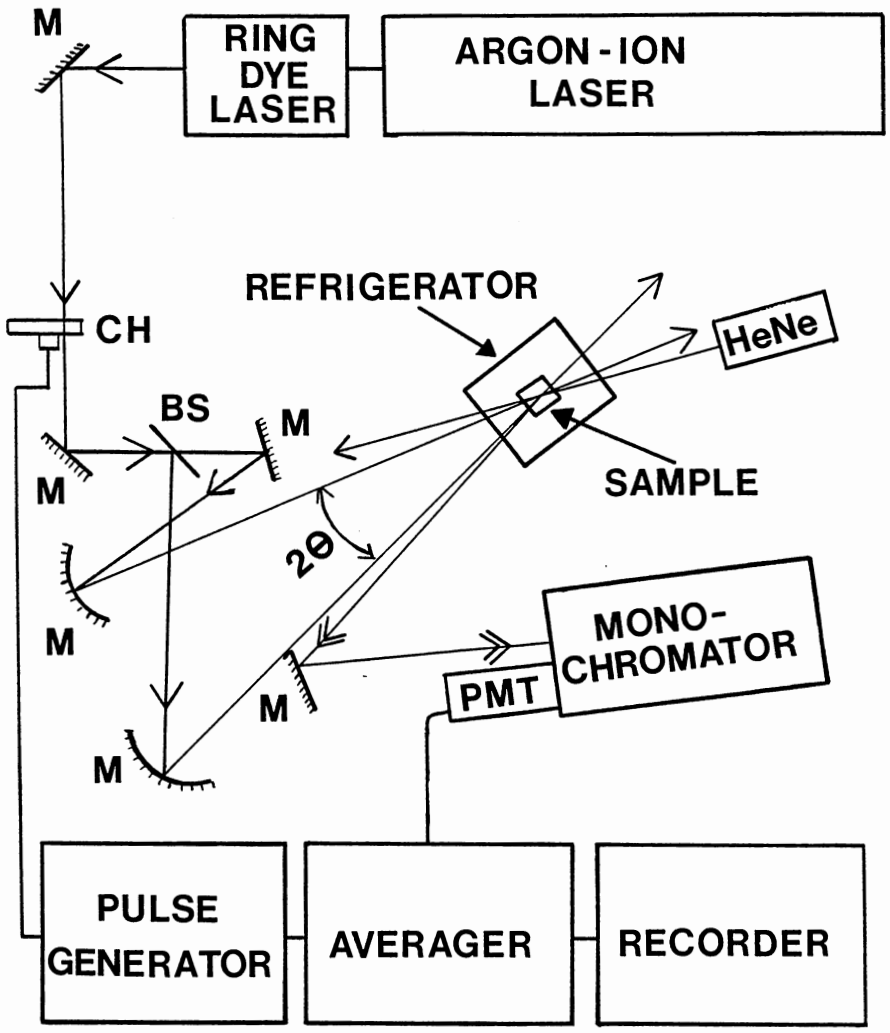

Figure 18. Experimental Apparatus for Four-Wave Mixing Scattering Efficiency and Grating Lifetime Measurements

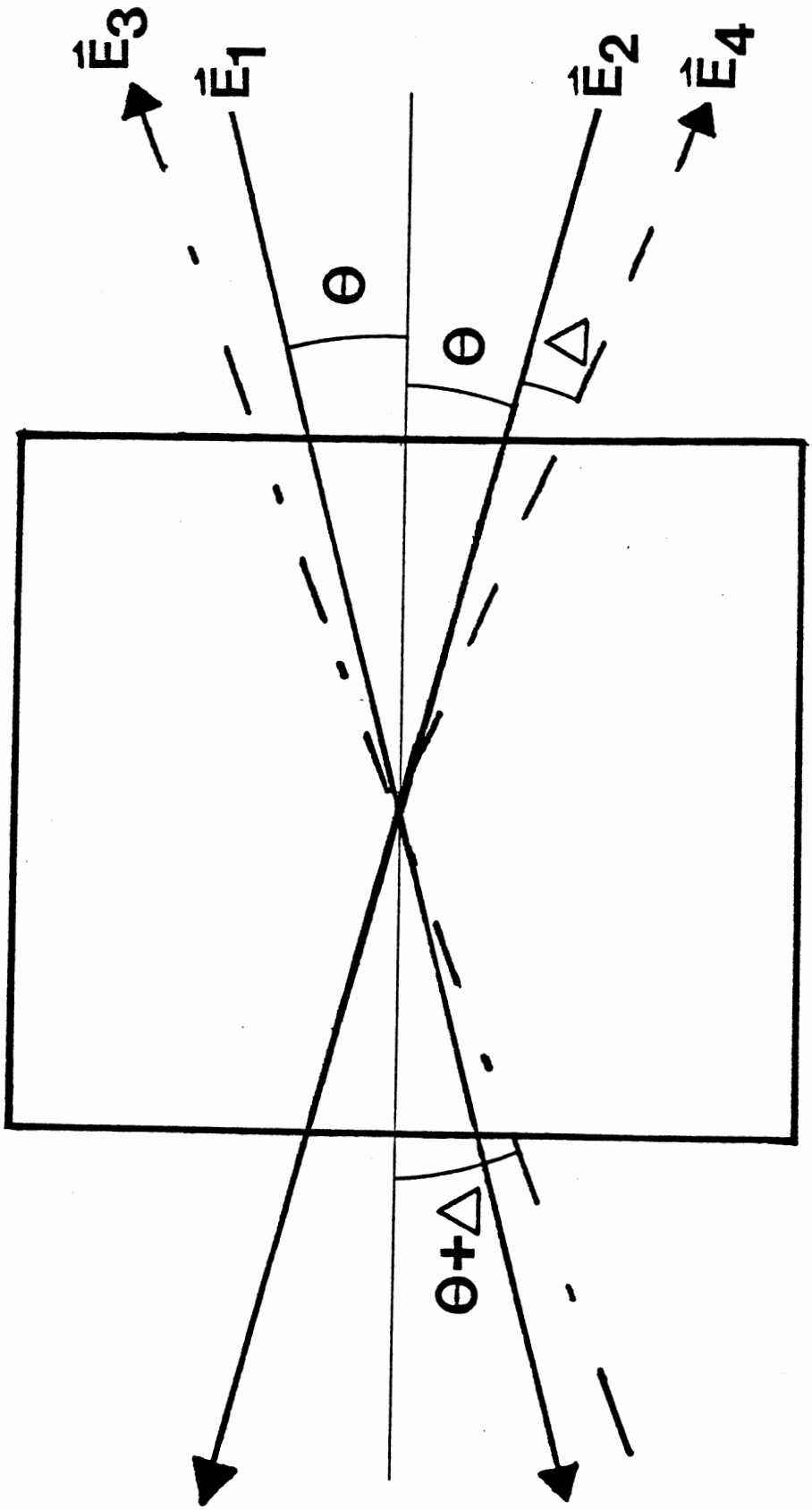

Figure 19. Laser Beam Geometry in Four-Wave Mixing

weakly focused inside the sample. The chopper was used to turn off the write beams at a variable frequency for the grating lifetime measurements. Care was taken to ensure that the difference in their optical path lengths was less than the coherence length of the laser. A probe beam at 632.8nm denoted as $\vec{E}_3$, from a Hughes 15mW Model 3227H-PC Helium-Neon laser, enters the sample nearly counterpropagating to one of the write beams, and a signal beam shown as $\vec{E}_4$ in Figure 19 or depicted by the line with double arrows in Figure 18, is defracted off of the grating and sent to a photomultiplier tube. The signal is collected in a Pacific Instruments Model MP-1018B 1/2-meter Monochromator and detected with a model PM2254B Amprex photomultiplier tube. The signal is then monitored and stored using jointly an HP8013B Pulse Generator and an HP Model 4202 Signal Averager. The data is then recorded on a strip chart recorder.

General Optical Spectroscopy

Although some of the general optical spectroscopic properties of emerald have been characterized (40-44), it is necessary to record and understand the properties of this individual sample. Shown in Figure 20 is the absorption spectrum for the Cr^{3+} ions in emerald at 70 K. The peaks in the absorption spectrum are labeled in terms of the octahedral crystal field designations of the final state of their transitions from the $^4A_2$ ground state. These designations are also used in Figure 21, which shows the partial Sugano-Tanabe diagram for Cr^{3+} ions in different host crystals, all of which are also vibronic laser materials. This diagram depicts the energy levels of the $(3d)^3$ electronic configuration in an octahedral crystal field as well as how the change in the strength of this octahedral component of the crystal field site of Cr^{3+} ions

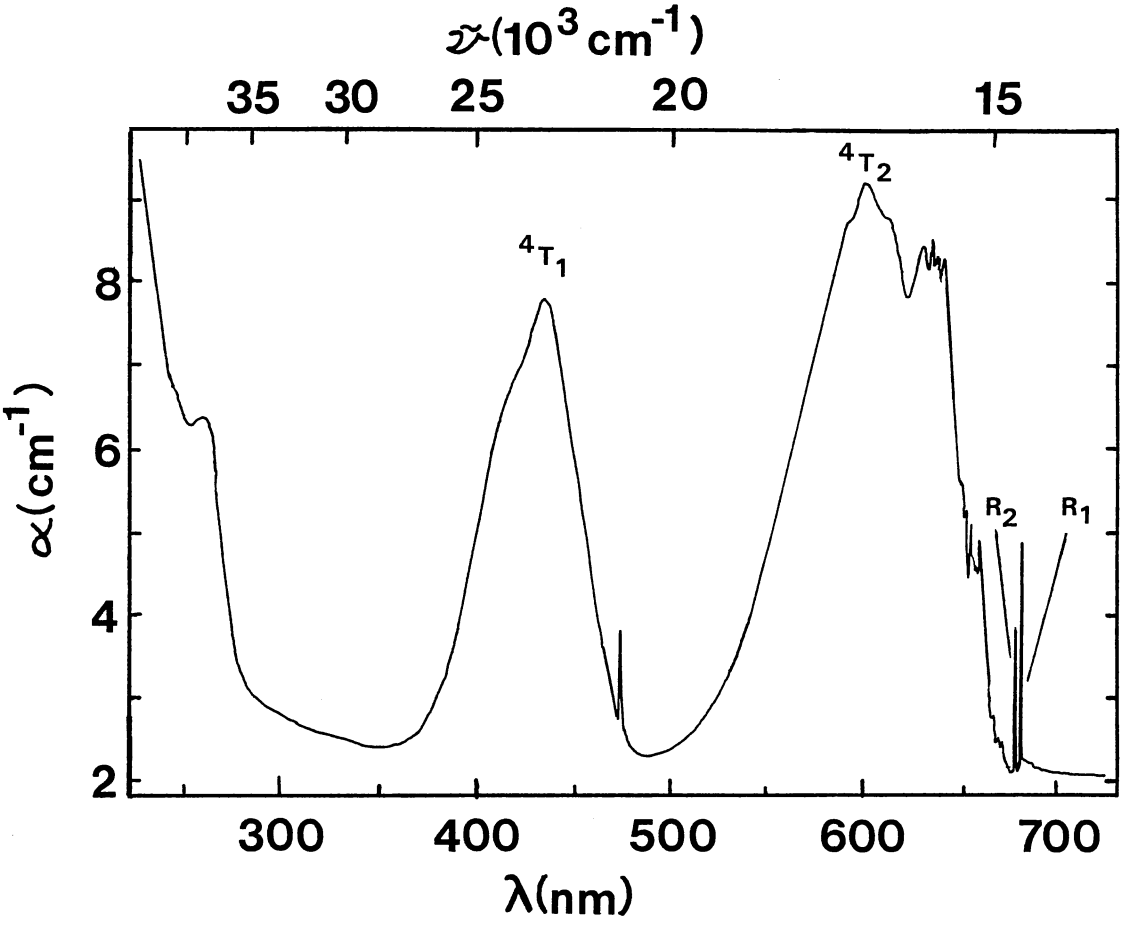

Figure 20. Absorption Spectrum of Emerald with 3 at.% Cr^{3+} at T=70 K

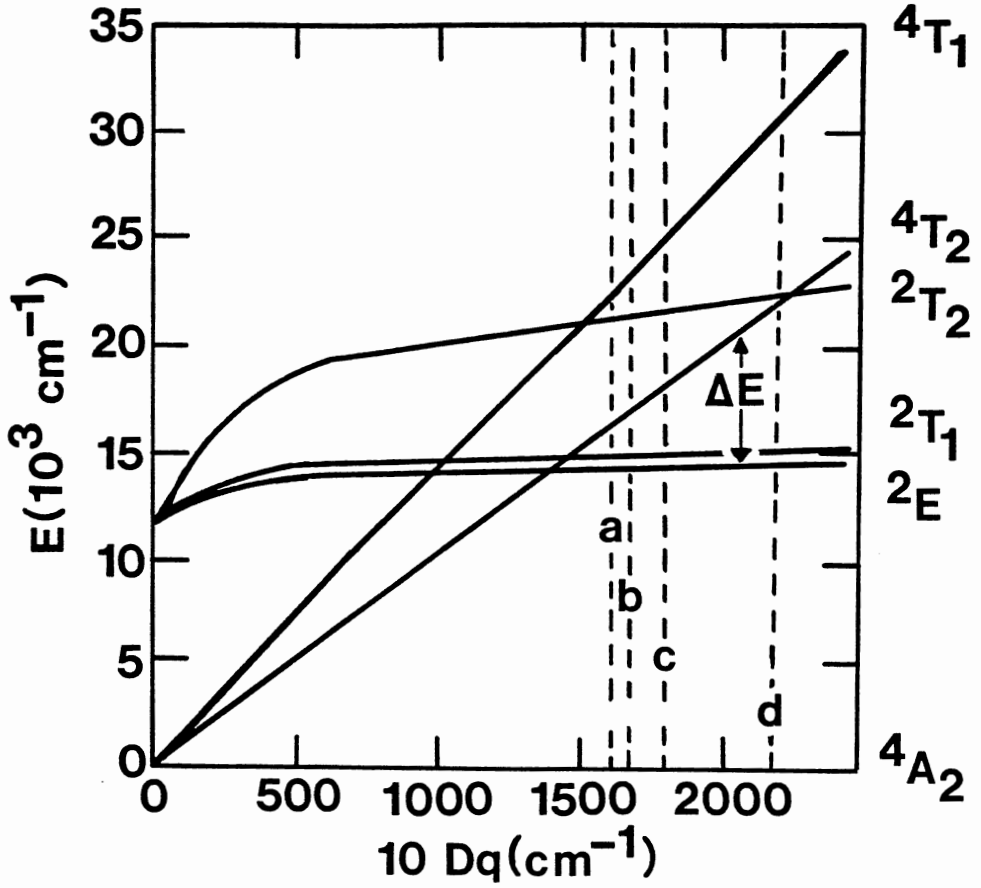

Sample	ΔE(cm^{-1})
a. Emerald	400
b. Alexandrite-M	800
c. Ruby	2300
d. Alexandrite-I	6400

Figure 21. Partial Sugano-Tanabe Diagram for Cr^{3+} Ions in Different Vibronic Laser Host Crystals

alters the splitting between the $^4T_2$ and ^2E levels, designated by ΔE. Figure 22 shows the energy level diagram specifically for Cr^{3+} ions in emerald. Labeled in this figure are the lasing transition, which originates from the $^4T_2$ level and terminates on a band of vibrationally excited ground electronic states. This band of vibrational states gives emerald a broadly tunable range from 670 nm to 850 nm (34-39). Also labeled in Figure 22 are the R_1 and R_2 lines, which are associated with transitions between the ^2E states and the $^4A_2$ state.

The fluorescence spectra of emerald at 70 K is shown in Figure 23. The fluorescence is associated with zero-phonon transitions from the crystal field split components of the ^2E level (the sharp R-lines) and broad band fluorescence which is a superposition of the vibronic sidebands of the R lines and emission from the $^4T_2$ level. As the temperature increases, the R-line emission decreases until, at 190 K, the strength of the intensity of the R-lines fluorescence and the broad band fluorescence are equal. Another detail to note is that the $^4T_2$ emission is Stokes shifted to lower energy (i.e., below that of the ^2E). This is one factor which makes emerald a very efficient vibronic laser at room temperature (39).

Figure 24 shows in higher resolution the overlap of the absorption and fluorescence spectra in the region of the R-lines at 70 K. This spectra is uncorrected for polarization effects. Both fluorescence and absorption spectra were taken from 10 K to 300 K, but the structure in both the R_1 and R_2 lines becomes most visible around 70 K. These lines are inhomogeneously broadened with large linewidths, consistent with results reported previously (53). The fluorescence spectra, shown in Figure 24, were taken using cw excitation from the argon-ion laser at

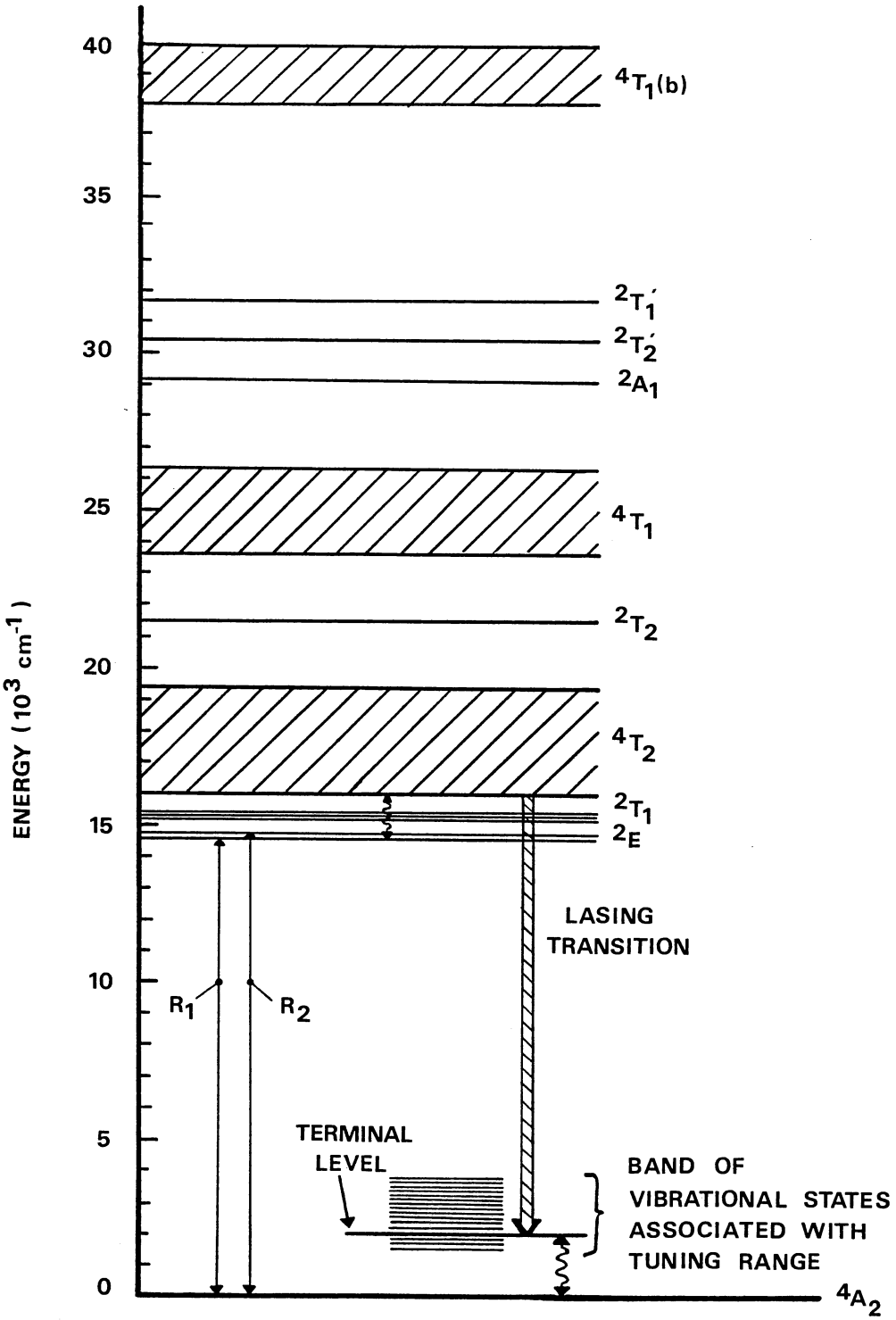

Figure 22. Energy Level Diagram for Cr^{3+} Ions in Emerald

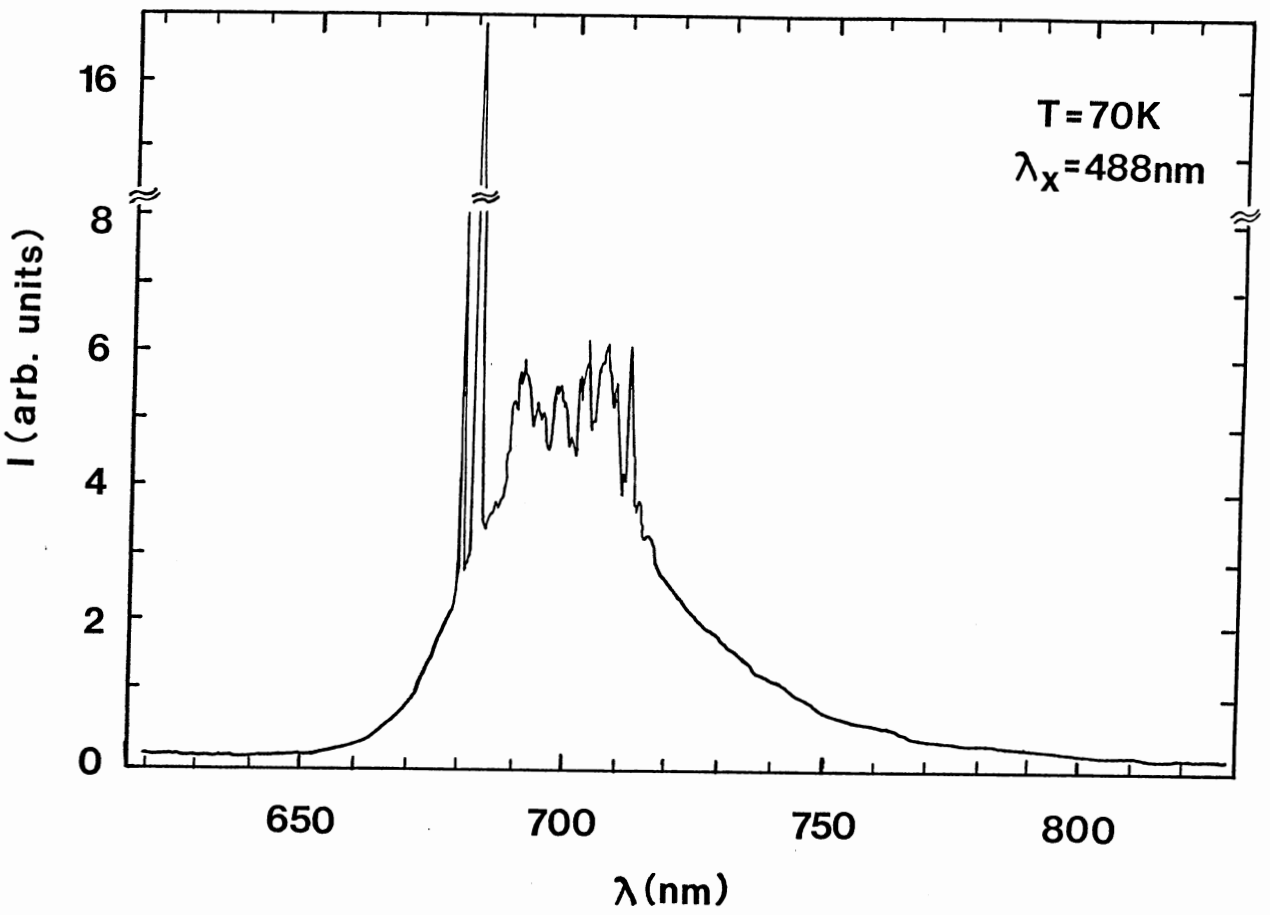

Figure 23. Fluorescence Spectrum of Emerald with 3 at.% Cr^{3+} at T=70 K Using 488 nm Excitation from an Argon Ion Laser

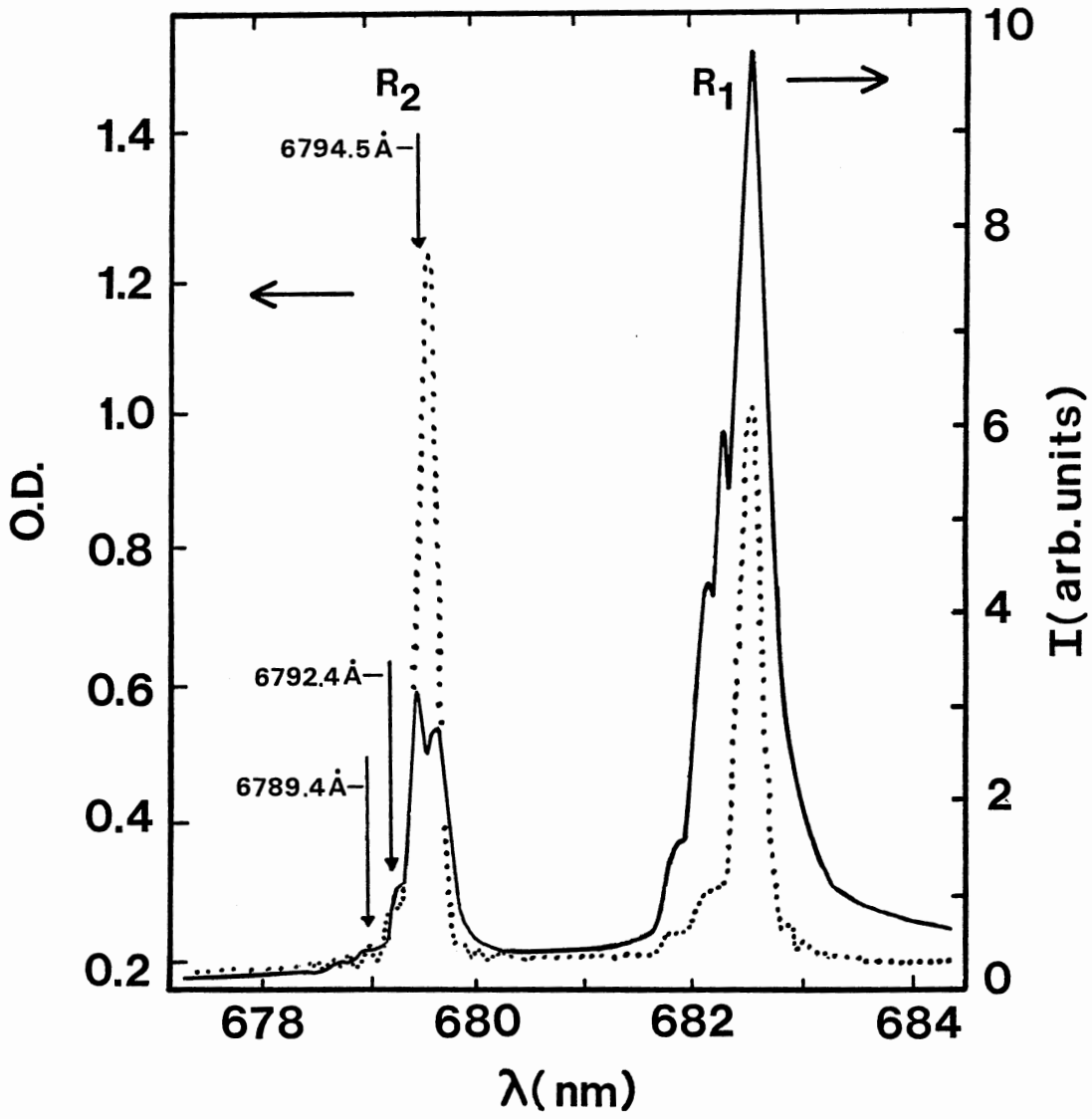

Figure 24. High Resolution Fluorescence and Absorption Spectra of the R-lines in Emerald at 70 K. The Solid Line is the Fluorescence Intensity and the Dots Represent the Absorption Spectra. The Vertical Arrows Indicate Excitation Wavelengths Used in Site Selection Spectroscopy

488.0 nm. Both of the R-lines in fluorescence exhibit a structure consisting of four peaks, and some structure is also observed in the absorption lines. The positions of these components are listed in Table VII. A large part of the absorption and luminescence spectra for each of the R lines overlap each other. Each peak is designated with superscripts in Table VII, but it is not clear how the peaks in R_1 correlate with those in R_2. Assuming that each of the peaks is associated with a nonequivalent crystal field site for the Cr^{3+} ion, it is possible to estimate the relative concentrations of the different Cr^{3+} sites from the absorption measurements of the R-lines. These values are listed in Table VIII, assuming the same oscillator strength of the $^4A_{2g} \longrightarrow {}^2E_g$ transition for each site.

In order to check if the observed splitting of the R-lines in the emerald sample is connected with the existence of multiple chromium sites in the crystal, the excitation spectra of the different components of the R_1 lines were measured. The spectra were recorded for λ_1 = 681.9 nm and λ_2 = 682.7 nm, hence for both wings of the R_1 line at 12 K, and are shown in Figure 25. The spectral resolution of the analyzing monochromator was approximately 0.2 nm. The results of the measurements showed that there was no difference between the excitation spectra recorded for either wing of the R_1 line. This may be due to either the relatively low resolution of the excitation spectra measurements or by the similarity of the absorption spectra of the different chromium sites in emerald.

The decay kinetics of the fluorescence under cw pumping conditions at 454.7 nm were monitored using a boxcar integrator. The signals were found to be single exponential decays over two decades between 12 and 200 K. The decay time of the fluorescence was 1.7 ms below 60 K. This

TABLE VII

SPECTRAL PROPERTIES OF THE R-LINES OF EMERALD WITH 3 at.% Cr^{3+}

R line	λ (nm)	
	absorption	fluorescence
R_1^a	681.55	--
R_1^b	681.80	681.80
R_1^c	682.25	682.20
R_1^d	--	682.30
R_1^e	682.60	682.60
R_2^a	678.80	--
R_2^b	678.95	678.95
R_2^c	679.24	679.25
R_2^d	679.56	679.50
R_2^e	--	679.65

TABLE VIII

DIFFUSION COEFFICIENTS AND RELATIVE CONCENTRATIONS OF Cr^{3+} IONS IN DIFFERENT SITES

Site	$N_i (cm^{-3})$	$D (cm^2/s)$
(a) - highest energy	1.720×10^{18}	4.6×10^{-13}
(b) - middle energy	3.680×10^{18}	9.4×10^{-13}
(c&d)* - lowest energy	1.716×10^{20}	2.5×10^{-11}
(e)**	-	-

*The fluorescence from time-resolved site-selection spectroscopy does not resolve site "c" thus, sites "c" and "d" are integrated together.
**Site "e" does not have a strong enough emission to accurately perform any integrations.

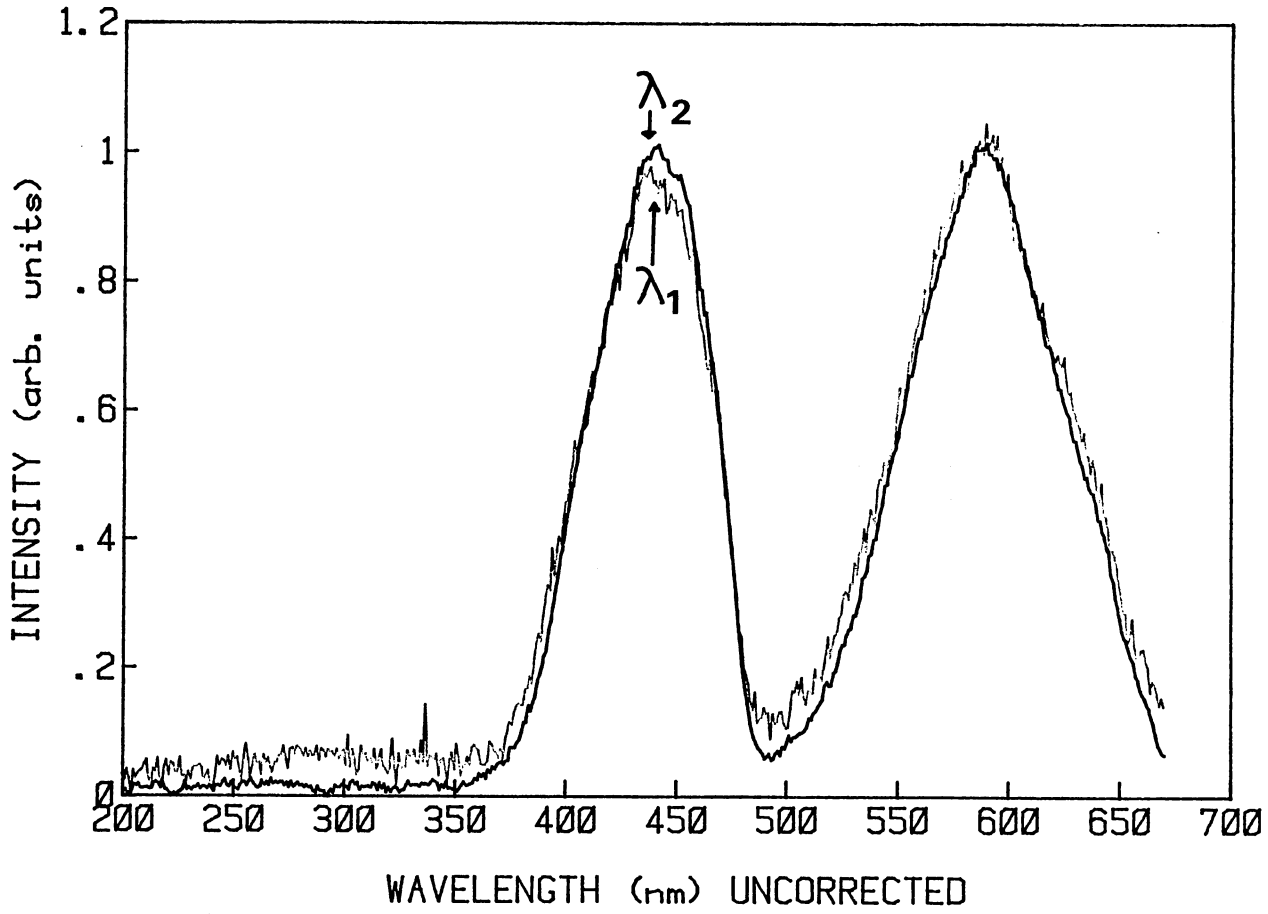

Figure 25. Excitation Spectra of the Different Components of the R_1 Lines, Recorded at 12 K for λ_1 = 681.9 nm and λ_2 = 682.7 nm

is slightly longer than the low temperature lifetimes reported by Kisliuk and Moore (54) and by Hassan, et al. (45). In both of these cases it was suggested that traces of Fe^{2} ions quenched the Cr^{3+} fluorescence. Above 60 K the lifetime decreases with increasing temperature due to thermal population of the $^4T_2$ level. The temperature dependence of the fluorescence lifetime is shown in Figure 26, with the associated values listed in Table IX.

A theoretical prediction for the temperature dependence of the fluorescence lifetime can be obtained from the expression

$$\tau^{-1} = \frac{\tau_E^{-1} + \tau_T^{-1} \exp(-\Delta E/k_B T)}{1 + \exp(-\Delta E/k_B T)} \quad . \tag{3-1}$$

Here it has been assumed that the ^2E and $^4T_2$ levels are separated by an energy ΔE and their populations are in thermal equilibrium. τ_E and τ_T are the intrinsic lifetimes of these levels and it is assumed that the intermediate $^2T_1$ levels do not play a significant role in the spectral dynamics (54). Equation (3-1) can be simplified further by assuming that the denominator is approximately equal to unity, thus giving

$$\tau^{-1} \simeq \tau_E^{-1} + \tau_T^{-1} \exp(-\Delta E/k_B T) \quad . \tag{3-2}$$

Using Equation (3-2), with the intrinsic lifetimes and the energy gap treated as adjustable parameters, the best fit to the data is shown as a solid line in Figure 26. The value of the energy gap between the ^2E and $^4T_2$ levels, ΔE, is found to be equal to 381 cm^{-1}, which is in good agreement with previous reported values of 380 cm^{-1} and 388 cm^{-1} reported by references (54) and (55), respectively. The intrinsic decay time of the $^4T_2$ level was found to be 14 μs which is between the values found

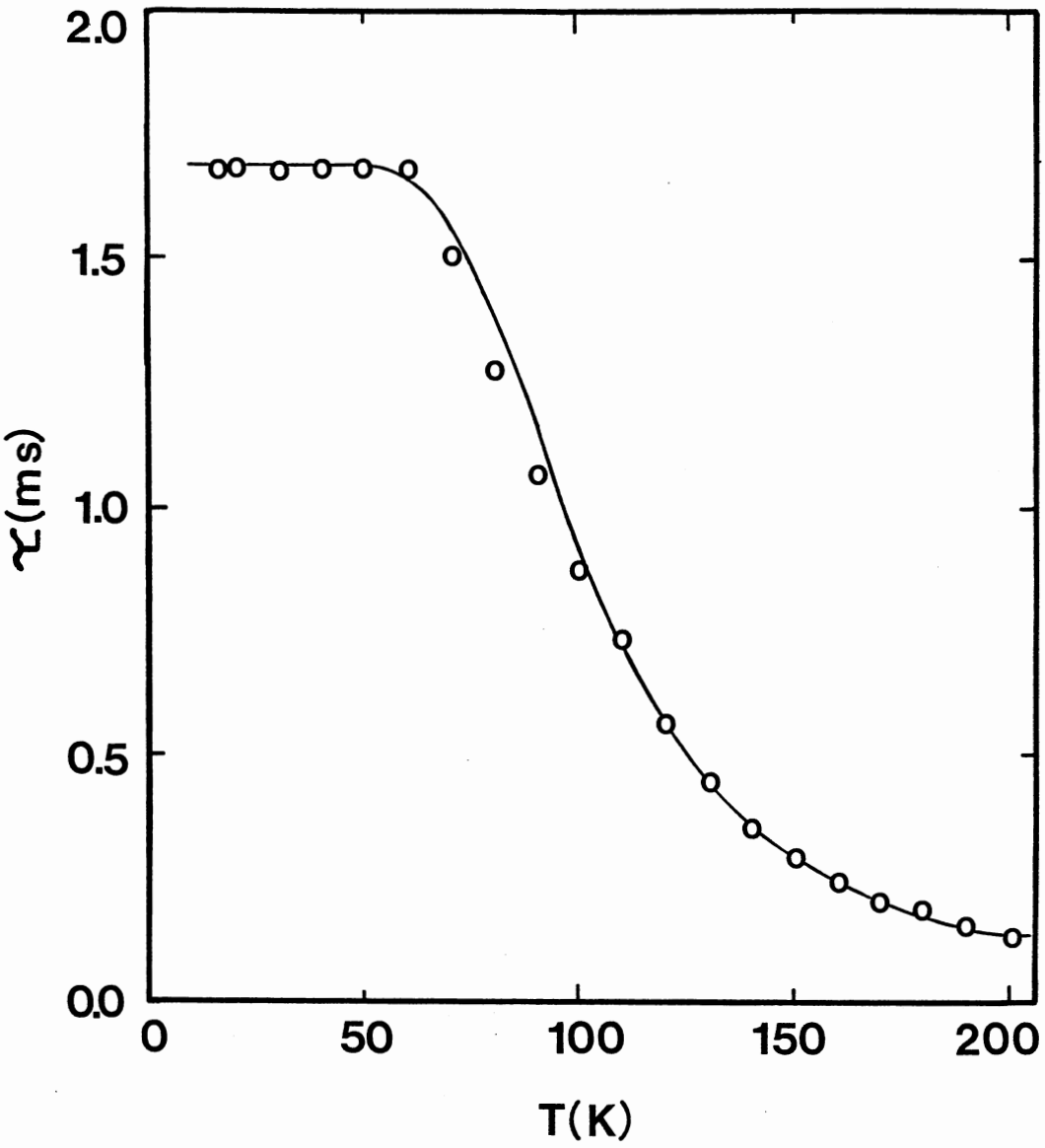

Figure 26. Temperature Dependence of the Fluorescence Lifetime of Emerald Under cw Excitation Conditions at 454.7 nm

TABLE IX

FLUORESCENCE LIFETIMES OF EMERALD AS A FUNCTION OF TEMPERATURE UNDER cw EXCITATION CONDITIONS AT 454.7 nm

τ(ms)	T(K)
1.698	15.6
1.709	20
1.708	30
1.709	40
1.708	50
1.710	60
1.504	70
1.278	80
1.064	90
0.876	100
0.727	110
0.560	120
0.445	130
0.353	140
0.293	150
0.244	160
0.205	170
0.187	180
0.153	190
0.130	200

from previous investigations (45,54). The parameters used in obtaining this fit are listed in Table X.

There are two other possible ways to estimate the value of ΔE from the spectroscopic data obtained. First, for $\tau_T << \tau_E$, which is applicable for this case, the expression in Equation (3-2) indicates that there is a region of temperature in which τ should be proportional to $\exp(\Delta E/kT)$. From Figure 26, this value is found from the slope between 70 K and 110 K to be 380 cm^{-1}. This case gives very good agreement. The second case involves observing the absorption spectrum in Figure 20. If ΔE is estimated to be 381 cm^{-1}, then by observing that the R_1 absorption peak is located at 682.5 nm (14652 cm^{-1}), it should be possible to predict that the lowest no-phonon $^4T_2$ absorption peak whould lie at 665.3 nm (381 cm^{-1} + 14652 cm^{-1} = 15033 cm^{-1}). From Figure 20, there is a peak in the structure at 666.0 nm, thus implying good agreement once again.

Energy Transfer Models

Energy transfer is a process which can take place in a material whenever a material is exposed to light. This exposure to light may cause energy to be absorbed through the creation of electronic excited states. The active ions which absorb this energy are referred to as sensitizers. This energy may later be emitted in the form of light or heat by the active ions which are referred to as activators. In order for the activator to emit part of the energy absorbed by the sensitizer, energy transfer must take place between the sensitizer and activator. The transfer mechanism can either be an electromagnetic multipole-multipole interaction or an

TABLE X

SPECTROSCOPIC PARAMETERS OF EMERALD

ΔE	381 cm^{-1}
τ_T	14 μs
τ_E	1.7 ms
Ω(T=13 K)	2.06 x 10^{-2} cm
Ω(T=50 K)	1.76 x 10^{-2} cm
Ω(T=85 K)	1.43 x 10^{-2} cm
Ω(T=100 K)	2.98 x 10^{-3} cm

exchange interaction. This transfer is usually thought of in terms of a quantum mechanical process in which the exchange takes place through a virtual photon. Energy transfer is typically treated in one of two limiting cases. The first involves a direct transfer from an excited sensitizer to an unexcited activator. This single-step process has been developed theoretically by Förster (56) and Dexter (57) in two separate classical papers, with further focused development added by Holstein, et al. (58) and Huber et al. (59). The second case is that of energy transfer to activators after multistep diffusion among sensitizers. The quasi-particle involved in this multistep transport process is called an exciton. The exciton migrating on a lattice of sensitizers can be considered to be a localized exciton, referred to as a Frenkel or Davydov exciton (60). The description of this exciton diffusion energy transfer was first developed by Frenkel (61), Trlifaj (62), and Förster (56). Typically, single-step energy transfer takes place whenever the sensitizer concentration is very low or whenever the sensitizer-activator interaction is much stronger than the sensitizer-sensitizer interaction. However, this is not the case for the short range spectral transfer found in emerald through TRSSS, so the emphasis on the theoretical development here will be on the second case, that of multistep diffusion.

When working with multistep transfer, both the sensitizer-sensitizer interaction and the sensitizer-activator interaction will be either a multipole-multipole interaction or an exchange interaction, and these may be different for the sensitizer-sensitizer and sensitizer-activator interactions. Thus the characterization of multistep energy transfer involves describing both the sensitizer-sensitizer migration and

describing the sensitizer-activator trapping. This problem is generally approached either from a random walk model or a diffusion model (56, 62-64).

For the case of spectral diffusion in emerald, the important theoretical models assume that the exciton migration can be described as a diffusional process with the activators acting as point traps. In treating the problem of spectral diffusion, an equation describing the time evolution of excited sensitizer states $n_s(\underset{\sim}{r},t)$, after a δ-function excitation pulse, can be written as

$$\frac{\partial n_s(\underset{\sim}{r},t)}{\partial t} = -\beta_s n_s(\underset{\sim}{r},t) + D\nabla^2 n_s(\underset{\sim}{r},t) - \sum_i \beta_s \left(\frac{R_o}{r_i}\right)^6 n_s(\underset{\sim}{r},t). \quad (3\text{-}3)$$

This equation accounts for the activator trapping properties and explicitly takes into account the sensitizer-activator interaction, with β_s being the sensitizer intrinsic decay rate, D is the coefficient for spectral diffusion, and r_i is the separation for a given sensitizer-activator pair. The last term in Equation (3-3) is sometimes written with a parameter α, describing the single-step transfer between a sensitizer and activator and defined as $\alpha' = \beta_s R_o^6$. The solution to Equation (3-3) must be averaged over the configuration of the activator distributions seen by each sensitizer, with most standard theories also assuming a uniform activator distribution. There has been no general solution found for Equation (3-3), however, two different solutions have been developed for special limiting cases and both of these cases assume that the interaction mechanism is electric dipole-dipole.

The first solution of Equation (3-3) comes from the work of Yokota and Tanimoto (7) in which they have treated the special case of weak

diffusion as a small perturbation on the stronger sensitizer-activator interaction. In order to see the limits of applicability of the Yokota-Tanimoto theory, the explicit solution to Equation (3-3), assuming the weak diffusion perturbation, can be written as

$$n_s(t) = n_s(o)\exp\{\beta_s t\}\left[\frac{1}{V}\int_o^{R_v} 4\pi r^2 \exp(tD\nabla_r^2 - \alpha r^{-6}t)\,dr\right]^{N_a} \qquad (3\text{-}4)$$

where, as mentioned before, a uniform distribution of activators has been assumed, n_s is the result of summing over all excited sensitizers, N_a is the number of activators, and the total volume of the sample is represented by the factor $V = 4\pi R_r^3/3$. Since ∇_r^2 and r^{-6} are Hermitian, it is possible to make use of an operator expansion

$$\exp(tD\nabla_r^2 - \alpha r^{-6}t) = \exp(-\alpha r^{-6}t)\left\{1 + \sum_{n=1}^{\infty}(-1)^n \int_o^t dt_1 \cdots \int_o^{t_{n-1}} dt_n U(t_1)\cdots U(t_n)\right\} \qquad (3\text{-}5)$$

where

$$U(t) = \exp(t\alpha r^{-6})\left\{-D\nabla_r^2 \exp(-t\alpha r^{-6})\right\}. \qquad (3\text{-}6)$$

The terms in this expansion have been evaluated previously (65), and keeping the first four terms gives

$$n_s(t) = n_s(o)\exp\left\{-\beta_s t - \frac{4}{3}\pi^{3/2} n_a \alpha^{1/2} t^{1/2}\left[1 + 2.5\pi^{-1/2}\Gamma\left(\frac{5}{6}\right) D\alpha^{-1/3} t^{2/3} - 4.45\pi^{-1/2}\Gamma\left(\frac{13}{6}\right) D^2\alpha^{-2/3} t^{4/3} + 21.66 D^3\alpha^{-1} t^2 - (600/\pi)\Gamma\left(\frac{11}{6}\right) D^4\alpha^{-4/3} t^{8/4} + \ldots\right]\right\} \qquad (3\text{-}7)$$

where $n_a = N_a/V$. Yokota and Tanimoto obtained their final results by keeping these four terms in the operator expansion and by making use

of the (1,2) Pade' approximate which is obtained as follows. Upon using a finite expansion for some function F(x),

$$F(x) = a_0 + a_1 x + \ldots + a_n x^n \quad . \tag{3-8}$$

it is possible to construct the Pade' approximate to F(x) by writing it in the form

$$F(x) = \frac{b_0 + b_1 x + \ldots + b_m x^m}{c_0 + c_1 x + \ldots + c_k x^k} \quad . \tag{3-9}$$

Upon expanding Equation (3-9) in a power series, it is then possible to find the coefficients b_i and c_j from the coefficients a_n. Then, if a finite number of the a_n coefficients are known, it is likewise possible to know a finite number of the b_i and c_j coefficients. By doing this, a better approximation of the function can be determined since a finite series expansion is replaced by an infinite series expansion. This gives

$$n_s(t) = n_s(o) \exp\{-\beta_s t - \frac{4}{3}\pi^{3/2} N_a R_o^3 (\beta_s t)^{1/2} \left[\frac{1+10.87x+15.50x^2}{1+8.74x}\right]} \tag{3-10}$$

where $x = D\beta_s^{-1/3} R_o^{-2} t^{2/3}$. Note that neglecting the fifth term in Equation (3-7) is valid only if the magnitude of this fifth term is small compared to the magnitude of the fourth term, which is the same as

$$14.7 D\alpha^{-1/3} t^{2/3} < 1 \tag{3-11}$$

which can be thought of as a validity check for the Yokota-Tanimoto theory. It is possible in many cases to fit the experimental data with this theory, but Equation (3-11) will be satisfield only when the sensitizer-sensitizer interaction is small compared to the sensitizer-activator interaction.

The other limiting case involving the solution of Equation (3-3) comes from the work of Chow and Powell (6) in which they have assumed that the direct single-step interaction is a small perturbation on the diffusional transfer. Thus, Chow and Powell have taken the opposite approach to Yokota and Tanimoto, in that they have assumed that the diffusion is the more important of the two transfer processes. The Chow-Powell theory rewrites the last term of Equation (3-3) as $\nu(r)n_s(\underset{\sim}{r},t)$, and then use an approximate Fermi pseudopotential (66) in lieu of an exact dipole-dipole expression, to write

$$\nu(r) \cong \nu_o(r) + U(r) \qquad (3\text{-}12)$$

in which

$$\nu_o(r) = \begin{cases} 0 & r \geq a \\ \infty & r \leq a \end{cases}$$

$$U(r) = \begin{cases} 0 & r \leq a \\ \alpha/r^6 & r \geq a \end{cases} .$$

Equation (3-3) can now be solved, treating U(r) in the Born approximation, and this solution corresponds to the case in which energy transfer via a diffusive migration is the dominant type of transfer. Thus the solution for the energy transfer rate has the form

$$W_{CP} = W_D + W_1 \qquad (3\text{-}13)$$

where W_D is simply the rate at which excitations arrive diffusively at the surfaces of the activator traps (i.e., the rate of diffusive energy transfer to the traps) given by

$$W_D = 4\pi D a n_a [1 + a(\pi D t)^{-1/2}]. \qquad (3\text{-}14)$$

In Equation (3-14), a is the trapping radius, n_a is the number of activator sites per unit volume, and D is the diffusion coefficient. The second term in Equation (3-13) is given by the Chow-Powell theory as

$$W_1 = \frac{4\pi n_a}{3a^3} + 2\pi n_a a^2 \int_a^\infty dr \, \frac{\alpha'}{r^6} \left\{ \text{erfc} \left[\frac{r-a}{(4Dt)^{1/2}} \right] \right\}^2 \qquad (3\text{-}15)$$

$$- 8\pi n_a a \int_a^\infty dr \, \frac{\alpha'}{r^s} \left\{ \text{erfc} \left[\frac{r-a}{(4Dt)^{1/2}} \right] \right\}$$

where, as mentioned earlier, α' is the potential constant. W_1 describes the rate of energy transfer by a single step resonant interaction process plus terms describing the effects of this process on transfer by diffusion. To efficiently obtain the explicit time dependence of the energy transfer rate, it is necessary to use numerical integration. The usual method of solution is to use a least squares fit to a given set of transfer rate data and to vary α', D, and a. As mentioned earlier, the solution to Equation (3-3) assuming a sensitizer-activator interaction small compared to the sensitizer-sensitizer interaction was given by the Chow-Powell theory in Equation (3-13). This expression is shown to be valid if the direct sensitizer-activator transfer is small compared to the sensitizer diffusion. This has been shown to be true if (67,68)

$$\pi D a^4 / \alpha' > 1 \qquad \text{where } \alpha' = \beta_s R_o^6 \, . \qquad (3\text{-}16)$$

Presented here, for the case of multistep migration, are two limiting cases describing opposite types of migration processes. Numerically fitting the theories to the time dependences of the sensitizer decay data is not sufficient when determining the validity of either the

Chow-Powell or Yokota-Tanimoto theories. It is necessary to look at the criteria for the validy of each theory, given for the Yokota-Tanimoto and Chow-Powell theories by Equations (3-11) and (3-16), respectively.

Time-Resolved Site-Selection Spectroscopy

Time-resolved site-selection spectroscopy (TRSSS) measurements were used to characterize the properties of short range spectral energy transfer between the active Cr^{3+} ions in emerald. A nitrogen laser-pumped dye laser, using Oxazine 720 dye, was used to selectively excite the Cr^{3+} ions in slightly different crystal field sites so that their transitions could be spectrally resolved. Excitation in the R_2 line typically yielded three emission peaks in the R_1 line. Using the labeling scheme from Table VII, we have associated sites a and b with sensitizer sites and site d with an activator site. It was not possible to resolve site c using nanosecond pulse excitation into the R_2 line. By taking spectral scans of the fluorescence emission at different times after the laser excitation pulse, it was possible to characterize the time dependence of the energy transfer between Cr^{3+} ions in nonequivalent sites.

The experimental apparatus for the TRSSS measurements is shown previously in Figure 17. The laser emission, with linewidths maintained at $\leq$0.6 Å FWHM, was focused onto the sample which was housed in a cryogenic refrigerator in order to control the temperature. The emerald sample was excited using three different laser wavelengths, 6789.4 Å, 6792.4 Å, and 6794.5 Å, which are shown as vertical arrows in the R_2 absorption line in Figure 24. The fluorescence spectra of the R_1 lines were

then spectrally resolved through a 1 meter monochromator and directed onto an RCA-C31034 photomultiplier tube. The input and output slits were maintained at 100 μm to insure a resolution of $\leq$0.4 Å.

Figure 27 shows the typical fluorescence spectrum of the R_1 lines at 20K and at 1.00 ms after the excitation of 6789.4 Å. It was possible to resolve three separate peaks in the fluorescence spectrum, with the points in Figure 27 representing the experimental data points. To study the spectral energy transfer, it is necessary to know the area associated with each peak and how it evolves with time. To obtain a good estimate for the area, the data were deconvoluted with a curve fitting routine that fit three overlapping Gaussian peaks to the fluorescence spectra. The total line shape was approximated by using

$$g_T(w) = g_1(w) + g_2(w) + g_3(w) \tag{3-17}$$

where the individual Gaussian curves are described by

$$g_i(w) = \frac{2}{\Delta w_i} I_i \left(\frac{\ln 2}{\pi}\right)^{1/2} \exp\left[-4\ln(2)\left\{\frac{(w-w_{io})^2}{\Delta w_i^2}\right\}\right]. \tag{3-18}$$

In Equation (3-18) I_i is the peak intensity of the individual Gaussian, w_i is the FWHM of the Gaussian curve and w_{io} is the frequency of maximum intensity of the curve. Attempts were also made to fit the fluorescence spectra with an overlapping Lorentzian lineshape function, given by

$$L_T(w) = L_1(w) + L_2(w) + L_3(w) \tag{3-19}$$

where the individual Lorentzian curves are described by

$$L_i(w) = \frac{\Delta\lambda_i}{2\pi}\left[(w_{oi}-w)^2 + \frac{\Delta\lambda_i^2}{4}\right]^{-1}. \tag{3-20}$$

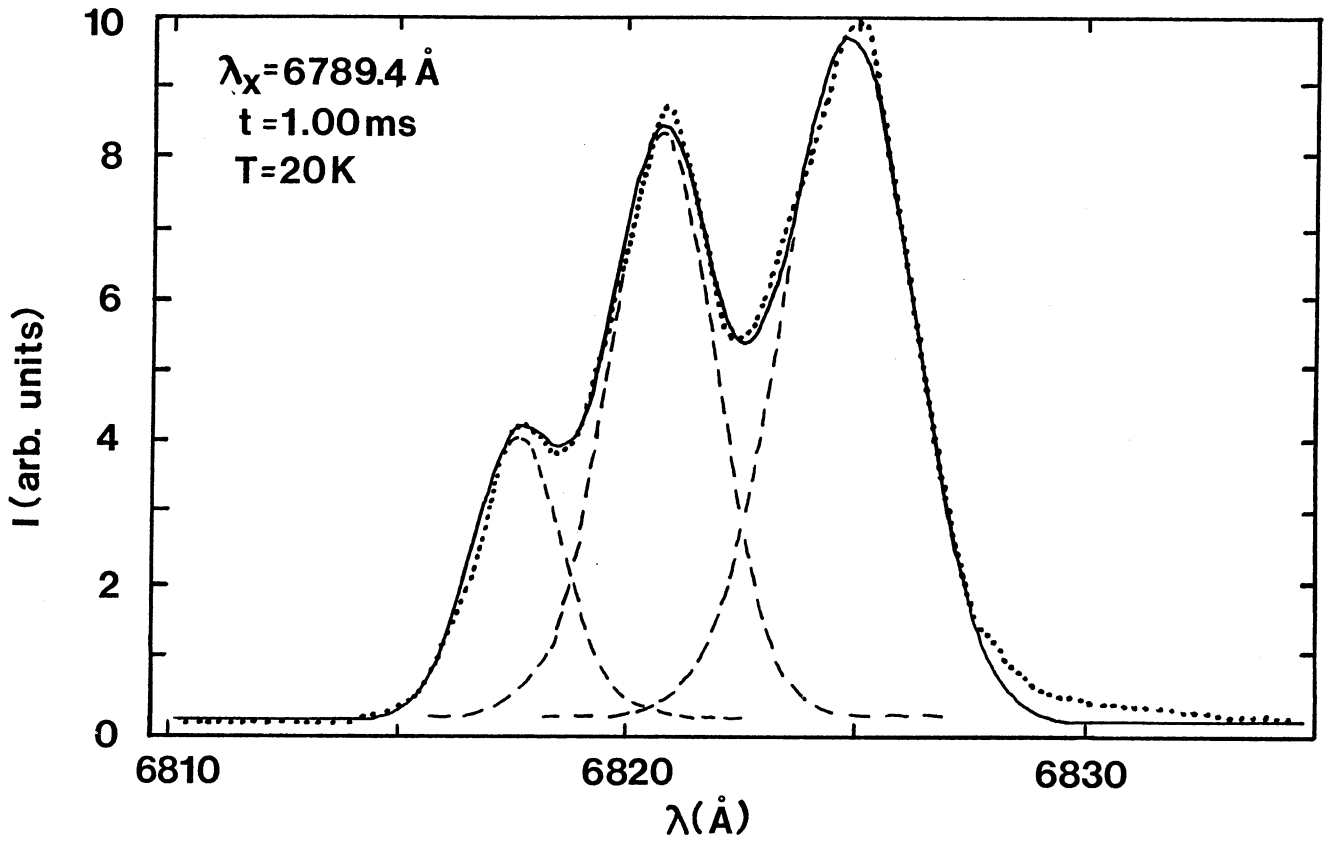

Figure 27. Fluorescence Spectra of the R_1 Lines in Emerald at 1.0 ms after the Pulse after Selectively Exciting the R_2 Line at 6789.4 Å at 20 K. The Dots Represent Experimental Data Points and the Broken and Solid Lines Represent the Separate and Overall Fitting with Three Overlapping Gaussian Curves, Respectively

In Equation (3-20), $\Delta\lambda_i$ is the FWHM of the Lorentzian line and w_{oi} is the peak frequency. When comparing the theoretical fits of the two functions to the experimental data, the Gaussian curves provided consistently better fits, with smaller overall error bars, thus all the time-resolved fluorescence spectra were fit with the overlapping Gaussian function. The separate Gaussians are denoted by the broken lines in Figure 27, with the overall fit shown by the solid line. The Gaussian profile fits the data quite well, with a little discrepency typically only on the low energy wings. From the curve fitting routine it was possible to obtain the total area of each peak, the peak wavelength and intensity, and the full-width at half maximum for each Gaussian. For the energy transfer analysis, it is necessary to observe the time evolution of the ratios of sensitizer to activator areas, thus, for these calculations, the areas are taken to be simply the product of the Δw_i and I_i. Any proportionality constants are then taken care of in the calculation of the ratios. In order to completely characterize the spectral energy transfer in emerald, the fluorescence spectra was monitored for the three different pumping wavelengths, each at four different temperatures and at eleven different times after the pulse. Thus, this portion of the TRSSS consists of 132 different fluorescence spectra. To avoid numerous figures and tabulations, only an assortment of representative data will be included in this section, such as the use of Figure 27 to demonstrate the typical fit of the overlapping Gaussians for one spectrum.

The fluorescence risetimes and lifetimes of each of the three peaks were monitored for each excitation wavelength and temperature and these

measured values are listed in Table XI. The two highest energy peaks are both double exponential decays with fast risetimes, while the lowest energy peak is single exponential over two decades with a much longer risetime. The accuracy of the lifetimes and risetimes is approximately ±5%. To characterize the properties of energy transfer between ions in different types of sites we have chosen to designate the two highest energy peaks, denoted as sites a and b in Table VII, as being associated with sensitizer sites and the lowest energy peak, denoted as site d in Table VII, as being associated with an activator site. Figures 28-30 show the fluorescence spectra of the R_1-lines for four different temperatures at 100 μs after the three different excitation wavelengths. As the excitation wavelength is shifted to lower energy, it is seen that the number of distinct peaks reduces until there is only one fluorescence peak remaining, that being associated with the emission from the activator site excited by the lowest energy excitation wavelength. There is also slight back transfer from activator to sensitizer sites, noticeable mostly at higher temperatures, and this will become important when evaluating the different energy transfer models. Figures 31-33 show the fluorescence spectra at 20 K, for the three excitation wavelengths, at five different times after the pulse. The two highest energy peaks seem to evolve at approximately the same rate, while the third peak evolves more slowly and becomes the dominant peak at the longer times after the pulse. This all correlates well with the fluorescence lifetime and risetime data presented in Table XI.

This time evolution of the R_1-lines is demonstrated in Figure 34, which shows the changes in the ratios of the integrated fluorescence

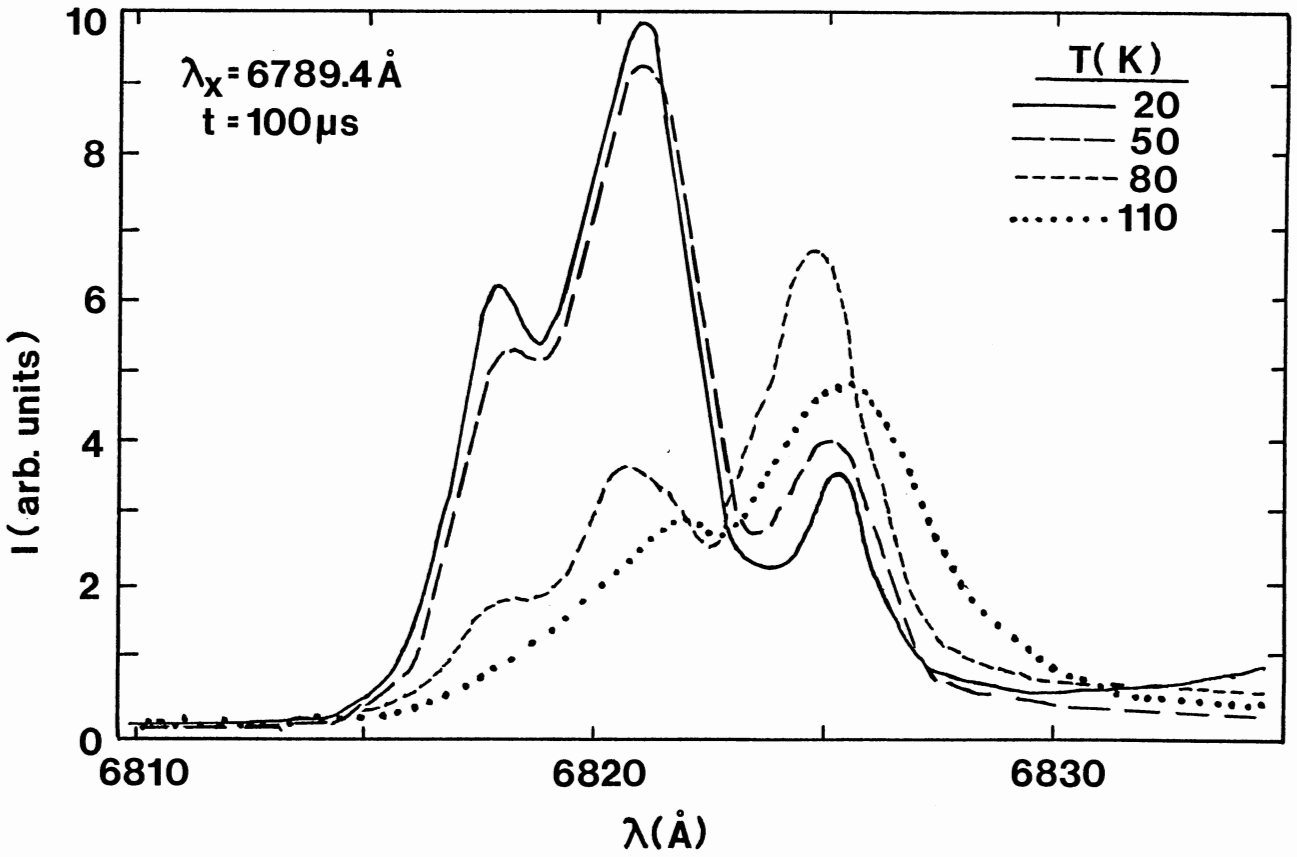

Figure 28. Fluorescence Spectra of the R_1-Lines in Emerald for Four Different Temperatures at 100 μs after the Pulse, Following Selective Excitation of the R_2-Lines at 6789.4 Å

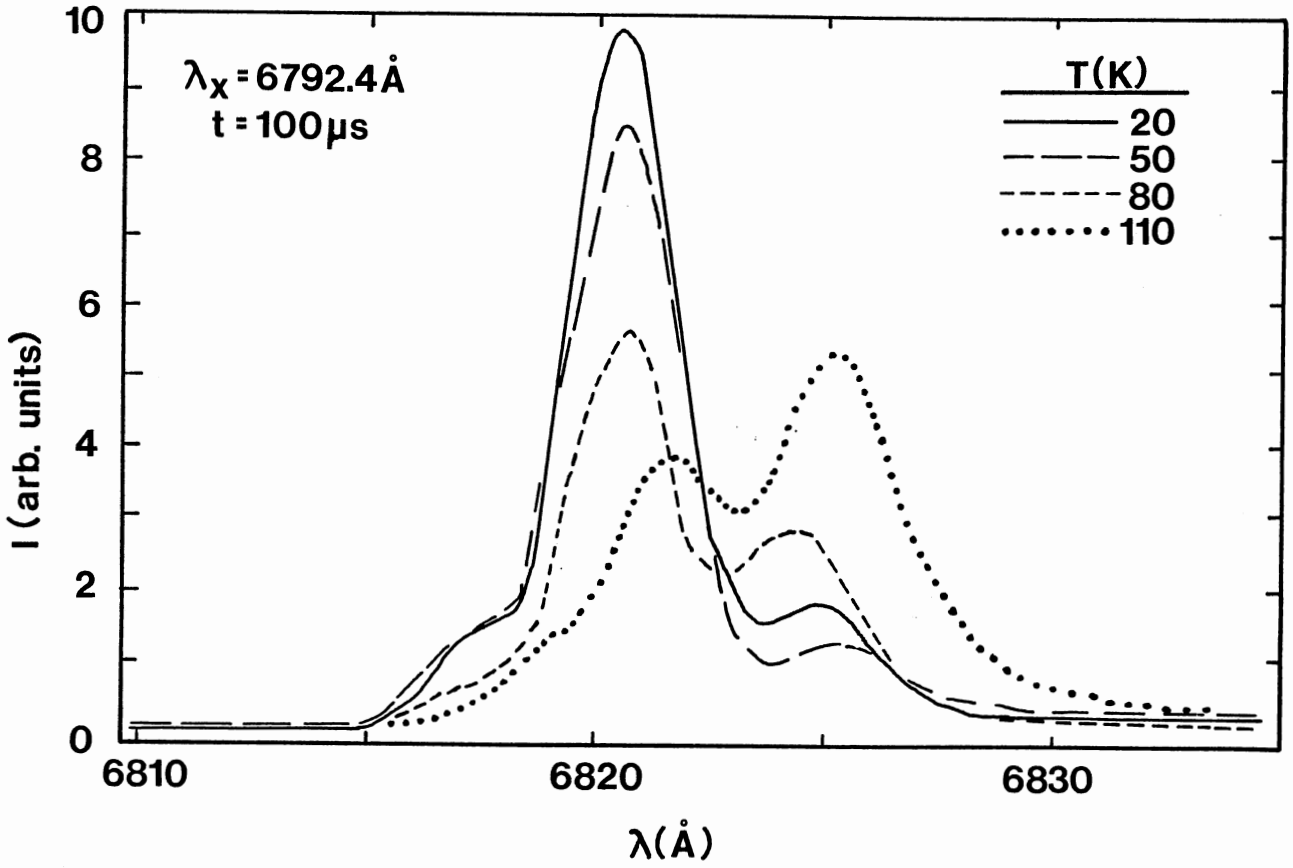

Figure 29. Fluorescence Spectra of the R_1-Lines in Emerald for Four Different Temperatures at 100 μs after the Pulse, Following Selective Excitation of the R_2-Lines at 6792.4 Å

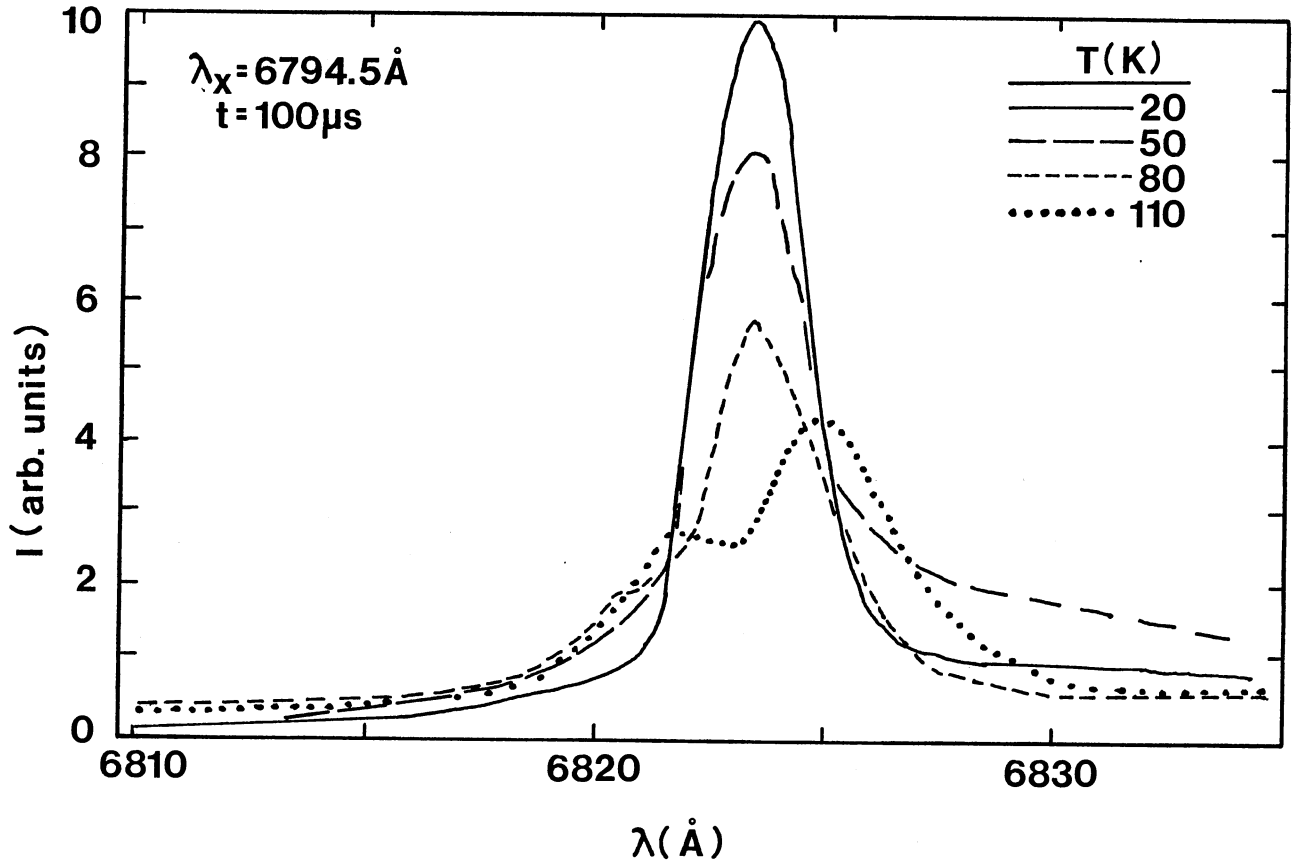

Figure 30. Fluorescence Spectra of the R_1-Lines in Emerald for Four Different Temperatures at 100 μs after the Pulse, Following Selective Exicitation of the R_2-Lines at 6794.5 Å

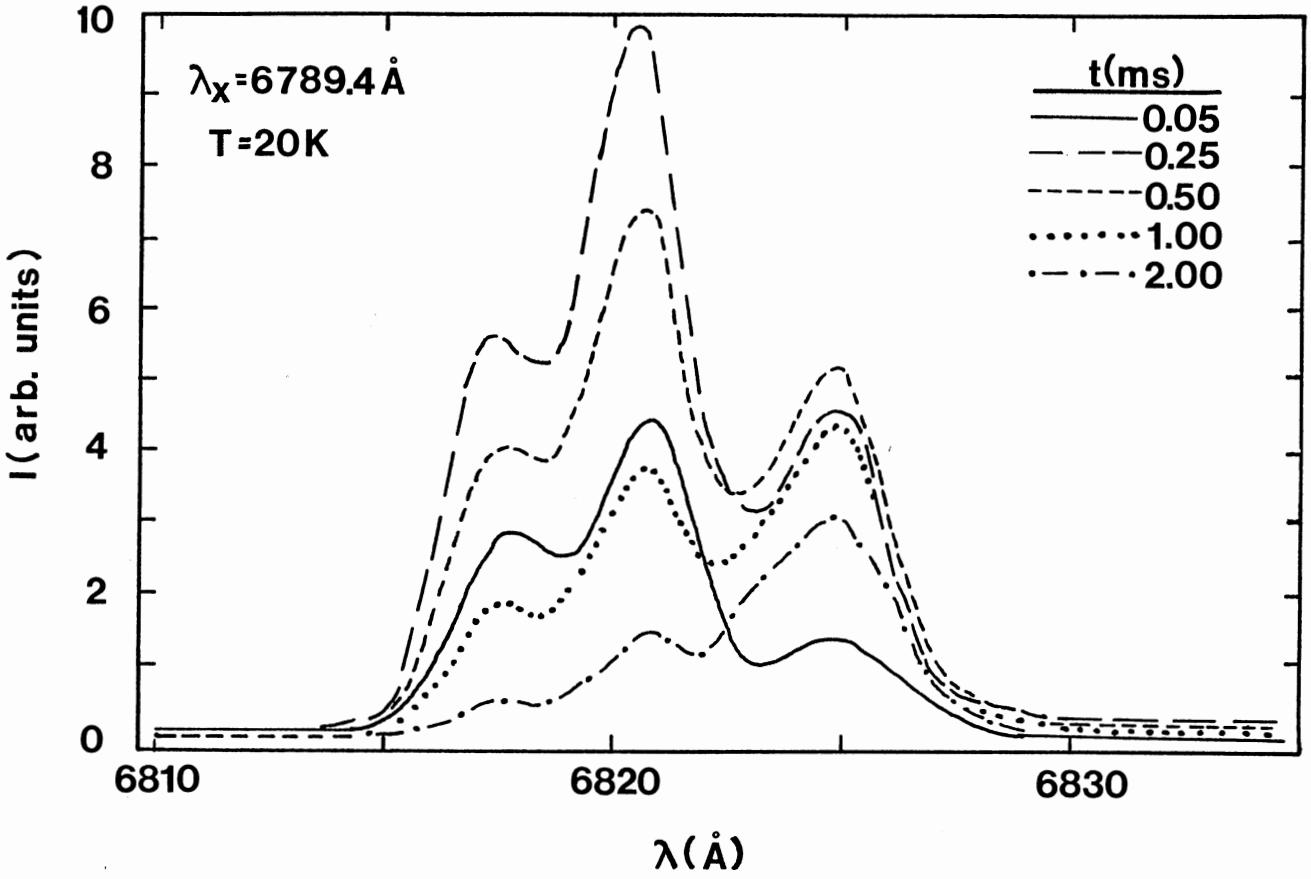

Figure 31. Fluorescence Spectra of the R_1-Lines in Emerald for T=20 K at Five Different Times after the Pulse, Following Selective Excitation of the R_2-Lines at 6789.4 Å

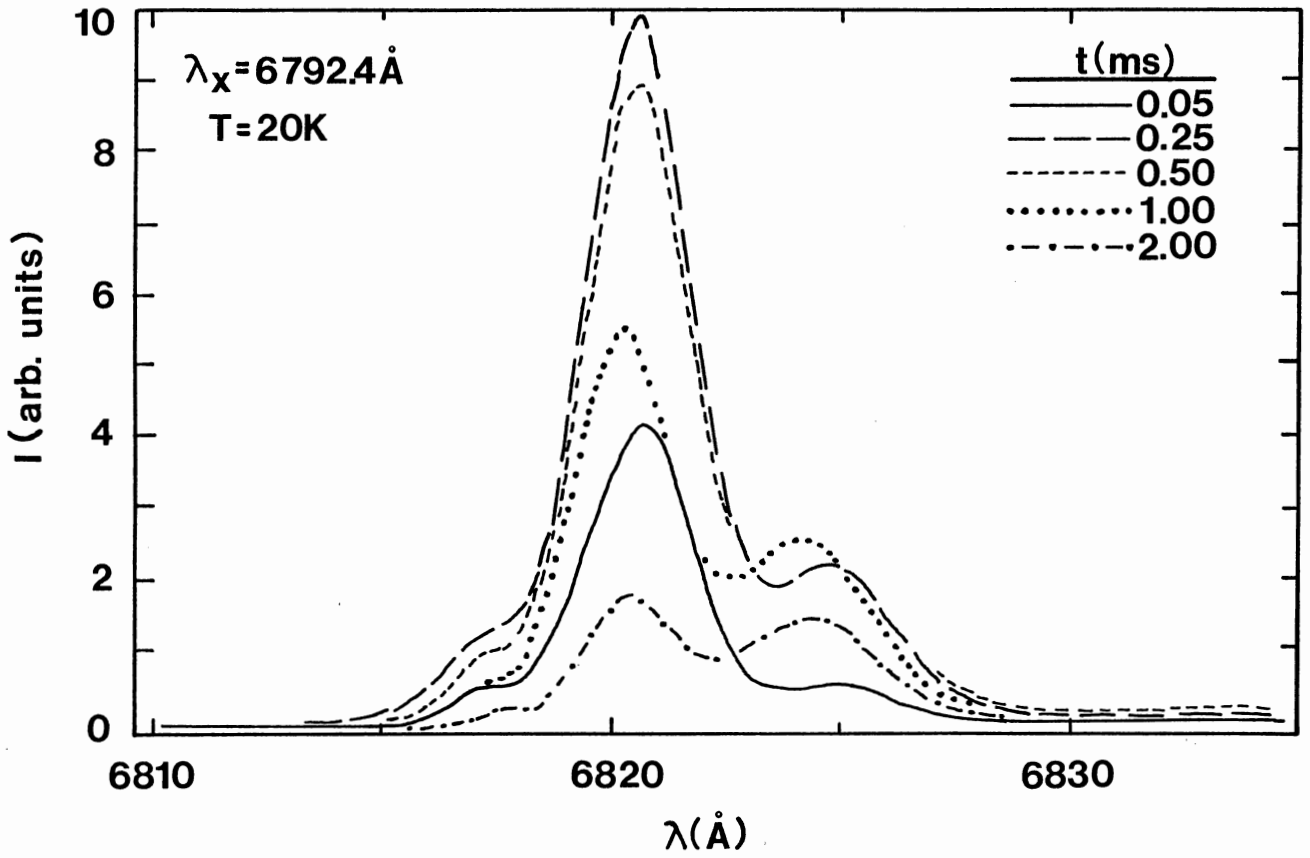

Figure 32. Fluorescence Spectra of the R_1-Lines in Emerald for T=20 K at Five Different Times after the Pulse, Following Selective Excitation of the R_2-Lines at 6792.4 Å

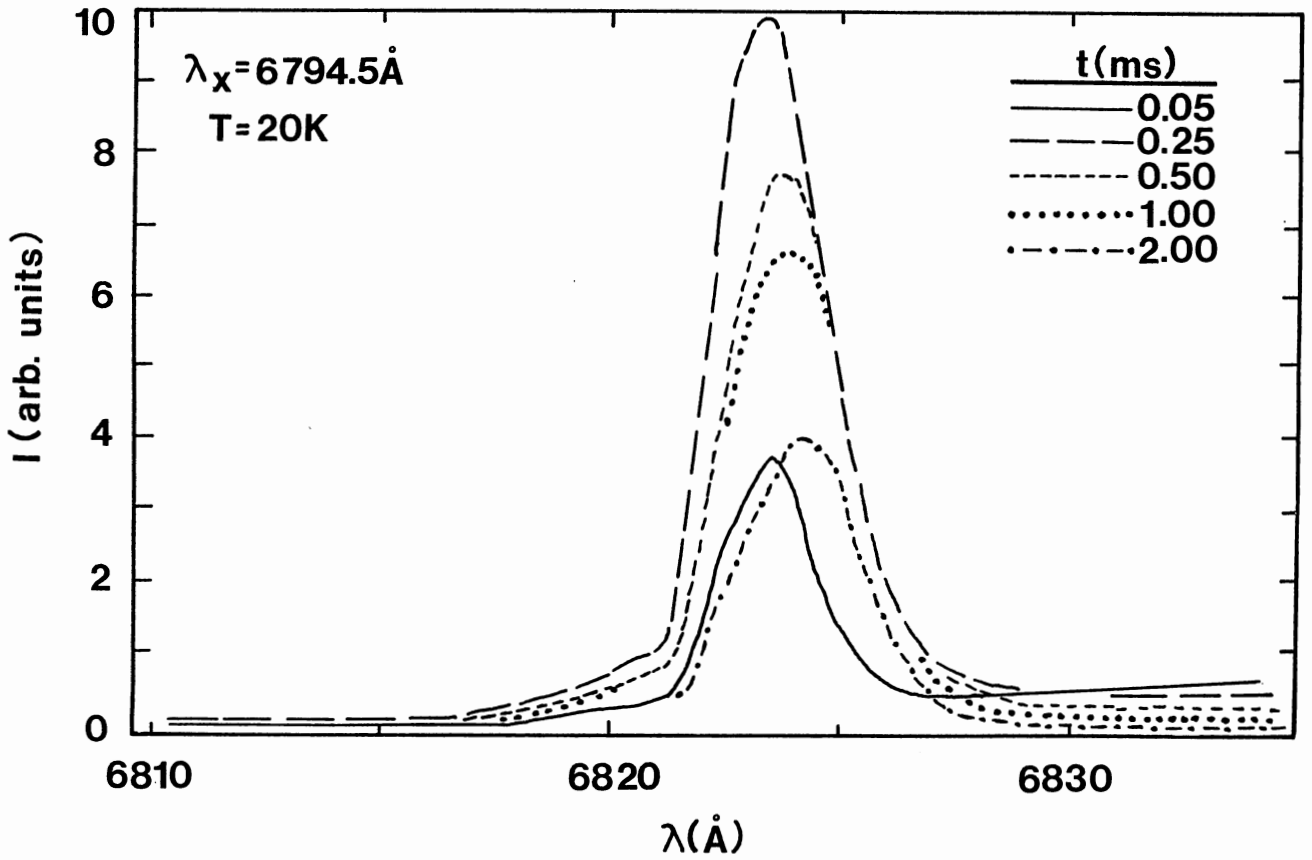

Figure 33. Fluorescence Spectra of the R_1-Lines in Emerald for T=20 K at Five Different Times after the Pulse, Following Selective Excitation of the R_2-Lines at 6794.5 Å

TABLE XI

FLUORESCENCE LIFETIMES, τ_i, AND RISETIMES, t_R, OF SENSITIZER AND ACTIVATOR SITES FOR EACH EXCITATION WAVELENGTH AND TEMPERATURE

	$\lambda_{emission}$ (Å):	6817.5		6820.75			6825.0	
	λ_{ex} (Å):	6789.4	6792.4	6792.4	6794.5	6789.4	6792.4	6794.5
T=20 K	τ_1 (ms)	1.112	1.859	1.079	1.540	1.436	1.610	1.575
	τ_2 (ms)	0.317	0.707	0.351				
	t_R (μs)	83.89	95.86	112.0	149.8	218.7	213.2	364.2
T=50 K	τ_1 (ms)	1.023	1.435	1.117	1.490	1.263	1.710	1.445
	τ_2 (ms)	0.324	0.404	0.400				
	t_R (μs)	62.34	95.83	106.6	143.2	207.9	234.8	353.4
T=80 K	τ_1 (ms)	1.043	1.083	1.004	1.078	1.034	1.380	1.189
	τ_2 (ms)	0.337	0.282	0.306				
	t_R (μs)	29.85	90.44	101.2	112.0	200.9	170.1	234.8
T=110 K	τ_1 (ms)	1.186	0.603	0.613	0.574	0.555	0.614	0.596
	τ_2 (ms)	0.215	0.113	0.233				
	t_R (μs)	--	49.50	31.17	82.38	148.6	62.34	133.6

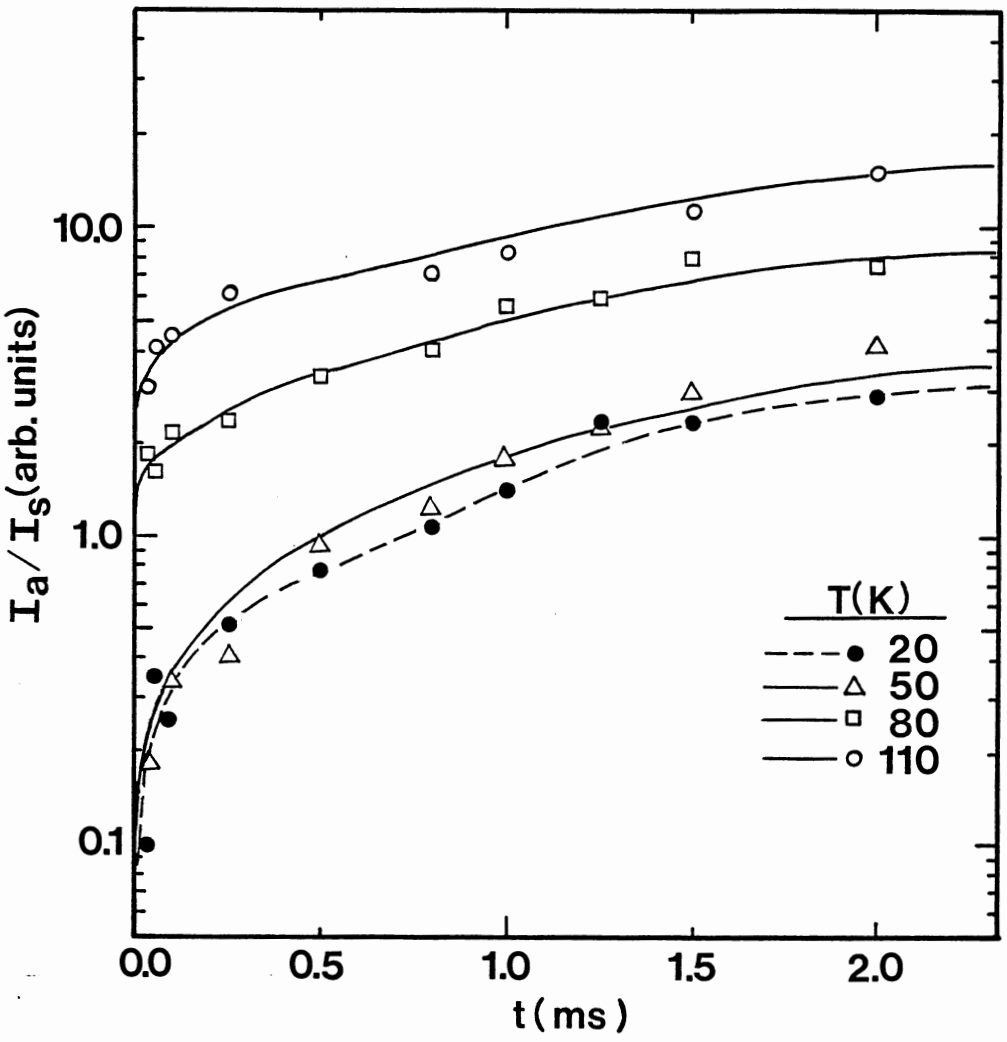

Figure 34. Time Dependence of the Ratios of the Integrated Fluorescence Intensities from Cr^{3+} Sensitizer and Activator Sites for Four Different Temperatures. The Solid Line Represents the Theoretical Fit Using a Rate Equation Model

intensities of the activator sites to that of the sensitizer sites. The values of the integrated fluorescence intensities are listed in Table XII. These areas are taken from the fits of the experimental data with Gaussian curves. There is an initial build up of the relative area of the transition and, at longer times after the pulse, an equilibrium condition is approached. The time evolution in the ratios can be modeled using a phenomenological rate parameter model illustrated in Figure 35. The sensitizer ions are those in the site preferentially excited by the laser at a rate W_s, whereas the activators are ions in sites which receive the energy through energy transfer as well as a small amount of direct pumping at a rate W_a. n_a and n_s are the concentrations of the ions in the excited states, W_{sa} is the rate of energy transfer from sensitizer to activator, and β_a and β_s are the fluorescence decay rates, associated with each type of site. The rate equations describing the time evolution of the populations of the excited state are

$$\frac{dn_s}{dt} = W_s - \beta_s n_s - W_{sa} n_s \tag{3-21}$$

$$\frac{dn_a}{dt} = W_a - \beta_s n_a + W_{sa} n_s \quad . \tag{3-22}$$

These equations can be solved assuming a delta-function excitation pulse, negligible back-transfer, and an explicit time dependence for the energy transfer rate. A variety of different theoretical models were tested, but it was found that the best fits to the data at both low and high temperatures were obtained with an energy transfer rate which varies as $t^{-1/2}$. The solutions of Equations (3-21) and (3-22) are given by

$$n_s(t) = n_s(0)\exp[-\beta_s t - 2\tilde{\Omega}t^{1/2}] \tag{3-23}$$

TABLE XII

TIME EVOLUTION OF THE INTEGRATED AREAS OF THE ACTIVATOR AND SENSITIZER FLUORESCENCE VERSUS TEMPERATURES

		Time After Pulse (ms)										
T(K)		0.025	0.05	0.10	0.25	0.50	0.80	1.00	1.25	1.50	2.00	5.00
						$\lambda_x = 6789.5$ Å						
20	I_a/I_s:	0.099	0.35	0.25	0.51	0.76	1.04	1.36	2.36	2.26	2.84	6.74
50		0.182	0.24	0.31	0.40	0.89	1.18	1.89	2.12	2.94	4.44	4.66
80		1.849	1.63	2.22	2.30	3.29	3.88	5.70	5.89	8.01	7.30	10.36
110		3.083	4.12	4.46	6.16	--	6.91	--	7.80	11.07	20.21	--

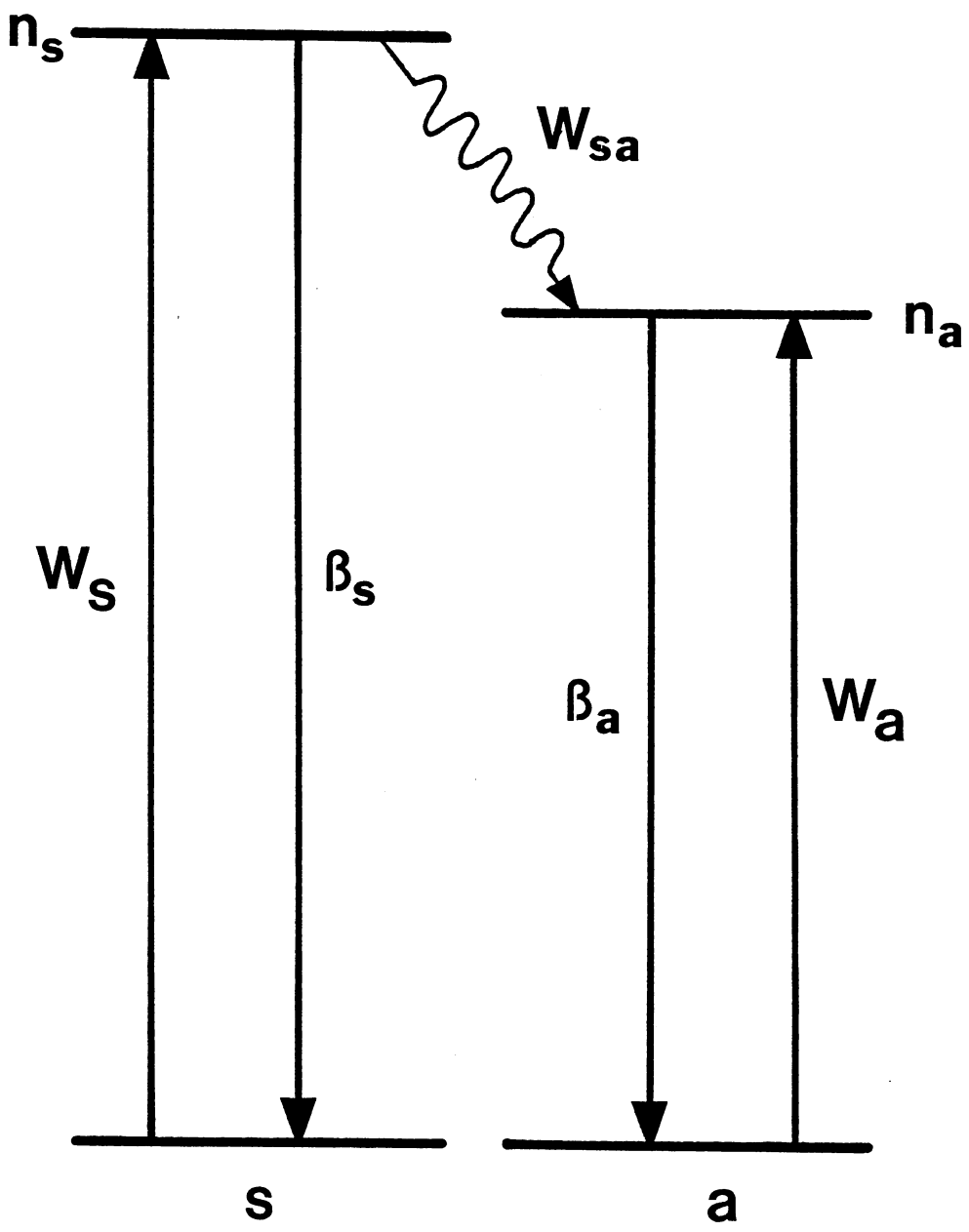

Figure 35. Rate Parameter Model for Interpretation of Spectral Energy Transfer Data

$$n_a(t) = n_s(0)\{\exp[-\beta_s t]-\exp[-\beta_s t-2\tilde{\Omega}t^{1/2}]\}+n_a(0)\exp[-\beta_a t] \tag{3-24}$$

where the time dependence of the energy transfer rate is written explicitly as $W_{sa}=\tilde{\Omega}t^{-1/2}$. The ratio of the integrated fluorescence intensities is proportional to the rate of the excited state populations and can be written directly as

$$\frac{I_a(t)}{I_s(t)} = \left(\frac{\beta_a^r}{\beta_s^r}\right)\left[\left\{\left(\frac{I_a(0)/h\nu_a}{I_s(0)/h\nu_s}\right)\left(\frac{\beta_s^r}{\beta_a^r}\right)+1\right\}\exp[2\tilde{\Omega}t^{1/2}]-1\right], \tag{3-25}$$

where β_a^r and β_s^r are the radiative decay rates associated with the activator and sensitizer sites, respectively. The solid and broken lines in Figure 34 represent the best fits of Equation (3-25) to the experimental data, treating $I_a(0)/I_s(0)$ and $\tilde{\Omega}$ as adjustable parameters. The values for these parameters are listed in Table XIII. This $t^{-1/2}$ variation of the energy transfer rate can be attributed to several types of processes: a trap-modulated energy migration in three dimensions in which the energy migrates among several sensitizer ions before transferring to an activator ion; single-step electric dipole-dipole interaction between randomly distributed sensitizers and activators; and multistep energy migration on a one dimensional lattice. It is possible to rule out the possibility of migration on a one dimensional lattice, and comparing the results with another analysis method should give an indication as which of the remaining two possibilities is the valid model.

Another approach used to extrapolate the energy transfer data is to look at the change in the fluorescence intensity as a function of time. This decay can be fit with an expression for the time evolution of the fluorescence with the energy transfer rate expressed by an appropriate

TABLE XIII

ADJUSTABLE PARAMETERS USED IN FITTING OF SPECTRAL ENERGY TRANSFER RATE EQUATION MODEL

T(K)	$I_a(0)/I_s(0)$	$\tilde{\Omega}(s^{-1/2})$	R_o (Å)
	$\lambda_x = 6789.5$ Å		
20	0.085	15.590	7.42
50	0.099	16.868	7.51
80	1.250	15.586	7.34
110	2.630	16.463	7.63

energy transfer theory. Analysis of the data was attempted using several models, mainly the Yokota and Tanimoto and the Chow-Powell theories described in the previous section, and it was found that the best analytical model for describing the transfer kinetics in emerald is that of Chow and Powell (6). Rewriting Equations (3-14) and (3-15) for the energy transfer rate gives

$$W'_{sa} = 4\pi N_a D_r a\left[1+a(\pi D_n t)^{-1/2}+\frac{4\pi N_a \alpha'}{3a^3}\right] + 2\pi N_a a^2 \int_a^\infty dr \left(\frac{\alpha'}{r^6}\right)\left\{\text{erfc}\left[\frac{(r-a)}{(4D_n t)^{1/2}}\right]\right\}^2 - 8\pi N_a a \int_a^\infty dr \left(\frac{\alpha'}{r^5}\right)\left\{\text{erfc}\left[\frac{(r-a)}{(4D_n t)^{1/2}}\right]\right\}$$

where N_a is the total concentration of activators, given as 1.716 x 10^{20} cm^{-3} from the absorption data in Table VIII, and D_n is the nonresonant diffusion coefficient. Once again, it needs to be stressed that the TRSSS measures spectral transfer among the nonresonant Cr^{3+} ions in emerald. Figure 36 shows the typical results of fitting this equation from the Chow-Powell theory to one of the experimental decay curves, taken at 20K, and demonstrates excellent agreement. As was detailed in the previous section, a good fit of the theory to the data is possible with both the Yokota-Tanimoto and Chow-Powell theories, but the appropriate theory has to meet the criteria listed in Equations (3-11) or (3-16), respectively. For 20 K, the values obtained from the fitting procedure using the Yokota-Tanimoto theory gave

$$D_n = 1.52\text{x}10^{-12}\,cm^2/s \quad \text{and} \quad \alpha' = 2.44\text{x}10^{-41}\,cm^6/s \ .$$

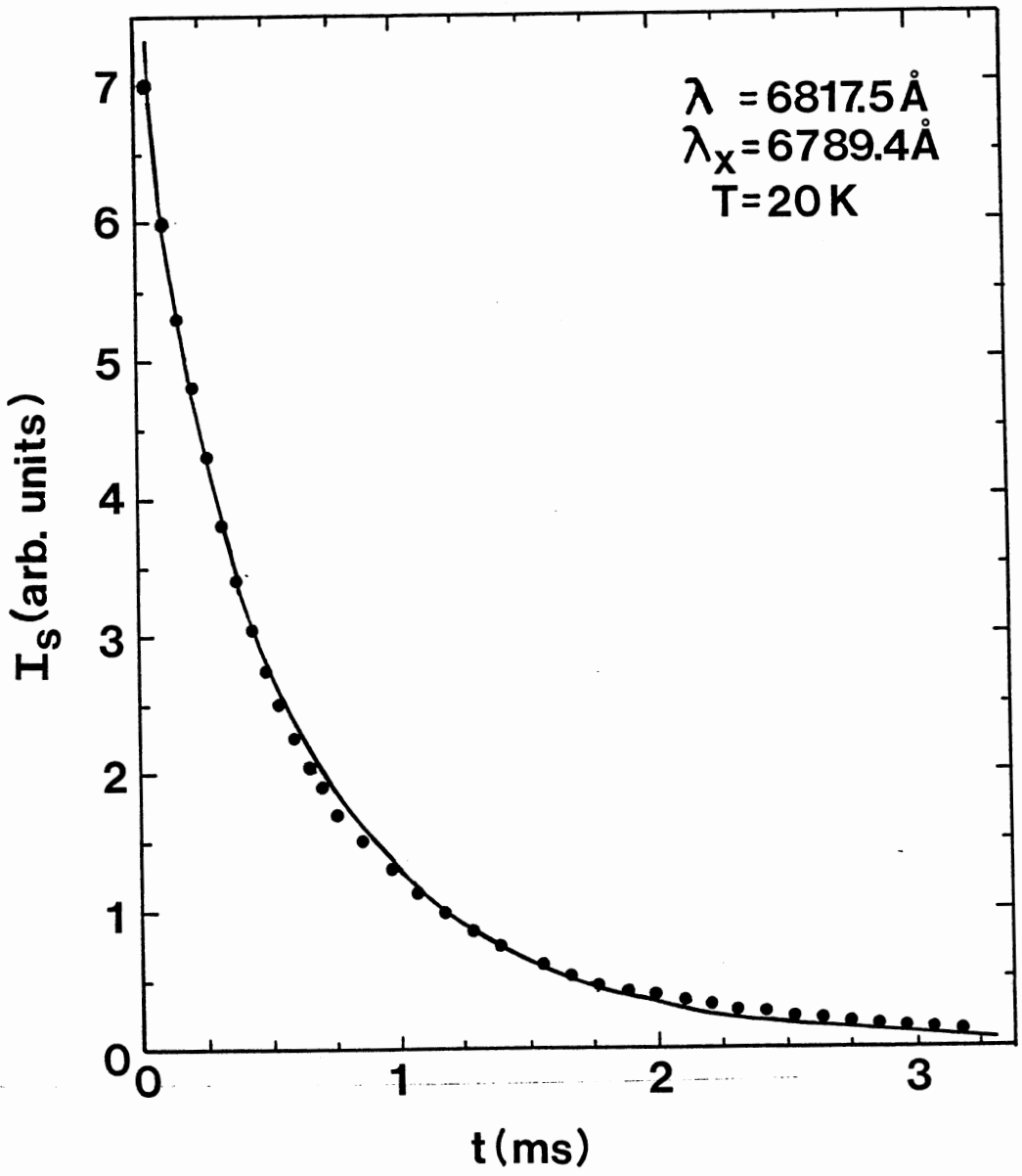

Figure 36. Time Dependence of the Fluorescence Emission Intensity of One Sensitizer Site of Cr^{3+} in Emerald at 20 K. The Solid Line Represents the Theoretical Fitting Using the Chow-Powell Model for Energy Transfer

When these values of D_n and α are substituted into (3-11) along with a typical time, such as the long component of the double exponential lifetime, the validity parameter is given as $14.7 D_n \alpha^{-1/3} t^{2/3} = 8.27$, which is greater than unity. Equation (3-11) can likewise be solved to show that the time necessary to meet the criteria is t = 46 μs, which is approximately the separation of the first and second data points in Figure 36. Although the Yokota-Tanimoto theory gives a good fit to this system, the Yokota-Tanimoto model is not valid for emerald.

However, fitting this data with the Chow-Powell theory gives, for T = 20 K,

$$D_n = 6.51 \times 10^{-13} \text{ cm}^2/\text{s} \text{ and } \alpha' = 4.66 \times 10^{-41} \text{ cm}^6/\text{s}$$

and a = 15.0 Å. As is shown in Figure 36, there is excellent agreement between experiment and theory. These parameters may then be substituted in Equation (3-16) to obtain the validity parameter

$$\pi D_n a^4 / \alpha' = 22.12$$

which is significantly greater than one. Thus the criteria are met and we can assume that this model accurately describes the spectral energy transfer in emerald. As defined by the Chow-Powell theory, $\alpha' = \beta_s^o R_o^6$, and from the values obtained by fitting the theory to the data, it is possible to explicitly solve for the critical interaction distance, R_o. For T = 20 K, the calculated value of this distance is R_o = 6.11 Å. It would be possible to know the intrinsic decay rate of this emission if we had a series of samples with low concentrations, but since we did not, this

decay rate has been estimated with the longer component of the fluorescence lifetime. This limits the accuracy of the R_o values to $\pm$ 0.4 Å. The values of the parameters, obtained in the computer fits, for different temperatures are listed in Table XIV.

Using the analysis of the data described above, the values of D_n were determined at several temperatures and the results are shown in Figure 37. From studies of the decay kinetics associated with the emission from the two sensitizer sites, D_n appears to remain constant for temperatures less than 100 K.

As has been shown, there are two possible methods for evaluating the spectral energy transfer in emerald. One involves modeling the pumping, decay and transfer kinetics with a rate parameter model. The other makes use of a physically appropriate theory to model the sensitizer decay kinetics, and for emerald, the most appropriate theory was that of Chow and Powell (6). In order to compare these two, it is necessary to first compare the resulting parameters for each. The values of the critical interaction distance, R_o, were calculated for both methods of evaluation. For T = 20 K, we found R_o = 6.11 Å from the fit to the sensitizer decay curve with the Chow-Powell model. It is also possible to use the Förster-Dexter (56,57) expression for an electric dipole-dipole transfer rate to find the value of R_o using the rate equation model. This expression is given by

$$R_o = \left\{ \frac{\omega_{DD}}{N_a} (\tau_s^o)^{1/2} \left(\frac{4}{3} \pi^{3/2} \right)^{-1} \right\}^{1/3} \qquad (3\text{-}26)$$

where

$$\omega_{DD} = W_{sa} = \tilde{\Omega} t^{-1/2} \quad .$$

TABLE XIV

SPECTRAL ENERGY TRANSFER PARAMETERS FROM
CHOW-POWELL THEORY FOR
EMERALD EMISSION

T(K)	D_n (10^{-13} cm^2/s)	α (10^{-41} cm^6/s)	a (Å)	R_o (Å)	CP Criterium
		λ = 6817.5 Å			
20	6.509	4.67	15.98	6.11	28.6
50	5.718	3.84	21.28	5.83	95.9
80	4.640	6.63	28.74	6.40	15.0
110	0.157	1.72	36.17	5.23	49.1
		λ = 6820.75 Å			
20	2.818	4.81	9.6	6.10	15.6
50	2.975	2.68	16.88	5.58	28.3
80	2.772	3.59	33.92	5.85	32.1
110	0.318	1.44	24.13	6.68	23.5

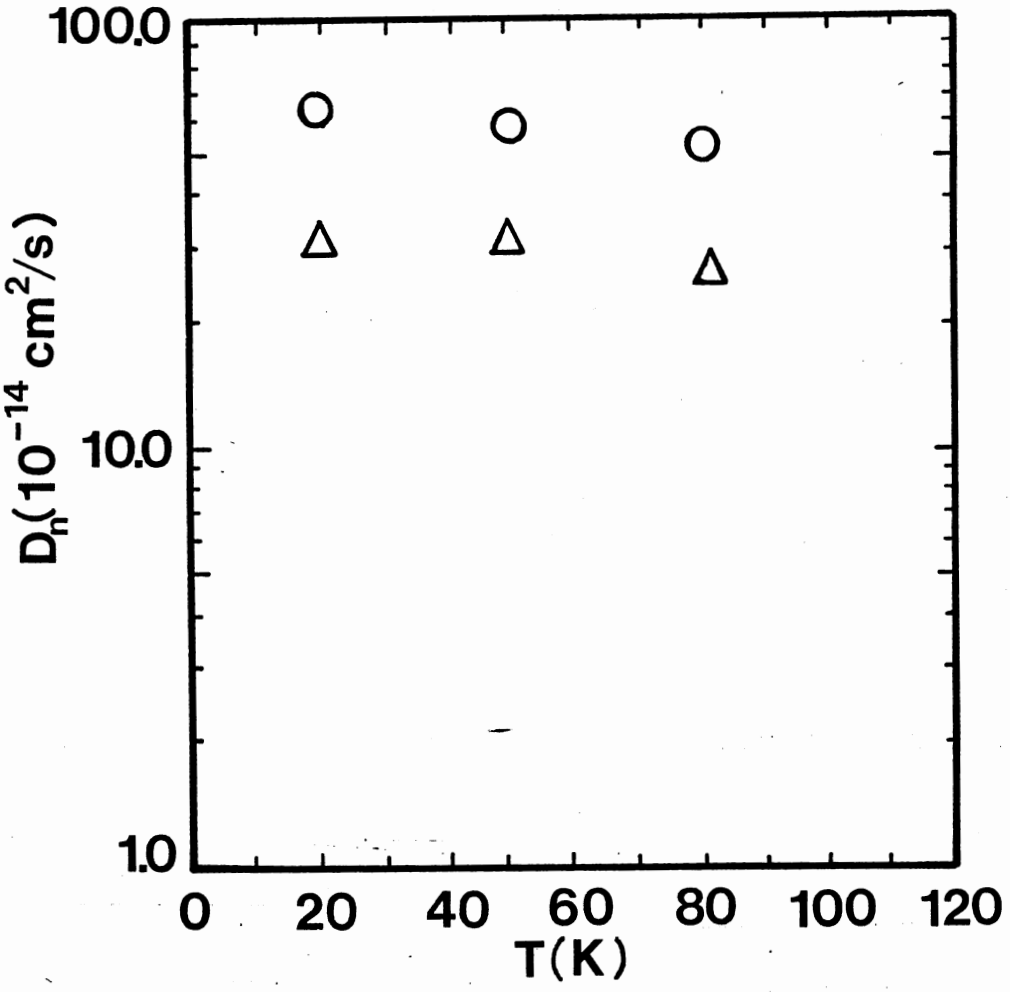

Figure 37. Temperature Dependence of the Nonresonant Diffusion Coefficient, D_n, Obtained from Site-Selection Spectroscopy Data for λ=6817.5 Å, (O); λ=6820.75 Å (Δ)

For T = 20 K, the value of R_o from the rate equation model is found to be R_o = 7.42 Å, and is listed in Table XIII. This value is in relatively good agreement with the value predicted by the Chow-Powell theory. It is also possible to compare the calculated values of the energy transfer rates for each method of evaluation. From the fitting using the Chow-Powell model, using a typical time of interest of 1.50 ms, $W'_{sa} = 6.47 \times 10^2\ s^{-1}$ at T = 20 K and for the rate equation model $W_{sa} = 4.03 \times 10^2\ s^{-1}$ for the same typical time and temperature. This again shows good agreement between the two models that monitor two different experimentally measurable optical characteristics. Since the Chow-Powell theory assumes a trap-modulated energy migration in three dimensions among sensitizers before transfer to an activator, and since both models give very similar transfer rates and critical interaction distances, it can be concluded that this is also the model to be used for interpreting the results of the rate equation evaluation.

Four-Wave Mixing Results

Four-wave mixing (FWM) measurements were used to characterize the properties of long range spatial energy migration in emerald. The details of the experimental setup used in this work were presented in Figure 18. Crossed laser beams from a ring dye laser were tuned to 588 nm, so as to pump reasonantly the $^4T_2$ band, and were used to establish a population grating of excited Cr^{3+} ions in the sample. The total laser power used in this work was about 300 mW. A He-Ne laser was used as the probe beam and the signal beam was processed by a PAR/EG&G signal averager. The two stronger beams from the ring dye laser interfere

inside the mixing medium creating a standing wave of the electric field with a wave vector parallel to the counterpropagating components of the wave vector of the pump beam. As a result of the absorption of the pump beams by the $^4T_2$ level, a population of excitons is created inside the mixing medium. The profile of the exciton concentration will follow the pattern of the interference of the pump beams. Thus, if the interference of the pump beam forms a sinusoidal pattern, then the profile of the exciton concentration will likewise be sinusoidal. If the absorption spectrum of the excited states differs from the absorption spectrum of the ground state, the imaginary part of the index of refraction in the zones of high excitation concentration is not equal to the imaginary part of the index of refraction in the zones associated with ions in the ground state. As a result of this, a transient grating of excited states is generated. This grating is referred to as a population grating for emerald since a nonuniform distribution of Cr^{3+} ions is established in the ground and excited states by resonantly pumping the $^4T_2$ level. By chopping the write beams on and off, the kinetics of the laser-induced grating could be monitored. These are influenced by the fluorescence decay and the spatial migration of Cr^{3+} excitation energy from the peak to valley regions of the gratings. If the chopper cuts off the excitation source, the grating will begin to decay as a result of the finite excitation lifetime and the energy migration process, and the initial nonuniform exciton distribution will then begin to fade out. If the grating is generated once again, and then the probe beam is switched on, the population grating will scatter it and as was shown in Figure 19, this scattered beam can be monitored to study the grating decay dynamics.

Our major interest in this work is the study of the kinetics of the laser-induced grating and the energy transfer processes that take place. The measurement of FWM scattering efficiency as a function of the crossing angle of the write beams, θ, is a secondary study that provides useful information concerning the nature of the laser-induced change in the complex index of refraction. For a simple sine wave grating, an equation describing the scattering efficiency at the Bragg angle was originally derived by Kogelnik (70) and Eichler (71) in their early work on holographic gratings, and is given by

$$\eta = \exp(-2\alpha L)\{\sin^2[d\pi\Delta n/2\lambda]+\sinh^2[d\Delta\alpha/4]\} \qquad (3\text{-}27)$$

where α and L are the absorption coefficient and thickness of the sample, and d is the thickness of the grating. Making the assumption that there is little or no beam depletion, and that the product of the grating thickness and the modulation depth is small, it is possible to simplify Equation (3-27) so that the FWM scattering efficiency is given by

$$\eta \approx \left(\frac{\pi}{2\lambda}\right)^2[d^2\Delta n^2] + \left(\frac{1}{4}\right)^2[d^2\Delta\alpha^2] \quad . \qquad (3\text{-}28)$$

As derived by Suchocki et al. in reference 72, it is possible to explain theoretically the variation of the signal intensity with crossing angle using a model based on the interaction between the laser and a two level system. This work starts with the wave equation describing the propogation of the laser beams in the atomic system as

$$\nabla^2\vec{E} = \left(\frac{\mu}{c^2}\right)\frac{\alpha^2\vec{E}}{\alpha t^2} + \left(\frac{4\mu\pi}{c^2}\right)\frac{\partial^2\vec{P}}{\partial t^2} \quad . \qquad (3\text{-}29)$$

Then, describing the electric fields of the laser beams as plane waves

$$\vec{E}_i(\vec{r},t) = \left(\frac{\vec{A}_i}{2}\right) \exp[-i(\omega_i t - \vec{k}_i \cdot \vec{r})] + c.c. \qquad (3\text{-}30)$$

where i=1→4, and correlates to the fields depicted in Figure 19, $\vec{P}$ is the polarization which is defined in terms of the complex susceptibility, and the $\vec{A}_i$'s represent the amplitudes of the beams. This method of solution gives a scattering efficiency defined as $\eta=|A_4|^2/|A_3|^2$, thus there are now two complex, coupled partial differential equations. They (72) then separate out the real and imaginary parts to give four, real, coupled equations that have to be solved numerically. The theoretical fits to the results provide information concerning the relative importance of the absorption and dispersion contributions to the signal, and the dephasing time of the atomic system. The values of the peak-to-valley differences in the absorption coefficients, $\Delta\alpha$, and the refractive index, Δn, are obtained from the adjustable parameters used in the theoretical fit of the scattering efficiency data versus the write beam angle. The important region of interest when fitting the theory to the experimental data has been shown to be at the peak of the scattering efficiency (72). The values of the fitting parameters found for the scattering efficiency versus crossing angle are listed in Table XV. The values in the crossing angle have been corrected for the refractive index of emerald, which is taken to be n=1.58 at 588 nm.

A typical computer fit of the scattering efficiency versus angle, for emerald at 45 K, is shown in Figure 38. The quality of the computer fits for the case of emerald is not quite as good as previous fits (72), and this is probably connected with the nonuniform distribution of the chromium ions in the sample and the vibrations inherent in the

TABLE XV

RESULTS OF THE FOUR-WAVE MIXING SCATTERING EFFICIENCY MEASUREMENTS IN EMERALD AT T=45 K

Parameter	Value
Adjustable Coefficients; D_i^j:	
D_2^r (10^{-6}):	2.0
D_2^i (10^{-9}):	8.0
D_1^r (10^{-7}):	5.0
D_1^i (10^{-7}):	4.0
Peak to Valley Changes in the Absorption Coefficient; $\Delta\alpha$ (cm^{-1}):	0.22
Peak to Valley Changes in the Refractive Index; Δn (10^{-4}):	1.3
Dephasing Time; T_2 (10^{-12} s):	1.2
Absolute Scattering Efficiency for θ=5.3 deg (10^{-3}):	3.7
Power of Write Beams; I_0 (W/cm^2):	80.0
Wavelength of Write Beams; λ (10^{-7} m):	5.764
Photon Energy; $h\nu$ (10^{-19} J):	3.45
Ground State Absorption Cross-Section; σ_1 (10^{-20} cm^2):	3.15
Excited State Absorption Cross-Section; σ_2 (10^{-20} cm^2):	2.79*

*Taken from Reference (79)

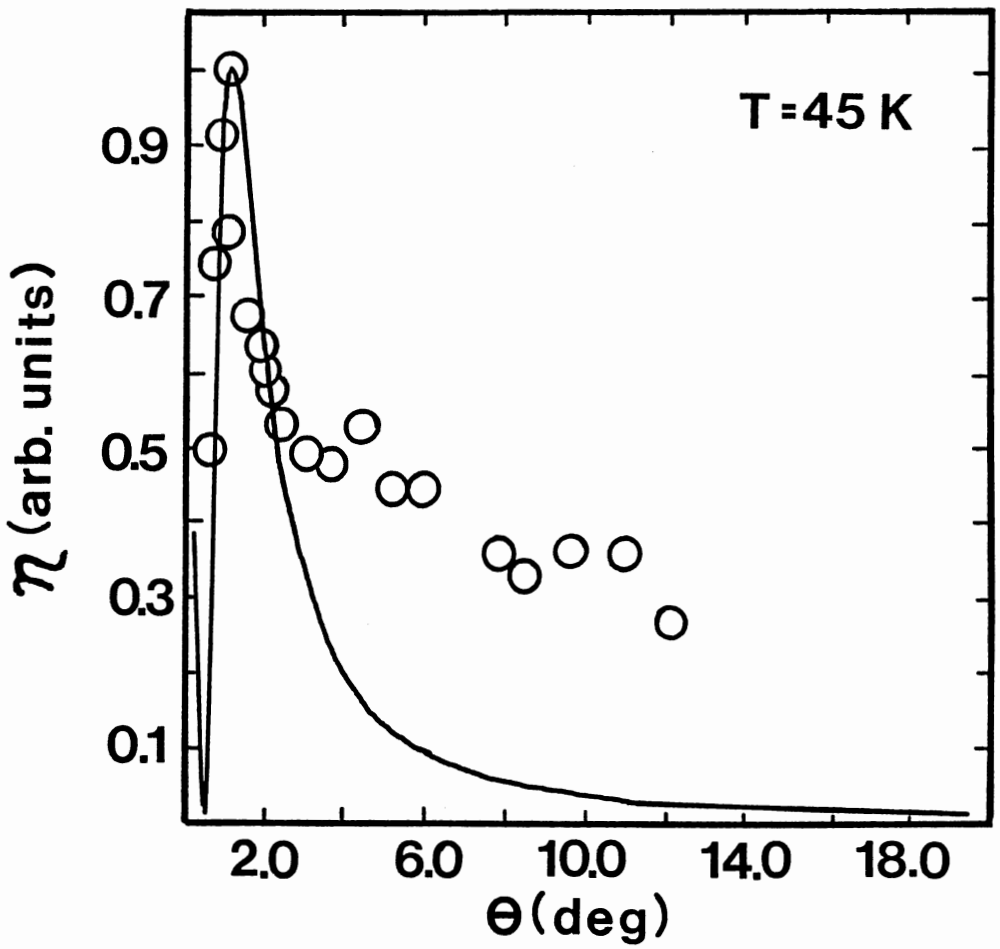

Figure 38. FWM Scattering Efficiency Versus the Write-Beam Crossing Angle at 45 K for Cr^{3+} Ions in Emerald. (See Text for Explanation of Theoretical Lines)

experimental setup. These vibrations can destroy the holographic grating which is created in the crystal. The FWM signal is much more sensitive to vibrations at small crossing angles than for larger angles, and it is for that reason that the data for small angles have much bigger error bars. Also, a background from the scattered He-Ne laser light is stronger for the small angles. All the above mentioned reasons might cause the measured relative intensity of the scattering efficiency at small angles to be less than true values, however they should have little influence in the position of the peak of the signal, and, as has been stated before, the fits to the peak region of the signal are quite good.

The values of $\Delta\alpha$, Δn, and T_2 were calculated from the formulas:

$$\Delta\alpha = \frac{-2\alpha D_2^i}{D_1^i} \tag{3-31}$$

$$\Delta n = \left(\frac{\alpha C}{\omega}\right) \frac{D_2^r}{D_1^i} \tag{3-32}$$

$$T_2 = \left(\frac{2\omega}{C}\right)\left(\frac{\Delta n}{\Delta\alpha}\right) (\omega-\omega_{21})^{-1} \tag{3-33}$$

where α is the absorption coefficient for the write beam wavelength (α = 5.57 cm^{-1} at 588 nm), c is the speed of light, ω is the circular frequency of the write beam light, ω_{21} is the resonant frequency of the atomic transitions, and the D_i^j's are theoretical coefficients treated as adjustable parameters in the numerical solutions of the coupled equations.

It is also possible to estimate the value of $\Delta\alpha$ from the rate equation analysis of a two level system (72,74):

$$\Delta\alpha = N_0 I_0 \sigma_1 (\sigma_1 - \sigma_2) \ (2I_0\sigma_1 + h\nu/\tau)^{-1} \qquad (3-34)$$

where N_0 is the concentration of active ions, I_0 is the intensity of the write beams with photon energy $h\nu$, τ is the fluorescence lifetime, and σ_1 and σ_2 are the ground and excited state absorption cross sections, respectively. Using the values listed in Table VIII and Table XVI, one can use Equation (3-34) to obtain the value of $\Delta\alpha$ equal to 0.07 cm^{-1}. Taking into account the uncertainty of the values σ_2 and I_0, these results are in quite reasonable agreement.

Relatively large values of Δn imply that the population grating created inside the crystal is mainly due to a dispersion grating. It should also be pointed out that the relatively large absorption coefficient of our emerald sample might be the cause of some errors due to beam depletion which has not been taken into account in this theory.

The FWM signal kinetics were found to be nonexponential and dependent on the crossing angle of the write beams for all temperatures for which a signal was visible. Above 160 K no FWM signal was observed and this can be attributed to the small value of the fluorescence lifetime at these temperatures (75). The decay of a transient population grating can usually be described by one of two types of decays; a simple exponential or a nonexponential expression. As stated earlier, the grating can decay because of two processes, one being the normal fluorescence decay and the other being energy migration from the peak-to-valley regions of the grating. Assuming a decay is purely exponential, it could be described by the expression (76,77)

$$I_s(t) = I_s(0)\exp(-Kt) \qquad (3-35)$$

where K, the grating decay rate involves the two contributions to the decay process, namely fluorescence and migration, and can be written in terms of macroscopic parameters

$$K = \frac{2}{\tau} + \left(\frac{32\pi^2 D}{\lambda^2}\right) \sin^2\left(\frac{\Theta}{2}\right) \tag{3-36}$$

or in terms of microscopic parameters

$$K = 2\left\{\left[\left(\frac{\bar{\alpha}+1}{\tau}\right)^2 + \left(\frac{4\pi V}{\Lambda}\right)^2\right]^{1/2} - \bar{\alpha}\right\} \tag{3-37}$$

Here, V is the ion-ion interaction rate, τ is the fluorescence lifetime, D is the diffusion coefficient, Θ is the crossing angle of the write beams in air, expressed in degrees, λ is the wavelength of the write beams in air, $\bar{\alpha}$ is the exciton scattering rate, and Λ is the grating spacing, defined by $\Lambda=\{\lambda/[2\sin(\Theta/2)]\}$. This single exponential grating decay is indicative of an incoherent, or random hopping type of exciton migration.

However, as was mentioned above, the signal kinetics in emerald were found to be nonexponential, and thus are consistent with the predictions of the theory of Kenkre (8) which describes the decay of a laser-induced grating in the presence of partially coherent exciton migration. The time dependence of the normalized FWM signal is given by

$$I_s(t) = \exp(-2t/\tau)\{J_o(bt)\exp(-\bar{\alpha}t) + \bar{\alpha}\int_o^\infty du \cdot \exp(-\bar{\alpha}[t-u])J_o(b[t^2-u^2]^{1/2})\}^2 \tag{3-38}$$

where b is expressed as

$$b = \frac{\pi^2 anV\theta}{45\lambda} \tag{3-39}$$

and n is the index of refraction of the crystal. a, which is the average distance between active chromium ions in our sample, can be estimated to be (78)

$$a = \left(\frac{0.17}{N_o}\right)^{1/3} = 9.87\text{Å} . \tag{3-40}$$

The FWM signal decay kinetics were fit using Equation (3-38) treating $\bar{\alpha}$ and b as adjustable parameters. In order to emphasize the effects of energy migration, both the experimental data and the theoretical expression were divided by $\exp(-2t/\tau)$ which eliminates the fluorescence decay contribution to the signal kinetics. A typical theoretical fit to the data is shown in Figure 39 for a crossing angle of $\theta=20^{o}$ at T=16 K, and the nonexponential shape of the curve is consistent with the presence of long mean-free path exciton migration. The Kenkre theory gives an excellent fit to the data. The parameters used to characterize the dynamics of the exciton migration include the resonant diffusion coefficient

$$D_r = \frac{2V^2a^2}{\bar{\alpha}} \tag{3-41}$$

the mean free path

$$L_m = \frac{1.414Va}{\bar{\alpha}} \tag{3-42}$$

the diffusion length

$$L_D = (2D_r\tau)^{1/2}, \tag{3-43}$$

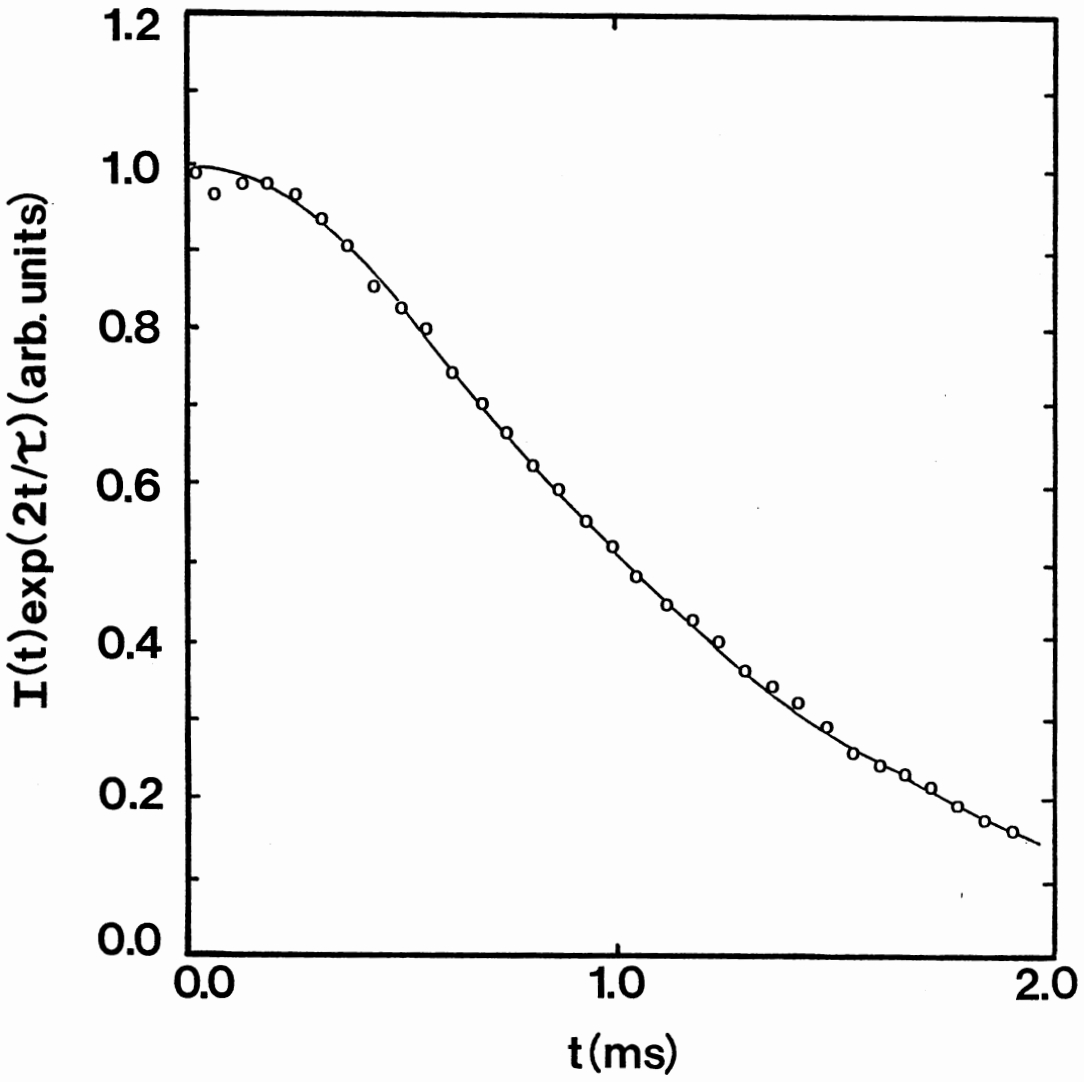

Figure 39. Four-Wave Mixing Decay Kinetics (Points) and Theoretical Fit of Equation (3-38) (Line) After Dividing by the Fluorescence Decay Factor. T=16°K and the Crossing Angle of the Write Beams is θ=20°

and the number of sites visited between scattering events,

$$N_s = \frac{L_m}{a} \quad . \tag{3-44}$$

The values of $\bar{\alpha}$, V, D_r, L_m, L_D, and N_s were calculated for each temperature and these values are listed in Table XVI. Figure 40a shows the temperature dependence of the scattering rate, $\bar{\alpha}$. This increase in $\bar{\alpha}$, with temperature, can be attributed to the scattering of excitons by phonons. The theoretical treatment of exciton-phonon scattering has been developed by Agranovich and co-workers for the case of Frenkel excitons in organic molecular crystals (80). Although our work deals with mobile electronic excitation energy localized on a single ion, this can be treated as a Frenkel exciton in a disordered system, and the theoretical treatment of Agranovich can be applied as an approximation to our data. This theory assumes that the exciton-phonon interaction can be considered a weak interaction, thus it is possible to develop an expression for the scattering rate from perturbation and scattering theory. The scattering rate for excitons by phonons is given by (80)

$$\frac{1}{\tau} = -\sum_{\vec{q},\vec{r}} \frac{\Delta^{\vec{k}}_{z}(\vec{q})}{k_z} \left[W^{\vec{k}}_{a}(\vec{q},\vec{r}) + W^{\vec{k}}_{e}(\vec{q},\vec{r}) \right] \tag{3-45}$$

where

$$W^{\vec{k}}_{e}(\vec{q},\vec{s}) = \frac{2\pi}{N\hbar} \left| F(\vec{k}-\vec{q};\vec{k};\vec{q},\vec{s}) \right|^2 (\bar{N}_{\vec{q},\vec{s}}+1)\, \delta \left[E(\vec{k}) - E(\vec{k}-\vec{q}) - \hbar\omega_{\vec{s}}(\vec{q}) \right] \tag{3-46}$$

and

$$W^{\vec{k}}_{a}(\vec{q},\vec{s}) = \frac{2\pi}{N\hbar} \left| F(\vec{k}+\vec{q};\vec{k};\vec{q},\vec{s}) \right|^2 \bar{N}_{\vec{q},\vec{s}}\, \delta \left[E(\vec{k}) - E(\vec{k}+\vec{q}) + \hbar\omega_{s}(\vec{q}) \right]. \tag{3-47}$$

TABLE XVI

THE TEMPERATURE DEPENDENCE OF AVERAGED SPATIAL ENERGY TRANSFER PARAMETERS FOR EMERALD FROM FWM MEASUREMENTS

T(K)	$D_r(10^{-7}\ cm^2/s)$	$L_m(10^{-6}\ cm)$	$L_D(10^{-5}\ cm)$	N_s	$\bar{\alpha}(10^3\ s^{-1})$	$V(10^5\ s^{-1})$
11	2.79	10.47	3.06	106	2.55	1.91
15	3.78	12.52	3.56	127	2.41	2.16
30	6.88	8.75	4.83	89	8.55	5.38
40	5.04	6.39	4.24	65	12.34	5.65
50	7.77	7.90	5.26	80	12.45	7.05
70	14.08	8.39	6.02	85	16.32	10.36
100	24.13	11.46	5.64	116	17.48	11.67
130	40.26	13.40	5.25	136	26.37	17.80
160	81.70	16.97	5.15	173	43.10	24.57

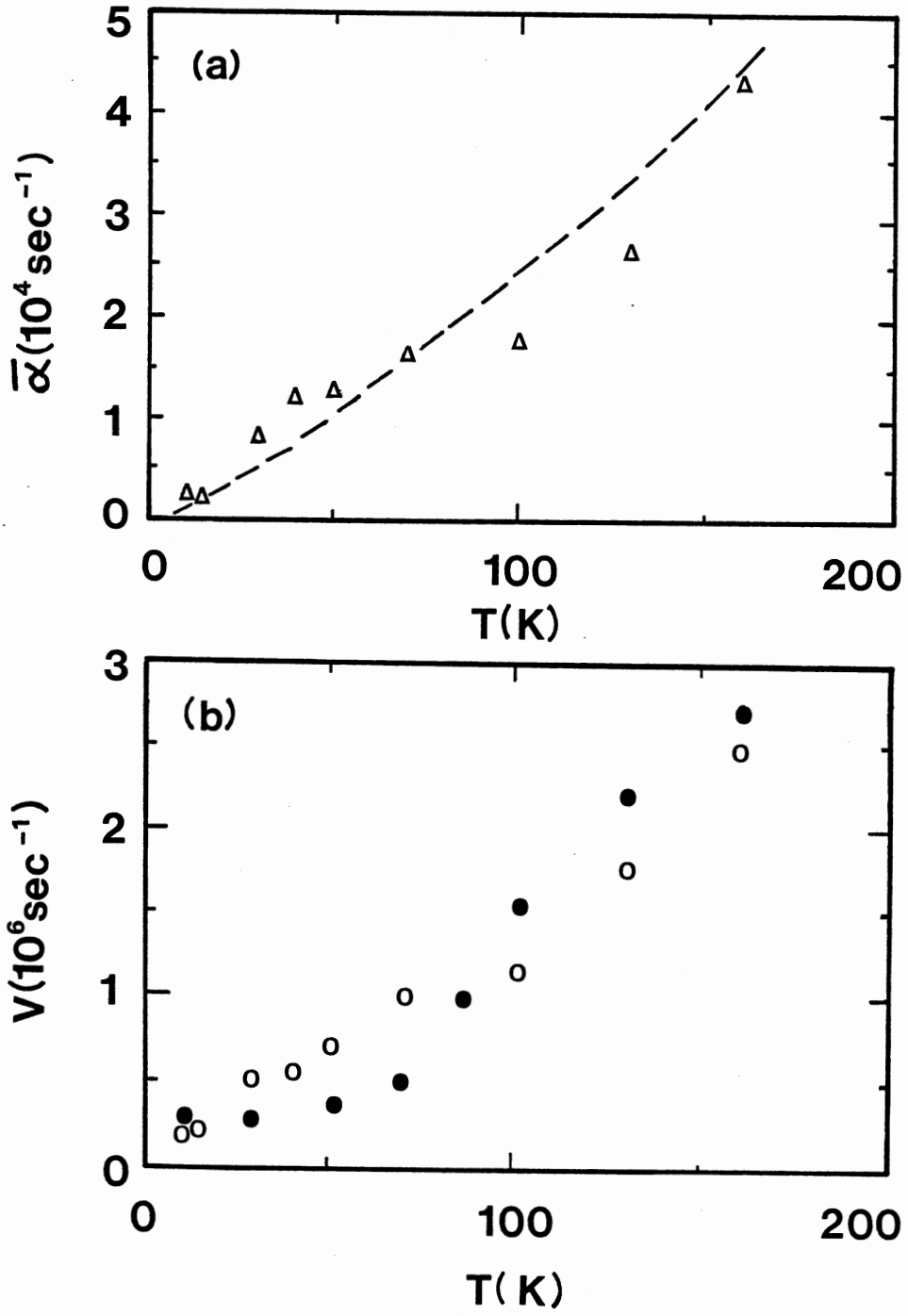

Figure 40. Temperature Dependence of (a) the Ion-Ion Interaction Rate V(O) with the Predicted Value of V(●) from the Förster-Dexter Theory, and (b) the Exciton Scattering Rate $\bar{\alpha}$ with a Broken Line Showing a $T^{3/2}$ Dependence, due to Acoustic Phonon Scattering

In Equations (3-44-46) $\vec{k}$ is the exciton wave vector before the collision, $\Delta\vec{k}(\vec{q})$ is the variation in the exciton wave vector due to the collision with the phonon $\vec{q},\vec{r}$, $W_a^{\vec{k}}(\vec{q},\vec{r})$ is the probability of absorption of the phonon $\vec{q},\vec{r}$, and $W_e^{\vec{k}}(\vec{q},\vec{r})$ is the probability of emission of the phonon $\vec{q},\vec{r}$, with $\bar{N}_{q,s}^{\rightarrow\rightarrow} = [\exp(h\omega_s^{\rightarrow}(\vec{q})/kT) - 1]^{-1}$. The number of the phonon branch is $\vec{r}$. The scattering rate can also be thought of as being made up of scattering due to both optical and acoustic phonons

$$\frac{1}{\tau} = \frac{1}{\tau_{op}} + \frac{1}{\tau_{ac}} \quad . \tag{3-48}$$

The exciton is not always going to be centered at the minimum of the exciton band, and its position may be denoted by $\vec{k} = \vec{k}_o + \vec{\kappa}$. If the minimum of the exciton band is located at the center of the Brillouin zone, then by Agranovich's definition (80), $\vec{k}_o = 0$ and $\vec{k} = \vec{\kappa}$. The thermal average value of $\vec{\kappa}$ may be evaluated from the relation

$$\frac{\hbar^{2\rightarrow 2}\kappa}{2m^*} = \frac{3}{2} k_B T \tag{3-49}$$

for a given temperature, with m* defined as the effective mass of the exciton.

The expression for the relaxation time due to scattering by acoustic phonons is given by Agranovich (80) as

$$\frac{1}{\tau_{ac}} = \frac{3|f_o^{ac}|^2 \bar{a}^4 m^*}{4\pi g \hbar^{3\rightarrow 2\rightarrow}\kappa} \left(\frac{k_B T}{\hbar\nu_o}\right) \int_o^{\S} x^4 \coth x dx \tag{3-50}$$

where $\S = 2\vec{\kappa}\hbar\nu_o/(k_B T)$, $\bar{a}$ is the latice parameter, f_o^{ac} is a constant associated with the coupling in the exciton-phonon interaction, and ν_o is the velocity of sound. Using Equation (3-49), and assuming $\S<1$, sets

the criteria that

$$T > \frac{12m^*\nu_o^2}{k_B} \simeq 4\ K\ \frac{m^*}{m} \tag{3-51}$$

then the integrand in (3-51) may be replaced by its value at small x. This reduction leaves

$$\frac{1}{\tau_{ac}} = \frac{gTK^3}{k^2} \sim T^{3/2} \tag{3-52}$$

where g contains all constants from (3-50). For the FWM studies in emerald, we are primarily concerned with this scattering due to acoustic phonons. The Debye temperature of emerald (45) is approximately 570 K, thus scattering due to optical phonons is of little concern in the temperature range of our FWM studies. From (3-50), the scattering due to acoustic phonons should go as $T^{3/2}$ and the broken line in Figure 40a shows a $T^{3/2}$ behavior. This seems to approximate roughly the change in $\bar{\alpha}$ with temperature and thus we claim that this increase in $\bar{\alpha}$ is due to scattering of the excitons by acoustic phonons.

The open circles in Figure 40b depict the change in the values of the ion-ion interaction rate, V, with temperatures from the FWM analysis. There is an obvious increase in the value of V with temperature. This increase is attributed to the temperature dependent change in the R-line versus vibronic side band emission. As the temperature increases, the emission from the R-lines decreases and the total area associated with the broad-band emission increases. From the theory of Förster (56) and Dexter (57) it is possible to approximate the temperature dependence of the ion-ion interaction rate in terms of a product of the intrinsic decay rate and a ratio of the critical interaction distance, R_o, and

and the sensitizer-activator separation, R, to the sixth power as

$$V(T) = (\tau_s^o)^{-1} \left(\frac{R_o}{R}\right)^6 \quad . \tag{3-53}$$

This theory does assume that the interaction is electric dipole-dipole. The temperature dependence of R_o in Equation (3-53) is contained solely in the overlap integral term, as R_o is given by

$$R_o = \left\{ \frac{3c^4h^4}{4\pi K^2 n^4} \left(\frac{\varepsilon}{\varepsilon_c}\right)^4 \Omega(T) \right\}^{1/6} \quad . \tag{3-54}$$

There is also the explicit temperature dependence of the intrinsic sensitizer lifetime. The overlap for this case involves the broad band vibronic emission and the sharp line R-line emission. To monitor how the overlap integral evolves with temperature, we measured the integrated fluorescence area for the R-lines and the vibronic side bands. We have approximated the temperature dependence of the overlap integral with the change in the ratio of the integrated areas with temperature. The interaction rate can now be rewritten in terms of the intrinsic sensitizer lifetime and the ratio of the broad-band vibronic to R-line emission integrated areas

$$V(T) = C(\tau_s^o)^{-1} \frac{I_{vib}}{I_R} \quad . \tag{3-55}$$

In Equation (3-56), C is a proportionality constant and the subscripts vib and R denote the vibronic side band and ^2E, R-line emission, respectively. The values of the integrated areas are taken from the time-resolved spectra under cw excitation at 457.9 nm. The solid circles in Figure 40b represent the values of V, calculated using Equation (3-55)

with $C = 7.0 \times 10^{-2}$, and are listed in Table XVII. These points follow the same general curve as the values of V calculated from the FWM data. Thus, the change in the amount of vibronic emission accounts for the increase of V with temperature.

Figure 41 shows the change in the resonant diffusion coefficient, D_r, with temperature. The solid line comes from using the values of $\bar{\alpha}$, predicted from the $T^{3/2}$ fitting, and V, obtained from Equation (3-55) for the change in the integrated fluorescence, and inserting these values into Equation (3-41). This line follows approximately the same curve defined by the experimentally determined resonant diffusion coefficient values. Thus the change in D_r versus temperature for emerald is due to acoustic phonon scattering, reflected in $\bar{\alpha}$, and the increase in the vibronic emission, reflected in V. These predicted values of D_r are listed in Table XVII for certain temperatures.

Discussion and Conclusions

The results described here show that there are two different types of energy transfer processes taking place in emerald. The first of these processes is a short-range spectral diffusion among Cr^{3+} ions in non-equivalent crystal field sites. This was characterized by TRSSS and the energy transfer interaction mechanism appears to be electric dipole-dipole, with multistep energy migration occurring among ions in sensitizer sites before transfer occurs to the ions in activator sites. The nonresonant diffusion coefficient for this process is of the order of 10^{-13} cm^2/s and appears to remain fairly constant with temperature. Two methods were used to characterize the spectral diffusion among Cr^{3+} ions

TABLE XVII

PREDICTED VALUES OF SPATIAL ENERGY TRANSFER PARAMETERS FOR EMERALD

Parameter	Temperature (K)							
	12.2	30	50	70	85	100	130	160
$V(10^{5}\ s^{-1})$	2.31	2.94	4.68	5.08	9.79	13.80	22.10	27.41
$D(10^{-7}\ cm^{2}/s)$	3.36	3.55	3.62	4.21	11.22	21.92	45.18	92.80

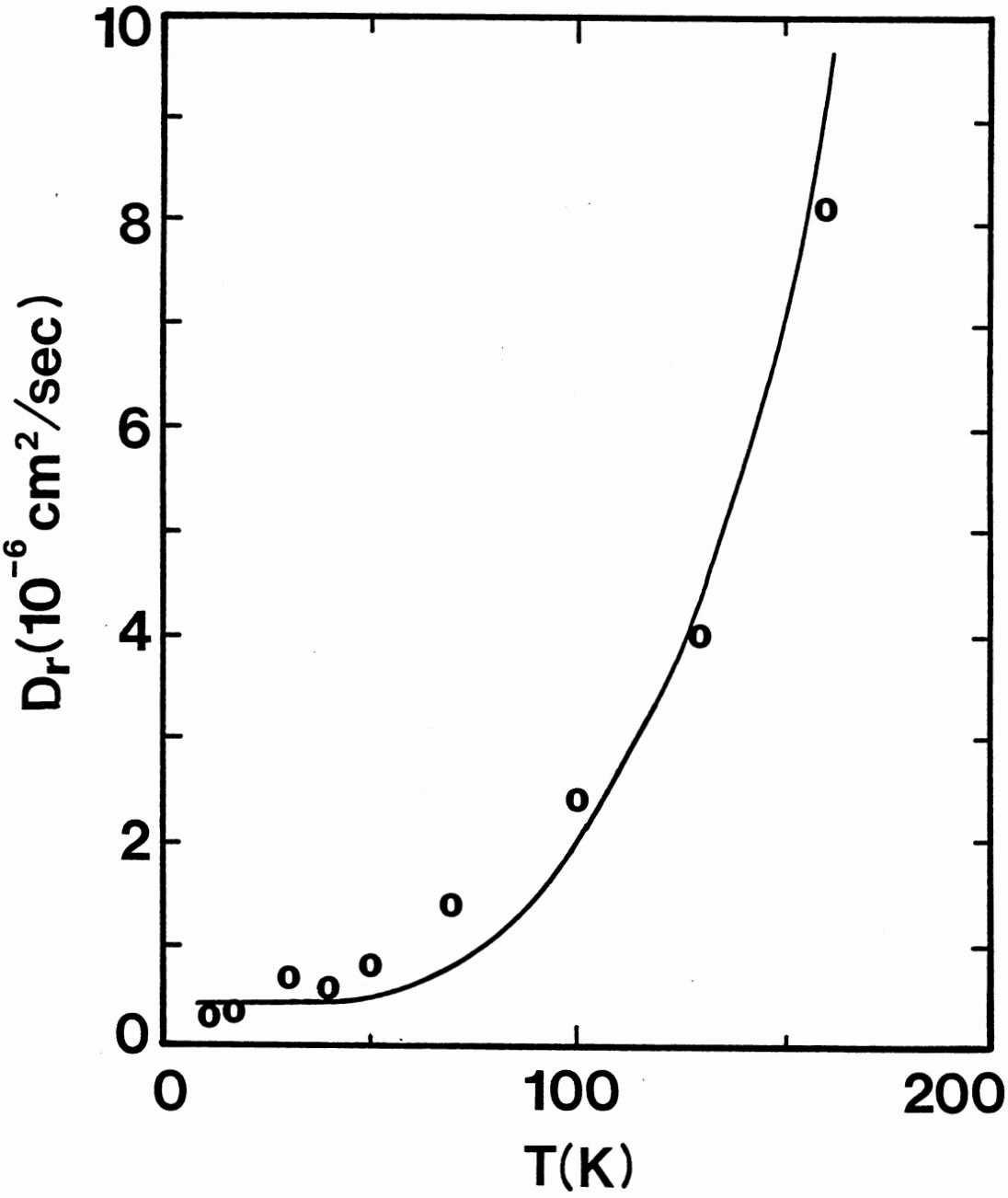

Figure 41. Temperature Dependence of the Resonant Exciton Diffusion Coefficient, D_r, with the Solid Line Given from Equation (3-41) Using Theoretical Values of $\overline{\alpha}$ and V

in nonequivalent crystal field sites and both give energy transfer rates and critical interaction distances which are consistent with each other. The diffusion coefficient calculated using the Chow-Powell theory can be compared with the value calculated from an expression derived by Förster (56) and Dexter (57). For a resonant, dipole-dipole interaction between two ions separated by a distance R, the energy transfer rate is

$$P_{dd} = \left(\frac{3\hbar^4 c^4 \sigma_a}{4\pi n^4 R^6 \tau_s}\right) \int \frac{\varepsilon_s(h\nu)\alpha_a(h\nu)}{(h\nu)^4} d(h\nu) \qquad (3\text{-}56)$$

where σ_a is the peak absorption cross-section of the activator ions, and ε_s and α_a are the normalized spectra of the sensitizer and activator absorption, respectively. The diffusion coefficient for the motion of the exciton on these sites can then be expressed in terms of the ion-ion interaction rate as (72)

$$D = \frac{1}{6} \int_a^\infty R^2 P(R) \rho(R) dR \qquad (3\text{-}57)$$

where the probability density of finding an ion at the distance R from the ion at the origin is given by

$$\rho(R) = 4\pi N_i R^2 \exp[-4\pi N_i R^3/3] \qquad (3\text{-}58)$$

where N_i is the relative concentration of Cr^{3+} ions in a particular site. For the electric dipole-dipole energy transfer interaction mechanism the diffusion coefficient becomes

$$D = \frac{4\pi N_i R_o^6}{6\tau_s} \int_a^\infty R^{-2} \exp[-4\pi N_i R^3/3] dR \quad . \qquad (3\text{-}59)$$

The lower limit of the integral, a, is taken to be 4.6 Å instead of zero,

since this is the nearest neighbor distance. Table VIII, which listed the relative concentrations of Cr^{3+} ions for this emerald sample, also lists the values of D calculated using Equation (3-59). This is of the same order of magnitude as the values calculated using the Chow-Powell model and gives us an approximate limit for D assuming diffusion among ions in similar sensitizer sites. Using this general expression for D indicates that the values calculated for the nonresonant diffusion coefficient are reasonable, within the order of magnitude.

The second energy transfer process in emerald is a long range spatial diffusion among resonant Cr^{3+} ions. This was characterized by FWM spectroscopy and the nonexponential behavior of the grating decay is consistent with the presence of long mean-free path exciton migration. The diffusion coefficient for the resonant spatial diffusion was found to be approximately 10^{-6} cm^2/s, which is much larger than that found for the spectral energy transfer. However, these are two very different types of processes, probed by two different experimental techniques, and no real comparison can be made between the magnitudes of these coefficients. It has been shown that this value of D_n is consistent with the values measured in other Cr^{3+}-doped materials which show a long-range type of spatial diffusion (72). One possible reason for the magnitude of D_n is found from an evaluation of the crystalline properties of synthetic emerald. There are local strain lines which run through the material, and it is conceivable that resonant ions lie along these lines. Then, when probing with FWM, the exciton could migrate to one of these lines and move rapidly along this path of resonant ions for a long distance before being scattered. We have not shown that this is actually the process taking place, but it is possible.

CHAPTER IV

SUMMARY AND CONCLUSIONS

Summary of the Results

In summary, the results in Chapter II help in understanding the complexity of multiphoton transitions and their interaction times with the intermediate state. For the fluoride glass, doped with trivalent europium, 266 nm and 532 nm excitation produce very similar emissions, with the 532 nm excitation producing a multiphoton transition terminating on the broad band 5d configurational level. By using a rate equation model, it is possible to solve for the two photon absorption cross-section. The main consideration in calculating σ_{2d} centers around the type of intermediate state involved. For BZLT:Eu^{3+} the intermediate state is either a virtual state very near the $^5D_1$ metastable state, or the real intermediate state, but one thing is certain, the cross-section is dependent upon the dephasing time of the intermediate state and not upon the longer fluorescence lifetime from the metastable state. Excitation at 266 nm and 532 nm in the oxide glass produced no two-photon transitions. Excitation with 354.7 nm produced interesting results in both glasses. It appears that there is either a change in the polarized local site of the ion or multiphoton excitation takes the ion well above the band edge and gives rise to shifted emissions and multiexponential decay times.

In Chapter III two spectroscopy techniques were discussed; first, time-resolved site-selection spectroscopy of emerald which probes spectral energy transfer among nonresonant Cr^{3+} ions and, second, nondegenerate four-wave mixing in emerald, which measures a long-range spatial diffusion. Both types of energy transfer processes appear to be taking place in emerald. The diffusion coefficients for each process are quite different, but are on the same order of magnitude as those seen for similar processes in other solids. The shorter-range, spectral diffusion in emerald is best analyzed with the theory of Chow and Powell and this indicates that there is a migration among sensitizer ions before transfer to the activator ions. The FWM data is best fit with the theory of Kenkre, which predicts a long mean-free path exciton migration. Thus the two energy transfer processes are quite different and two different spectroscopic techniques are used to best analyze these processes. Finally, scattering efficiency measurements were used to predict the nonradiative decay rates of the excited state.

Suggestions for Future Work

For the multiphoton spectroscopy, the best direction for the future work is in analyzing the interaction times of the intermediate state and also in probing the real versus virtual intermediates. The addition of a piosecond dye laser would allow tuning resonantly into a real intermediate level to measure the cross-section, and then detuning to determine how significant a role the nearby virtual intermediate states play in the two-photon cross-section measurements and this sum over the intermediate states. Likewise, having the ability to tune in the ultraviolet

would allow probing the 5d level and determine exactly what is taking place there.

There is still much work that can be done with emerald. A better understanding of the coupling theory in the T_2 measurements would shed a great deal of light onto the importance of nonradiative decay in vibronic laser materials. Also, having a variety of concentrations of samples would allow a better general picture of what role the sensitizers and activators play and what some of the intrinsic decay rates are. Also, it would be nice to look at how the energy transfer process changes as the samples become less or more concentrated, and to see if there are any optimum concentrations for lasing or other applications. Finally, the two-level model used in the FWM scattering efficiency evaluation assumes little or no depletion of the probe beam, but because of the absorption of Cr^{3+} ions in this region, this assumption is not strictly met. A more appropriate model might help to give better fits of the scattering efficiencey versus crossing angle data.

REFERENCES

1. Judd, B. R., Phys. Rev. 127, 750 (1962).

2. Ofelt, G. S., J. Chem. Phys. 37, 511 (1962).

3. Quarles, G. J., Spectroscopic Studies of $Y_3Al_5O_{12}:Nd^{3+}$ Under High-Power, Picosecond-Pulse Excitation, M.S. Thesis, Oklahoma State University, 1983.

4. Quarles, G. J., G. E. Venikouas, and R. C. Powell, Phys. Rev. B 31, 6935 (1985).

5. Venikouas, G. E., G. J. Quarles, J. P. King, and R. C. Powell, Phys. Rev. B 30, 2401 (1984).

6. Chow, H. C. and R. C. Powell, Phys. Rev. B 21, 3785 (1980).

7. Yokota, M., and O. Tanimoto, J. Phys. Soc. Japan 22, 779 (1967).

8. Wong, Y. M., and V. M. Kenkre, Phys. Rev. B 22, 3072 (1980); V. M. Kenkre and D. Schmid, Phys. Rev. B 31, 2430 (1985) and references therein.

9. Kramer, M. A., and R. W. Boyd, Phys. Rev. B 23, 986 (1981).

10. Fan, T. Y., and R. L. Byer, J. Opt. Soc. Am. B 3, 3454 (1986).

11. Lezama, A., and C. B. De Araujo, Phys. Rev. B 33, 3221 (1986).

12. Kholodenkov, L. E., and A. B. Makhanek, Phys. Stat. Sol. (b) 125, 365 (1984).

13. Moune-Minn, O, K., and P. Procher, C. R. Acad. Sc. Paris 300, 203 (1985).

14. Tanaka, I., and M. Kawasaki, in "Advances in Multi-Photon Processes and Spectroscopy, Vol. 1", ed. S. H. Lin, (World Scientific, Singapore, 1984), p. 239.

15. Drexhage, M. G., O. H. El-Bayoumi, C. T. Moynihan, A. J. Bruce, K. H. Chung, D. L. Gavin, and T. J. Loretz, Comm. Am. Ceramic Soc. 5, C-166 (1982).

16. Chang, N. C., J. Appl. Phys. 34, 3500 (1963).

17. Reisfeld, R., Structure and Bonding 13, 30 (1973).

18. Carnall, W. T., P. R. Fields, and K. Rajnak, J. Chem. Phys. 49, 4412, 4424, 4443, 4447, 4450 (1968).

19. Reisfeld, R., E. Greenberg, R. N. Brown, M. G. Drexhage, and C. K. Jorgensen, Chem. Phys. Lett. 95, 91 (1983).

20. Blanzant, B., L. Boehm, C. K. Jorgensen, R. Reisfeld, and N. Spector, J. Solid State Chem. 32, 185 (1980).

21. Weber, M. J., and R. F. Schaufele, J. Chem. Phys. 43, 1702 (1965).

22. Dexpert-Ghys, J., Y. Charreire, M. Leskelä, and L. Niinistö, J. Electrochem. Soc. 132, 711 (1985).

23. Struck, C. W., and W. H. Fonger, J. Lumin. 12, 456 (1970).

24. Riseberg, L. A., and M. J. Weber, Progress in Optics 14, 89 (1972).

25. Layne, C., and M. J. Weber, Phys. Rev. B 16, 3259 (1972).

26. Brecher, C., and L. A. Riseberg, Phys. Rev. B 21, 2607 (1980).

27. Yatsiv, S., W. G. Wagner, G. S. Picus, and F. M. McClung, Phys. Rev. Lett. 15, 614 (1965).

28. Eberly, J. H., and J. Krasinski, in "Advances in Multi-Photon Processes and Spectroscopy, Vol. 1", ed. S. H. Lin, (World Scientific, Singapore, 1984), p. 1.

29. Hunt, R. B., Jr., and R. G. Pappalardo, J. Lumin. 34, 133 (1985).

30. Gang, X., and R. C. Powell, J. Appl. Phys. 57, 1299 (1985).

31. Denisov, Yu. V., I. V. Kovaleva, V. P. Kolobkov, and V. V. Rastoskuev, Opt. Spectros. 38 54 (1975).

32. Axe, J. D., Jr., Phys. Rev. 136 A42 (1964).

33. McClure, D. S., and C. Pedrini, Phys. Rev. B 32, 8465 (1985); S. A. Payne, A. B. Goldberg, and D. S. McClure, J. Chem. Phys. 81, 1529 (1984); C. Pedrini, F. Rogemond, and D. S. McClure, J. Appl. Phys. 38, 2379 (1986).

34. Shand, M. L., Proc. Int. Conf. on Lasers '82, ed. R. C. Powell (S.P.S. Press, McLean, 1982), p. 799.

35. Buchert, J., A. Katz, and R. R. Alfano, Proc. Int. Conf. on Lasers '82, ed. R. C. Powell (S.P.S. Press, McLean, 1982), p. 791.

36. Shand, M. L., and J. C. Walling, IEEE J. Quantum Electronics QE-18, 1829 (1982).

37. Buchert, J., A. Katz, and R. R. Alfano, IEEE J. Quantum Electronics QE-19, 1477 (1983).

38. Shand, M. L., and S. T. Lai, IEEE J. Quantum Electronics QE-20, 105 (1984).

39. Lai, S. T., J. Opt. Soc. Am. B 4, 1286 (1987).

40. Wood, D. L., J. Chem. Phys. 42, 3404 (1965).

41. Brum-Grzhimailo, S. V., and G. V. Klimusheva, Opt. Spectr. 8, 179 (1960).

42. Morosin, B., Acta Cryst. B 28, 1899 (1972).

43. Halperin, B., D. Nicollin, and J. A. Koningstein, Chem. Phys. 42, 277 (1979).

44. Veremeichik, T. F., Phys. Stat. Sol. (b) 124, 719 (1984).

45. Hasan, Z., S. T. Keany, and N. B. Manson, J. Phys. C 19, 6381 (1986).

46. Shannon, R. D., and C. T. Prewitt, Acta Cryst. B25, 925 (1969).

47. Bragg, W. L., and J. West, Proc. R. Soc. A 111, 691 (1926).

48. Birgeneau, R. J., J. Chem. Phys. 50, 4282 (1969).

49. Edgar, A., and D. R. Hutton, J. Phys. C 11, 5051 (1978).

50. Wyckoff, R. G., Crystal Structure (Interscience Publishers, Inc., New York, 1948), Vol II., p. 7.

51. Farrell, E. F., J. H. Fang, and R. E. Newnham, Amer. Mineralogist 48, 805 (1963).

52. Price, D. C., E. R. Vance, G. Smith, A. Edgar, and B. L. Dickson, J. Physique C 6, 811 (1976).

53. Wood, D. L., J. Ferguson, K. Knox, and J. F. Dillon, Jr., J. Chem. Phys. 37, 890 (1963).

54. Kisliuk, P., and C. A. Moore, Phys. Rev. 160, 307 (1967).

55. Fonger, W. M., and C. W. Struck, Phys. Rev. B 11, 3251 (1975).

56. Förster, T., Ann. Phys. 2, 55 (1948); Z. Naturforsch 49, 321 (1949).

57. Dexter, D. L., J. Chem. Phys. 22, 836 (1953).

58. Holstein, T., S. K. Lyo, and R. Orbach, Phys. Rev. Lett. 36, 891 (1976); Rich, R. M., S. Alexander, J. Bernasconi, T. Holstein, S. K. Lyo, and R. Orbach, Phys. Rev. 18, 3048 (1979); Lyo, S. K., T. Holstein, and R. Orbach, Phys. Rev. B 18, 1637 (1978).

59. Huber, D. L., Phys. Rev. B 20, 2307 (1979); W. Y. Ching and D. L. Huber, Phys. Rev. B 18, 5320)1978); W. Y. Ching, D. L. Huber, and B. Barnett, Phys. Rev. B 17, 5025 (1978).

60. Knox, R. S., "Theory of Excitons," Academic Press, New York, 1963; Dexter, D. L. and R. S. Knox, "Excitons," Interscience, New York, 1965.

61. Frenkel, J., Phys. Z. Sowjetunion 9, 158 (1936).

62. Trlifaj, M., Czech. J. Phys. 6, 533 (1956); 8, 510 (1958).

63. Chandrasekhar, S., Rev. Mod. Phys. 15, 1 (1943).

64. Spitzer, F., "Principles of Random Walk," Van Nostrand, Princeton, 1964; Rosenstock, H. B., SIAM J. Appl. Math. 9, 169 (1961); Rudemo, R., SIAM J. Appl. Math. 14, 1243 (1966); Montroll, E. W., and G. H. Weiss, J. Math. Phys. 2, 167 (1965).

65. Merkle, L. D., Doctoral Dissertation, Oklahoma State University, Stillwater, (1978).

66. Blatt, J. M., and V. F. Weisskopf, "Theoretical Nuclear Physics," Wiley, New York, 1952.

67. Lawson, C. M., E. E. Freed, and R. C. Powell, J. Chem. Phys. 76, 4171 (1982).

68. Lawson, C. M., Doctoral Dissertation, Oklahoma State University, Stillwater, (1981).

69. Sardar, D., and R. C. Powell, J. Lumin. 22, 349 (1981).

70. Kogelnik, H., Bell Sys. Tech. J. 48, 2909 (1969).

71. Eichler, H., and H. Stahl, J. Appl. Phys. 44, 3429 (1973); J. Appl. Phys. 44, 5383 (1973).

72. Suchocki, A., G. D. Gilliland, and R. C. Powell, Phys. Rev. B 35, 5830 (1987).

73. Hill, K. O., Appl. Opt. 10, 1695 (1971).

74. Ghazzawi, A. M., J. K. Tyminski, R. C. Powell, and J. C. Walling, Phys. Rev. B 30, 7182 (1984).

75. Suchocki, A., J. D. Allen, R. C. Powell, and G. M. Loiocano, to be published in Phys. Rev. B.

76. Siegman, A. E., J. Opt. Soc. Am. 67, 545 (1977).

77. Nelson, K. A., R. Cassalegno, R. J. D. Miller, and M. D. Fayer, J. Chem. Phys. 77, 1144 (1982).

78. Lyo, S. K., Phys. Rev. B 3, 3331 (1971).

79. Fairbank, W. M., Jr., G. K. Klauminzer, and A. L. Schawlow, Phys. Rev. B. 11, 60 (1976).

80. Agranovich, V. M., and M. D. Galanin, "Electronic Excitation Energy Transfer in Condensed Matter," North Holland, New York, 1982; V. M. Agranovich and Yu. V. Konobeev, Phys. Stat. Sol. 27, 435 (1968); V. M. Agranovich and Yu. V. Konobeev, Optika i Spektroskopiya 6, 242 (1959).

81. Van Vleck, J. H., J. Chem. Phys. 41, 67 (1937).

82. Woudenberg, J. P. M., Physica 9, 217, 936 (1942).

83. Kranzen, P., J. P. M. Woudenberg, and C. J. Gorter, Physica 10, 693 (1943).

84. Hoogschagen, J., A. P. Snoek, and C. J. Gorter, Physica 11, 518 (1943).

85. Hoogschagen, J., Th. Scholte, and S. Kruyer, Physica 11, 504 (1946).

86. Hoogschagen, J., Physica 11, 513 (1946).

87. Broer, L. J. F., C. J. Gorter, and J. Hoogschagen, Physica 11, 231 (1945).

88. Hoogschagen, J., and C. J. Gorter, Physica 14, 197 (1948).

89. Peacock, R. D., in Structure and Bonding, Vol. 22, edited by J. D. Dunitz, P. Hemmerich, J. A. Ibers, C. K. Jorgensen, J. B. Neilands, D. Reinen, and R. J. P. Williams (Springer-Verlag, New York, 1975) pp. 83-122.

90. Racah, G., Phys. Rev. 62, 438 (1942); Phys. Rev. 63, 364 (1943).

91. Hessler, J. P., and W. T. Carnall in Lanthanide and Actinide Chemistry and Spectroscopy, ACS Symposium Series Vol. 131, edited by N. M. Edelstein (American Chemical Society, Washington, D. C., 1980) pp. 349-368.

92. Messiah, A., Quantum Mechanics, Vol. II (John Wiley & Sons, New York, 1961) pp. 1053-1078.

93. Hufner, S., Optical Spectra of Transparent Rare Earth Compounds (Academic Press, New York, 1978).

94. Judd, B. R., Operator Techniques in Atomic Spectroscopy (McGraw-Hill Book Company, New York, 1963).

95. Judd, B. R., J. Chem. Phys. 44, 839 (1966).

96. Krupke, W. F., Phys. Rev. 145, 325 (1966).

97. Wybourne, B. G., Spectroscopic Properties of Rare Earths (Interscience, John Wiley, New York, 1965).

98. Reisfeld, R., and C. K. Jorgensen, Lasers and Excited States of Rare Earths (Springer-Verlag, New York, 1977) pp. 87-90.

APPENDIX

THE JUDD-OFELT FORMULATION OF CRYSTAL FIELD INDUCED F-F TRANSITIONS

Introduction

The purpose of this appendix is to present the theoretical development, as well as the relationship to experimentally measurable parameters, used in the Judd-Ofelt formalization. These parameters are very useful in predicting transition probabilities, oscillator strengths, line strengths, spontaneous emission coefficients, radiative lifetimes, and branching ratios for f-f transitions in rare earth doped materials.

The first studies of these transitions were conducted in 1937 by Van Vleck (81). His results gave the first conclusive proof that the sharp line spectra of the trivalent rare earth ions were in fact due to transitions within the $4f^n$ configuration and not due to transitions from higher energy configurations, as was earlier believed. Van Vleck gave a complete development for the electric dipole, magnetic dipole, and electric quadrupole selection rules as applied to the appropriate tensor operators. His calculations for the line intensities take into account each of these three types of transitions, and he correctly identified some of the previously 'unidentified and extra' lines as being magnetic dipole in origin.

The next serious set of studies was carried out by a group of spectroscopists at the Zeeman Laboratories at the University of

Amsterdam in the early 1940's (82-87). Their studies were of rare earth ions in aqueous solution and these gave much better measurements of the absolute intensities of the different spectra. This groups' calculations made some adjustments in Van Vleck's (81) conclusions, mainly in the order of magnitude of the strength of the magnetic dipole and electric quadrupole transitions. A complete tabulation of all known oscillator strengths for the rare earth aquo ions appeared in 1948 (88) and no other intensity data appeared until the now famous simultaneous papers on the theory of lanthanide intensities by Judd (1) and Ofelt (2), both in 1962.

The following sections will primarily be focused on the Judd-Ofelt formulation of crystal field induced electric dipole transitions in the $4f^n$ configurations. The considerations in the following sections will hold primarily for the rare earth ions. It is well known that the four dominant sources of optical radiation in rare earth crystal spectra are:

(i) Forced electric dipole radiation induced by odd terms of the crystal field

(ii) Forced electric dipole radiation induced by lattice vibrations

(iii) Allowed magnetic dipole radiation

(iv) Allowed electric quadrupple radiation

The experimental data on the solid state spectra of rare earths shows that the radiation is mostly electric dipole in nature, although some cases of magnetic dipole radiation are also observed (18). In free atoms the magnetic dipole radiation is typically about six orders of magnitude weaker than that of electric dipole radiation. Because most spectra observed is forced electric dipole, the development of this section will be concentrated towards this type of transition. At the

end, a brief overview of these other types of transitions will be presented, as well as how their theoretical development differs.

Forced Electric Dipole Transitions

The Judd-Ofelt theory can be most formally described through the use of tensor operators, n-j symbols, and reduced matrix elements. A brief description and definition of each will be given for a better understanding of the Judd-Ofelt theory.

Tensor Operators

An irreducible tensor operator of rank k, $\overleftrightarrow{T}^{(k)}$ is defined as that collection of components

$$\overleftrightarrow{T}^{(k)}_{-k} , \overleftrightarrow{T}^{(k)}_{-k+1}, \ldots , \overleftrightarrow{T}^{(k)}_{q} , \ldots \overleftrightarrow{T}^{(k)}_{k-1} , \overleftrightarrow{T}^{(k)}_{k} \qquad \text{(A-1)}$$

These components may be transformed under rotations according to

$$\overleftrightarrow{T}^{(k)}_{q}(\text{new}) = \sum_{q'} \vec{D}^{(k)}_{qq'} \overleftrightarrow{T}^{(k)}_{q'}(\text{old}) \qquad \text{(A-2)}$$

where we define $\vec{D}^{(k)}$ as a general rotation matrix of rank k (89). To calculate the matrix elements of tensor operators in momentum space, it is necessary to start with Racah's definition (90) for the irreducible tensor, $\overleftrightarrow{C}^{(k)}$, which transforms as spherical harmonics, having components

$$\overleftrightarrow{C}^{k}_{q} = \left(\frac{4\pi}{2k+1}\right)^{1/2} Y_{kq} \qquad \text{(A-3)}$$

where Y_{kq} is the spherical harmonic of rank k. Thus, as an example:

$$\overleftrightarrow{C}^{o}_{o} = (4\pi)^{1/2} Y_{oo} = 1 \tag{A-4}$$

The position vector $\vec{r}$ is a tensor of rank=1, and is thus related to $\vec{C}^{(1)}$ as:

$$\vec{r} = r\, \vec{C}^{(1)} \tag{A-5}$$

Since the tensor varies from $-k \rightarrow +k$, the components of the position vector are given by (89):

$$\vec{r}_{(+1)} = r\, \vec{C}^{(1)}_{1} = r\left(\frac{4\pi}{3}\right)^{1/2} Y_{11} = -\frac{1}{\sqrt{2}}(x+iy)$$

$$\vec{r}_{o} = r\, \vec{C}^{(1)}_{o} = r\left(\frac{4\pi}{3}\right)^{1/2} Y_{10} = Z \tag{A-6}$$

$$\vec{r}_{(-1)} = r\, \vec{C}^{(1)}_{-1} = r\left(\frac{4\pi}{3}\right)^{1/2} Y_{11} = \frac{1}{\sqrt{2}}(x-iy)$$

Now, looking at forced electric dipole transitions, it is useful to employ the electric dipole moment operator

$$\vec{P} = -e \sum_{i} \vec{r}_{i} = -e \sum_{i} r_{i} \left(\vec{C}^{(1)}\right)_{i} \tag{A-7}$$

where $\vec{P}$ is the sum over all the electrons of the position vectors of these electrons (24). (Note that some papers will label this operator as $\vec{P}=\vec{E}_{p}$.) In relating Equation (A-7) back to Equation (A-2), this operator is equivalent to

$$\vec{P} = -e\, \vec{D}_{1} \tag{A-8}$$

where, when relating this to the position vector:

$$\vec{P} = -e \vec{D}^{(1)}_q \quad , \; q = \pm 1, \; 0. \tag{A-9}$$

Another operator that will come into play in the Judd-Ofelt theory is the Crystal Field Operator, $\vec{V}^{C.F.}$. This is a general tensor of rank t,

$$\begin{aligned} \vec{V}^{C.F.} &= \sum_{t,p} A_{tp} \sum_i r_i \left(\vec{C}^{(t)}_p \; (\theta_i, \phi_i) \right) \\ &= \sum_{t,p} A_{tp} \vec{D}^{(t)}_p \end{aligned} \tag{A-10}$$

where A_{tp} are called the crystal field parameters (91).

Matrix Elements and Reduced Matrix Elements

The known selection rules for electric dipole transitions are given by

$$\Delta l = \pm 1 \; ; \; \Delta S = 0 \; ; \; |\Delta L| \; , \; |\Delta J| \leq 2l$$

where for the rare earth elements, l=3. It is obvious that transitions between f^n levels involve no change in parity, thus, electric dipole transitions are forbidden by Laporte's rule. However, such transitions do become allowed if odd harmonics in the static or dynamic crystal field admix states of opposite parity into $4f^n$. This can occur statically if the rare earth ions reside in a lattice site lacking inversion symmetry (eg, $C_1, C_{3v}, D_{2d}, D_4, S_4, T, T_d$, and 0). First, in Equation (A-10), it is necessary to consider the admixing by the odd parity terms (t=odd) in the crystal field expansion. Since the electric dipole operator is odd, it is necessary to have the admixing of odd terms to give nonzero matrix elements.

It has been shown that the Hamiltonian of an ion in a lattice can be written as (91)

$$H = H_o + H_o + H_{cryst} + H_{so} \tag{A-11}$$

where

$$H_o = \sum_{i=1}^{n} \frac{p_i^2}{2m} - \frac{ze^2}{r_i} \tag{A-12}$$

is the unperturbed or free ion Hamiltonian, and where

$$H_{el} = \sum_{j>1}^{n} \sum_{i=1}^{n} \frac{e^2}{r_{ij}} \tag{A-13}$$

is the electrostatic interaction between electrons. Likewise the remaining two terms

$$H_{cryst} = \sum_{i=1}^{n} e\, \bar{V}^{C.F.}(r_i, \theta_i, \phi_i) \tag{A-14}$$

$$H_{so} = \lambda \vec{L} \cdot \vec{S} \tag{A-15}$$

are known as the crystal field perturbation and spin orbit interaction respectively. Now, expanding the eigenstates to include the perturbation due to this crystal field term, in first order, gives the eigenstate for the a^{th} level of the f^n configuration as (24)

$$|\psi_a\rangle = |\phi_a\rangle - \sum_{\beta} \frac{\langle\phi_\beta|V_{odd}|\phi_a\rangle|\phi_\beta\rangle}{(E_a - E_\beta)} \tag{A-16}$$

where the state is defined by:

$$|\phi_a\rangle = |4f^n \alpha\ SLJM_J\rangle \quad . \tag{A-17}$$

For this case, the states of the $4f^n$ configuration are considered to be linear combinations of the Russell-Saunders coupled states. Note that the summation is over the states of the configurations having opposite parity. Also, the term (α) represents all other quantum numbers other than S,L,J and M_J which are required to completely specify the state.

In order to begin evaluating the transition probabilities it is necessary to evaluate the appropriate matrix elements:

$$\langle \alpha SLJM_J | \overleftrightarrow{T}^{(k)}_q | \alpha S'L'J'M_J' \rangle \ . \qquad \text{(A-18)}$$

It is possible to see that since there are (2k+1) components of the operator and (2J+1) values of M_J, there will generally be (2k+1) x (2J+1) x (2J'+1) separate matrix elements to evaluate for every $J \rightarrow J'$ transition.

To simplify the evaluation of this problem, it is possible to apply the Wigner-Eckart theorem to the matrix elements. The Wigner-Eckart theorem will produce a product of a reduced matrix element, which depends on J,J', and k, but not on M_J,M_J', or q (i.e., the matrix element is component independent) and a 3-j symbol whose value depends upon these components which are considered. The usual form of the Wigner-Eckart Theorem is

$$\langle \alpha JM_J | \overleftrightarrow{T}^{(k)}_q | \alpha' J' M_J' \rangle = C(J'M_J'kq:JMJ'k) \frac{\langle \alpha J || \overleftrightarrow{T}^{(k)} || \alpha' J' \rangle}{(2J+1)^{1/2}} \qquad \text{(A-19)}$$

however, the form with the 3-j symbol is written as (92)

$$\langle \alpha SLJM_J | \overleftrightarrow{T}^{(k)}_q | \alpha' S' L' J' M_J' \rangle = (-1)^{J-M_J} \begin{pmatrix} J & k & J' \\ -M_J & q & M_J' \end{pmatrix} \times \langle \alpha SLJ || \overleftrightarrow{T}^{(k)} || \alpha' S' L' J' \rangle \tag{A-20}$$

where the 3-j symbols are typically written as:

$$\begin{pmatrix} J & k & J' \\ -M_J & q & M_J' \end{pmatrix} \equiv \begin{pmatrix} j_1 & j_2 & j_3 \\ m_1 & m_2 & m_3 \end{pmatrix} . \tag{A-21}$$

The 3-j symbols are related to the Clebsch-Gordon coefficients through

$$\begin{pmatrix} j_1 & j_2 & j_3 \\ m_1 & m_2 & m_3 \end{pmatrix} = (-1)^{j_1 - j_2 - m_3} C(j_1 m_1 j_2 m_2 : j_1 j_2 j_3 - m_3)(2j_3+1)^{-1/2} \tag{A-22}$$

and the values of these terms are tabulated similarly to the tables for the Clebsch-Gordon coefficients (92).

It is also possible to couple the angular momentum (j_1, j_2, j_3) to give a resultant j. Using an analogous process for further reducing the reduced matrix elements, it is also possible to express the matrix element with a 6-j symbol (92):

$$\langle \alpha SLJ || \overleftrightarrow{T}^{(k)} || \alpha' S' L' J' \rangle = \delta(SS') \ (-1)^{S+L'+J+k} \times [(2J+1)(2J'+1)]^{1/2} \begin{Bmatrix} L & k & L' \\ J' & S & J \end{Bmatrix} \langle \alpha SL || \overleftrightarrow{T}^{(k)} || \alpha' S' L' \rangle . \tag{A-23}$$

A common notation for the 6-j symbol is given as:

$$\begin{Bmatrix} L & K & L' \\ J' & S & J \end{Bmatrix} \equiv \begin{Bmatrix} j_1 & j_2 & j_3 \\ J_1 & J_2 & J_3 \end{Bmatrix} . \tag{A-24}$$

For a nonzero term, the selection rules specify that the elements of each of the triads

$$(j_1 j_2 j_3)\ (j_1 J_2 J_3)\ (J_1 j_2 J_3)\ (J_1 J_2 j_3)$$

(i) satisfy the triangular inequalities

(ii) have an integral sum.

These 3-j and 6-j symbols will come into play later when developing the expressions for the oscillator strengths and line strengths.

Judd-Ofelt Theory

The first term to look at in the development of Judd-Ofelt theory is the oscillator strength. The oscillator strength of a component of the electric dipole transition from a ground state $|A\rangle$ to an excited state $|B\rangle$ is given by (93)

$$f^{e.d.} = \chi\left[\frac{8\pi^2 mc\sigma}{he^2}\right] |\langle A|\vec{P}|B\rangle|^2 \qquad \text{(A-25)}$$

but, using the definition from Equation (A-9)

$$\vec{P} = -e\overset{\leftrightarrow}{D}{}^{(1)}_{q} \quad , q = \pm 1,0$$

it is possible to write the oscillator strength as

$$f^{e.d} = \chi\left[\frac{8\pi^2 mc\sigma}{h}\right] |\langle A|\overset{\leftrightarrow}{D}{}^{(1)}_{q}|B\rangle|^2 \qquad \text{(A-26)}$$

where m is the mass of the electron, h is Plank's constant, c is the speed of light, σ is the energy of the transition in cm^{-1} and χ is the

Lorentz field correction for the refractivity of the medium. For electric dipole transitions the most common expression used for the Lorentz field correction is (24)

$$\chi = \frac{n(n^2+2)^2}{9} \tag{A-27}$$

where n is the index of refraction.

Using the expansion of the crystal field potential in Equation (A-10) and the expansion of the states given in Equation (A-16), it is possible to write the ground and excited states as

$$|A\rangle = |\phi_a\rangle + \sum_\beta \frac{\langle\phi_\beta|\langle\phi_a|\overline{V}^{C.F.}|\phi_\beta\rangle}{(E_a - E_\beta)}$$

$$|B\rangle = |\phi_b\rangle + \sum_\beta \frac{\langle\phi_\beta|\langle\phi_b|\overline{V}^{C.F.}|\phi_\beta\rangle}{(E_b - E_\beta)} \tag{A-28}$$

where

$$|\phi_a\rangle = |4f^n \alpha J M_J\rangle \quad , \quad |\phi_b\rangle = |4f^n, \alpha' J' M_J'\rangle \tag{A-29}$$

and

$$|\phi_\beta\rangle = |f^n, \alpha'', J'', M_J''\rangle \tag{A-30}$$

and β stands for all the quantum numbers of the excited configuration (i.e., the higher energy, opposite parity terms).

Making use of the correspondence principle for the states and the fact that the crystal field parameter is Hermitian, it is now possible to write an expression for the oscillator strength:

$$f^{e.d.} = \chi\left[\frac{8\pi^2 mc\sigma}{h}\right]\left\{\sum_{\beta,t,p} A_{tp}\left[\frac{\langle\phi_a|\overleftrightarrow{D}_q^{(1)}|\phi_\beta\rangle\langle\phi_\beta|\overleftrightarrow{D}_p^{(1)}|\phi_b\rangle}{(E_b-E_\beta)}\right.\right. \tag{A-31}$$

$$\left.\left. + \frac{\langle\phi_a|\overleftrightarrow{D}_p^{(1)}|\phi_\beta\rangle\langle\phi_\beta|\overleftrightarrow{D}_q^{(1)}|\phi_b\rangle}{(E_a-E_\beta)}\right]\right\}^2 .$$

It is now desirable to reduce this equation into a usable expression. For the purpose of brevity, only operations on the first half of the above expression will be shown, since the same treatment will be used for both terms.

First, combining Equations (A-7) and (A-9) gives

$$\vec{P} = -e\sum_i r_i(\overleftrightarrow{C}_q^{(1)})_i = -e\,\vec{D}_q^{(1)}$$

but, expressing the operators in this term as

$$\vec{D}_q^{(1)} = \sum_i r_i^{(1)}\,(\overleftrightarrow{C}_q^{(1)})_i \tag{A-32}$$

and

$$\vec{D}_p^{(t)} = \sum_i r_i^{(t)}\,(C_p^{(t)})_i \tag{A-33}$$

gives a rewritten first term:

$$\sum_{\beta,t,p} A_{t,p}\left\{\frac{\langle\phi_a|\sum_i r_i^{(1)}(C_q^{(1)})_i|\phi_\beta\rangle\langle\phi_\beta|\sum_i r_i^{(t)}(C_p^{(t)})_i|\phi_b\rangle}{(E_b-E_\beta)}\right\}.$$

Included in the previously defined term α are the quantum numbers (n and l), where n is the principal quantum number and l is the angular momentum quantum number. If the matrix elements are written in integral form, then the total wave function can be written as a product of

Laguerre polynomials, spherical harmonics, and a phase factor. The typical hydrogen-like wave function appears as:

$$\psi_{nlm}(r,\theta,\phi,t) = R_{nl}(r)\ Y_l^m(\theta,\phi)\ e^{-iE_nt/\hbar} \quad . \tag{A-34}$$

Pulling the n and l quantum numbers out of the α term, it is possible to define the radial integral by (2)

$$\int_o^\infty R_{nl}(r)\ r^k\ R_{n'l'}dr = \langle nl|r^k|n'l'\rangle \tag{A-35}$$

where, for this case, (R/r) is the radial part of the above wave function. Thus the first term can now be rewritten as:

$$\sum_{\beta,t,p,i} A_{tp} \left\{ \frac{\langle\phi_a|r_i^{(1)}(\vec{C}_q^{(1)})_i|\phi_\beta\rangle\langle\phi_\beta|r_i^{(t)}(\vec{C}_p^{(t)})_i|\phi_b\rangle}{(E_b-E_\beta)} \right\}$$

$$= \sum_{\beta,t,p,i} A_{tp} \left\{ \frac{\langle\phi_a|(\vec{C}_q^{(1)})_i|\phi_\beta\rangle\langle\phi_\beta|(\vec{C}_p^{(t)})_i|\phi_b\rangle}{(E_n-E_\beta)} \right\} \tag{A-36}$$

$$x\ \langle 4f^n|r^{(1)}|nl\rangle\langle nl|r^{(t)}|4f^n\rangle \quad .$$

Next, it is possible to further simplify the above expression by making use of the generalized closure relation. As Judd writes: The occurrence of the structure

$$|\phi_\beta\rangle\langle\phi_\beta|$$

in Equation (A-36), "Suggests that it might be possible to adapt the closure procedure in some way, thereby uniting $\vec{C}_q^{(1)}$ and $\vec{C}_p^{(t)}$ into a single operator that acts between the states of the $4f^n$ configuration" (1).

He went on further to make the assumption that the "splittings within the multiplets of the excited configurations are negligible compared with the energies that the configurations as a whole lie above. This amounts to assuming that E_β is independent of J''" (1).

Thus if the energy of the perturbing configuration is invariant with respect to α'', J'', and M_J'' then it is possible to write an exact equation (88)

$$\sum_{\substack{\alpha''S''L'' \\ J''M_J''i}} \langle\phi_a|(\vec{C}_q^{(1)})_i|\phi_\beta\rangle\langle\phi_\beta|(\vec{C}_p^{(t)})_i|\phi_b\rangle$$

$$= (-1)^{p+q+\lambda}[\lambda]\begin{pmatrix} 1 & \lambda & p \\ q & (-p-q) & p \end{pmatrix}\langle\phi_a|\sum_i\left\{(\vec{C}_q^{(1)}\vec{C}_p^{(t)})^{(\lambda)}_{-p-q}\right\}_i|\phi_b\rangle \tag{A-37}$$

where $[\lambda] = (2\lambda + 1)$ is an abbreviation introduced here.

Now, it is possible to define a product tensor operator as

$$\overleftrightarrow{C}_{qk}(\theta,\phi) = \overleftrightarrow{U}_{kq}(\theta,\phi)C'_{kq} \tag{A-38}$$

where $\overleftrightarrow{U}_{kq}$ is now the normalized angular tensor operator and C'_{kq} is simply a corresponding normalization matrix element (94) . Thus using the product operator techniques, Equation (A-37) can be further simplified to yield:

$$= (-1)^{p+q+f+1}[\lambda][f][1]\begin{pmatrix} 1 & \lambda & t \\ q & (-p-q) & p \end{pmatrix}\begin{Bmatrix} 1 & t & \lambda \\ f & f & 1 \end{Bmatrix}$$

$$\times \langle f||C'^{(1)}||1\rangle\langle 1||C'^{(t)}||f\rangle\langle\phi_a|\overleftrightarrow{U}^{(\lambda)}_{-p-q}|\phi_b\rangle \tag{A-39}$$

Judd later argued that the above assumption might present a somewhat weak link in his own theory (95), however, most data analysis is not

effected by this simplification. Judd also made another even less justified assumption in his theory, however it does simplify things considerably. He assumed that the energy denominators were equal, (1)

$$E_a - E_\beta \equiv E_b - E_\beta = \Delta E \quad . \tag{A-40}$$

This implies that the configurations used for the admixing lie far above the states involved in the optical transitions. This is certainly a rather bad approximation for certain of the rare earths where the energy of, say, the $4f^{n-1}5d$ configuration is not very much greater than that of the $J \rightarrow J'$ transitions being considered. Such an example is Pr^{3+}, (18) where the first 4f-5d absorption in CaF_2 is located at about 250nm, which is very close to optical transitions of the 4f configuration. However, if the assumption is applied to both halves of Equation (A-31), then both halves will differ only in their 3-j symbol. Then the oscillator strength will appear as:

$$f^{e.d.} \alpha \sum_{p,t} A_{tp} \left\{ \Gamma \begin{pmatrix} 1 & \lambda & t \\ q & (-p-q) & p \end{pmatrix} + \Gamma \begin{pmatrix} t & \lambda & 1 \\ p & (-p-q) & q \end{pmatrix} \right\} . \tag{A-41}$$

From the symmetry properties of the 3-j symbols (92), permutations of any two columns are described by

$$\begin{pmatrix} j_1 & j_2 & j_3 \\ m_1 & m_2 & m_3 \end{pmatrix} = (-1)^{j_1+j_2+j_3} \begin{pmatrix} j_2 & j_1 & j_3 \\ m_2 & m_1 & m_3 \end{pmatrix} \tag{A-42}$$

then

$$\begin{pmatrix} 1 & \lambda & t \\ q & (-p-q) & p \end{pmatrix} = (-1)^{1+\lambda+t} \begin{pmatrix} t & \lambda & 1 \\ p & (-p-q) & q \end{pmatrix} \tag{A-43}$$

and since it has been assumed that t=odd for admixing to give nonzero matrix elements, it can finally be written as

$$= (-1)^{\lambda} \begin{pmatrix} t & \lambda & 1 \\ p & (-p-q) & q \end{pmatrix} .$$

Thus the two halves of Equation (A-31) will be equal if λ is even, and they will exactly cancel if λ is odd. This simplification of removing all odd λ-terms only occurs by introduction of the average energy denominator term. The 6-j symbol now restricts λ to values less than or equal to 6 (92). Because of the restriction that the sum of all the j values must be integer, the only possible values are 0→7 (since $4f^n$ has up to 14 electrons), thus the even terms are λ = 2, 4, and 6.

Thus the oscillator strength, with its new requirements on its possible summation terms, is given by

$$f^{e.d} = \chi\left[\frac{8\pi^2 mc\sigma}{h}\right]\left[\sum_{\substack{p,t \\ \lambda \equiv \text{even}}} (-1)^{p+q} [\lambda] A_{tp} \begin{pmatrix} 1 & \lambda & t \\ q & (-p-q) & p \end{pmatrix}\right. \tag{A-44}$$

$$\left. x \begin{Bmatrix} J & \lambda & J' \\ -M_J & (-q-p) & M'_J \end{Bmatrix} \boxed{\vdash} (t,\lambda) \langle 4f^n \alpha J || \hat{U}^{(\lambda)} || 4f^n \alpha' J' \rangle \right]^2$$

where

$$\boxed{\vdash}(t,\lambda) = 2 \sum_{l,n} (-1)^{f+l} [f][l] \begin{Bmatrix} 1 & \lambda & t \\ f & 1 & f \end{Bmatrix} \tag{A-45}$$

$$\frac{\langle f||C'^{(1)}||l\rangle\langle l||C'^{(t)}||f\rangle\langle 4f^n|r|nl\rangle\langle nl|r^t|4f^n\rangle}{\Delta E} .$$

Equation (A-44) is equipped to deal with transitions between individual Stark levels. However another simplification can be made here in the

Judd-Ofelt theory, although this time the simplification comes about from actual observation of experimental data, and not from a mathematical assumption. In most all spectroscopy of rare earth doped materials, the transitions between Stark split levels cannot be distinguished. Thus if it is assumed that the spectra is taken at high enough temperatures so that all components of the ground state are equally populated, that is, that the spectra is taken around room temperature, then it simplifies matters to sum over all the Stark levels of the ground state (1,2). At the same time it is possible to carry out the summation over the components $C'^{(1)}$ and $C'^{(t)}$. These assumptions are appropriate for isotropic light, especially when comparing the total absorption and emission intensities between terms. When carrying out the sum over the components of the 3-j symbols, and making use of their known properties (92), these now simply become

$$\left[(1/3)^{1/2} \; (1/2J+1)^{1/2} \; (1/2t+1)^{1/2} \right] .$$

Making the above substitution now leads to an expression for the oscillator strength

$$f^{e.d.} = \chi \left[\frac{8\pi^2 mc\sigma}{3h} \right] \sum_{\lambda=2,4,6} \Omega_\lambda \frac{|\langle 4f^n \alpha J || \overleftrightarrow{U}^{(\lambda)} || 4f^n \alpha' J' \rangle|^2}{(2J+1)} \qquad \text{(A-46)}$$

where

$$\Omega_\lambda \equiv [\lambda] \sum_{p,t} | A_{t,p} |^2 \begin{Bmatrix} \cdot & \cdot & \lambda \\ \cdot & \cdot & t \end{Bmatrix}^2 (t,\lambda)(2t+1)^{-1} . \qquad \text{(A-47)}$$

This is the standard form of the expression for the oscillator strength in the Judd-Ofelt formalism (24).

The coefficients Ω_2, Ω_4, and Ω_6 are tabulated intensity parameters that are usually derived empirically by a fitting program. These parameters are fit after inserting into a program the known values for the unit angular tensor matrix elements. These elements are calculated from wave function analysis and a very complete tabulation of such parameters has been published by Carnall, et al. (18). A sample of the typical values for the oscillator strengths, Ω_λ, and $\overleftrightarrow{U}^{(\lambda)}$ terms are given in Table I and Table II.

As a brief review, it has been shown that the Ω_λ coefficients involve:

(i) The odd harmonics in the expansion of the local crystalline field, which admix opposite parity states into the $4f^n$ configuration, thereby allowing the forced electric dipole transitions.

(ii) The energy separations of states of the $4f^n$ and opposite parity configurations.

(iii) The interconfigurational radial integrals.

These properties depend on the local environment and large site-to-site variations in the Ω_λ values are possible. However, since the $\overleftrightarrow{U}^{(\lambda)}$ are wavefunction dependent there is very little site or host dependence.

Finally, a review of the selection rules shows the following:

(i) $\lambda \leq 6$, and λ is even, thus $\lambda=2,4,6$

(ii) $t \leq 7$, and t is odd, thus $t=1,3,5,7$

(iii) Combining (i) and (ii) gives:

$\lambda=2$ $t=1,3$

$\lambda=4$ $t=3,5$

$\lambda=6$ $t=5,7$

where the principal selection rule for the above properties is the triangular inequality:

$$|j_1-j_2| \leq J \leq |j_1+j_2| \quad \underline{\text{or}} \quad |l-\lambda| \leq t \leq |l+\lambda| \tag{A-48}$$

(iv) $\Delta l=\pm 1$ thus l=d or l=g configurations

(v) $\Delta S=0$, from the $\delta(S,S')$ in Equation (A-23)

(vi) $|\Delta J|, |\Delta L| \leq \lambda$.

The selection rules on S and L are valid in the limit of Russell-Saunders coupling, but since transitions are generally between linear combinations of these states, these rules are not always rigidly adhered to. As an example, the $^5D_2$ labelled state in Eu^{3+} is simply a linear combination of the $^5D_2$ and $^7F_2$ states in the $^5D_2 \longrightarrow {}^7F_0$ transition. The selection rules on J are much more rigid and can only be broken by "J-mixing", which is typically a rather weak effect.

Related Electric Dipole Equations

From Equations (A-46) and (A-47), which define the oscillator strength, it is now possible to find a whole series of expressions which can relate theoretical derivations to experimentally measured parameters. The first of these, based on the analysis by Judd (1) is the Line strength, S. The line strength is related to the electric dipole moment operator as

$$S^{e.d.} = (1/e^2)\left|\langle A|\vec{P}|B\rangle\right|^2 \tag{A-49}$$

or, writing in terms of the oscillator strength gives:

$$S^{e.d.} = \left[\frac{h}{8\pi^2 mc\sigma\chi}\right] f^{e.d.}$$

$$= \sum_{\lambda=2,4,6} \Omega_\lambda \left|\langle 4f^n \alpha J \| \overleftrightarrow{U}^{(\lambda)} \| 4f^n \alpha' J' \rangle\right|^2 . \qquad \text{(A-50)}$$

The next important parameter often listed in the literature is the Integrated Absorption Coefficient (96). This coefficient is also directly related to the electric dipole moment operator matrix elements by the expression

$$\int k(\lambda)d\lambda = \rho \frac{8\pi^3\bar{\lambda}}{3ch}\left[\frac{(n^2+2)^2}{9}\right]\left|\sum_{A,B} \langle A|\vec{P}|B\rangle\right|^2 \qquad \text{(A-51)}$$

where ρ is the rare earth ion density in the lattice, and $\bar{\lambda}$ is the peak wavelength of the transition. This term may also be related to the oscillator strength through

$$\int k(\lambda)d\lambda = \frac{\rho\pi\bar{\lambda}e^2}{3c^2 m\sigma}\left[\frac{9\chi^2}{n^3}\right] f^{e.d.}$$

$$= \rho \frac{8\pi^3\bar{\lambda}}{3ch}\frac{\chi}{n^2} \sum_{\lambda=2,4,6} \Omega_\lambda \left|\langle 4f^n \alpha J \| \overleftrightarrow{U}^{(\lambda)} \| 4f^n \alpha' J' \rangle\right|^2 (2J+1)^{-1} \qquad \text{(A-52)}$$

The next analogous quantity probably is the one most often used to compare the theory and experimental data. This quantity is the Spontaneous Emission Coefficient,

$$A^{e.d.}(j,j') = \frac{8\pi^2\sigma^2 e^2}{mc} f^{e.d.}$$

$$= \chi\left[\frac{(8\pi^2 e)^2}{3h}\right]\sigma^3 \sum_{\lambda=2,4,6} \Omega_\lambda \left|\langle 4f^n \alpha J \| \overleftrightarrow{U}^{(\lambda)} \| 4f^n \alpha' J' \rangle\right|^2 (2J+1)^{-1} \qquad \text{(A-53)}$$

This is indeed a most useful expression, for starting with spectroscopic measurements, one can work in reverse order to find all the previously listed quantities. This is made possible due to the fact that two other quantities, the Radiative Lifetimes and the Fluorescence Braching Ratios, from a level "a" to a level "b" are defined, respectively, in terms of the spontaneous emission coefficient by

$$\left\{ 1/\tau_a^{rad} \right\} = \sum_b A_{ab} \tag{A-54}$$

and

$$\beta_{ab} = A_{ab} / \sum_b A_{ab} = \tau_a^{rad} A_{ab} \tag{A-55}$$

where the summation over "b" is simply the summation over all terminal levels. Both of these terms are easily measurable in the laboratory and lead to a simple way of gathering values for all other quantities in Equations (A-46), (A-47) and (A-49) → (A-53). This concludes the evaluation of f↔f electric dipole transitions through the formalism of the Judd-Ofelt theory. As was shown, after a careful evaluation of the matrix elements involving the electric dipole moment operator in the oscillator strength equation, it is possible to relate a series of other parameters in terms $f^{e.d.}$.

In the next two sections a brief treatment of the other possible transitions in rare earth doped materials, namely the magnetic dipole and electric quadrupole allowed transitions, will be studied. Each will be developed on the basis of a good understanding of the forced electric dipole method, with similar or detailed steps omitted. The first section will deal with magnetic dipole transitions.

Allowed Magnetic Dipole Transitions

Just as with the case of the electric dipole transition section, the first step is to define the appropriate operator. The magnetic dipole moment operator is defined by:

$$\vec{M} = -\frac{e\hbar}{2mc} \sum_i (\vec{L}_i + 2\vec{S}_i) \quad . \tag{A-56}$$

However, there exists a difference from here on. Where as for the electric dipole case, $\vec{P}$ was of odd parity. $\vec{M}$ is defined of even parity, thus, transitions between the states of the $4f^n$ configuration are allowed. So, there is no requirement for a change in parity between initial and final states. It is thus easier to calculate the oscillator strengths, which are defined by

$$\begin{aligned} f^{M.D.} &= \left[\frac{8\pi^2 mc}{h^3 e^2}\right] 4\pi^2 \chi' \left|\langle A|\vec{M}|B\rangle\right|^2 \\ &= \left[\frac{32\pi^4 mc}{h^3 e^2}\right] \chi' \frac{e^2h^2}{4m^2c^2} \left|\langle 4f^n \alpha JM_J|\vec{L}+2\vec{S}|4f^n \alpha' J' M_J'\rangle\right|^2 \\ &= \left[\frac{2\pi^2}{hmc}\right] \chi' \left|\langle 4f^n \alpha JM_J|\vec{L}+2\vec{S}|4f^n \alpha' J' M_J'\rangle\right|^2 \end{aligned} \tag{A-57}$$

where, once again, the free-ion approximation for defining the states of the $4f^n$ configuration as being linear combinations of the Russell-Saunders coupled states has been used. Since there is no need to worry about admixing the odd harmonic terms of the crystal field potential, it is possible to simply apply the Wigner-Eckart theorem to the matrix elements in Equation (A-57):

$$\langle f^n \alpha J M_J | \vec{L}+2\vec{S} | f^n \alpha' J' M_J' \rangle$$

$$= (-1)^{J-M_J} \begin{pmatrix} J & k & J' \\ -M_J' & q & M_J' \end{pmatrix} \langle f^n \alpha J || \vec{L}+2\vec{S} || f^n \alpha' J' \rangle \quad . \tag{A-58}$$

Once again, it is convenient to reduce this further by employing the convention for isotropic light and summing over the three polarizations to give:

$$\begin{pmatrix} J & k & J' \\ -M_J & q & M_J' \end{pmatrix} \Longrightarrow (1/3)^{1/2} (1/_{2J+1})^{1/2} \quad . \tag{A-59}$$

The magnetic dipole Oscillator Strength appears in final form as:

$$f^{M.D.} = \chi' \left[\frac{2\pi^2}{3hmc} \right] \frac{|\langle f^n \alpha J || \vec{L}+2\vec{S} || f^n \alpha' J' \rangle|^2}{(2J+1)} \quad . \tag{A-60}$$

Just as was done previously, relationships to the line strength and spontaneous emission coefficient can be developed. The magnetic dipole allowed Line Strength is given as

$$S^{M.D.} = \left[\frac{e^2 h^3}{32\pi^4 mc} \right] (\chi')^{-1} f^{M.D.}$$

$$= \beta^2 |\langle f^n \alpha J || \vec{L}+2\vec{S} || f^n \alpha' J' \rangle|^2 \; ; \; \beta = \left(\frac{e\hbar}{2mc} \right) \tag{A-61}$$

and the Spontaneous Emission Coefficient can be written as:

$$A^{M.D.}_{(J,J')} = \chi' \left[\frac{64\pi\sigma^3}{3(2J+1)hc^3} \right] \beta^2 |\langle f^n \alpha J || \vec{L}+2\vec{S} || f^n \alpha' J' \rangle|^2 \quad . \tag{A-62}$$

For magnetic dipole transitions, the Lorentz field correction term, χ' is defined by (24):

$$\chi' \equiv n^3 \quad . \tag{A-63}$$

The magnetic dipole oscillator strengths and reduced matrix elements, $||\vec{L}+2\vec{S}||$, are tabulated in several publications (18,97).

In the limit of Russell-Saunders coupling, transitions can only occur between J-levels of the ground term and so most strong magnetic dipole transitions are outside the detectable spectral range. However, intermediate coupling can relax the S and L election rules, allowing magnetic dipole transitions in the visible region. Most of these transitions are a minimum of one to two orders of magnitude less intense than forced electric dipole transitions, and are typically only seen when the electric dipole transitions are very weak. An average oscillator strength for the magnetic dipole transition is $\approx 1.0\text{x}10^{-8}$, as compared to $1.0\text{x}10^{-6}$ for electric dipole transitions.

For the evaluation of spectra that consists of both electric dipole and magnetic dipole transitions, it is convenient to have expressions which include both terms. The following expressions have been developed in terms of the Line Strengths (98) The total Oscillator Strength is given by

$$f = \frac{8\pi^2 mc\sigma}{3h(2J+1)} \left[\frac{(n^2+2)^2}{9n} \, S^{e.d.} + n \, S^{M.D.} \right] \tag{A-64}$$

where the Lorentz field corrections and line strengths have been defined previously. Likewise, the Spontaneous Emission Rate appears as:

$$A_{(J;J')} = \frac{64\pi^2 \sigma^3 e^2}{3h(2J+1)} \left[\chi \, S^{e.d.} + \chi' S^{M.D.} \right] . \tag{A-65}$$

Now, the Radiative Lifetime and Branching Ratio of a level J can be defined in terms of the Spontaneous Emission Probability as

$$\left\{1/\tau_J^{rad}\right\} = \sum_{J'} A(J;J') \tag{A-66}$$

and

$$\beta_{JJ'} = A(J;J')/\sum_{J'} A(J;J') \tag{A-67}$$

where the summation is over all terminal levels J'. Finally, two parameters that relate experimentally measurable parameters are the Integrated Absorption Cross-Section

$$\int \sigma(\bar{\nu})d\bar{\nu} = \left(\frac{\pi e^2}{mc^2}\right)\left[\frac{8\pi^2 m\nu}{3h(2J+1)}\right]\frac{1}{n^2}\left[\chi S^{e.d.} + \chi' S^{M.D.}\right] \tag{A-68}$$

where ν is the linewidth in cm^{-1}, and the Peak Induced Emission Cross-Section which is given as

$$\sigma(\lambda_p) = \left(\frac{\lambda_p}{8\pi cn^2\Delta\lambda_{eff}}\right)\left(\frac{64\pi^2\nu^3}{3hc^3(2J+1)}\right)\left[\chi S^{e.d.} + \chi' S^{M.D.}\right] \tag{A-69}$$

where $\Delta\lambda_{eff}$ is the effective linewidth and λ_p is the peak emission wavelength. This concludes the development of the magnetic dipole formalism and its relationship with the electric dipole terms.

Electric Quadrupole Transitions

From electromagnetic theory, it is known that the electric quadrupole operator will have the form of

$$\vec{r} \cdot \vec{r} \approx r^2 \tag{A-70}$$

thus, the matrix elements involving a quadrupole operator between initial and final states appears as:

$$\sim\left|\langle A|r^2|B\rangle\right|^2 . \tag{A-71}$$

It is obvious that transitions between $4f^n$ levels are allowed, since r^2 will provide an even parity term. The solution of the matrix element development parallels quite closely that for the electric dipole terms. In more formal terms, the electric quadrupole operator can be constructed as:

$$\overset{\leftrightarrow}{Q}{}^{(2)}_q = \left(\frac{2}{3}\right)^{1/2} \sum_i r_i^2 \, \overline{C}^{(2)}_i e . \tag{A-72}$$

Once again, the oscillator strength is defined as

$$f^{eq} = \chi\left[\frac{8\pi^2 mc\sigma}{h}\right]\left|\langle A|\overset{\leftrightarrow}{Q}{}^{(2)}_q|B\rangle\right|^2 \tag{A-73}$$

where the expression for χ is assumed to be the same as that for electric dipole transitions:

$$\chi = \frac{n(n^2+2)^2}{9} . \tag{A-74}$$

As with the electric dipole development, it is possible to pull out the radial integral:

$$\int_0^\infty R_{nl}(\bar{r})\, r^2\, R_{n'l'}(\bar{r})dr = \langle nl|r^2|n'l'\rangle . \tag{A-75}$$

For this case, there is no need to mix in the odd components of the crystal field potential, since f→f transitions are now parity allowed. Using the same development from the electric dipole case, the matrix element may be reduced in terms of the angular unit tensor operator and the normalization factor $\overset{\leftrightarrow}{C}{}^{(2)}$:

$$\langle A|\overleftrightarrow{Q}_q^{(2)}|B\rangle = \langle nl|r^2|n'l'\rangle\langle A|\sum_i \bar{C}_i^{(2)}|B\rangle$$

$$= \langle nl|r^2|n'l'\rangle\langle 4f^n \alpha J M_J|\sum_i \bar{C}_i^{(2)}|4f^n \alpha J' M_J'\rangle$$

$$= \langle nl|r^2|n'l'\rangle\langle 4f^n \alpha J M_J|\sum_i \overleftrightarrow{U}_i^{(2)} C'^{(2)}|4f^n \alpha J' M_J'\rangle$$

$$= \langle nl|r'|n'l'\rangle\langle l||C'^{(2)}||l'\rangle\langle 4f^n \alpha J M_J|\vec{U}^{(2)}|$$

$$4f^n \alpha' J' M_J'\rangle \quad . \tag{A-76}$$

Application of the Wigner-Eckart theorem to the matrix element gives

$$\langle 4f^n \alpha J M_J|\overleftrightarrow{U}^{(2)}|4f^n \alpha' J' M_J'\rangle$$

$$= (-1)^{J-M_J}\begin{pmatrix} J & k & J' \\ -M_J & q & M_J' \end{pmatrix}\langle 4f^n \alpha J||\overleftrightarrow{U}^{(2)}||4f^n \alpha' J'\rangle \tag{A-77}$$

where further reduction of the reduced matrix elements yields:

$$\langle 4f^n \alpha J||\overleftrightarrow{U}^{(2)}||4f^n \alpha' J'\rangle$$

$$= (-1)^{S+L'+J+k}\left\{(2J+1)(2J'+1)\right\}^{1/2}\begin{Bmatrix} J & J' & k \\ L' & L & S \end{Bmatrix}$$

$$\langle 4f^n \alpha||\overleftrightarrow{U}^{(2)}||4f^n \alpha'\rangle \quad . \tag{A-78}$$

Carrying out the summation over components gives

$$f^{eq} = \chi\left[\frac{8\pi^2 mc\sigma}{h}\right]\left(\frac{2}{3}\right)(e)^2(1/2J+1)\langle 4f^n \alpha J|\overleftrightarrow{U}^{(2)}||4f^n \alpha' J'\rangle$$

$$= \chi\left[\frac{4\pi^4 mc\sigma}{5he^2}\right]\sigma^2 L\,(\alpha J M_J{}_i\,\alpha' J' M_J')(2J+1)^{-1} \tag{A-79}$$

where, by definition (97)

$$L_q^{1/2}\ (\alpha J M_J;\alpha' J' M_J') = \left(-\frac{2e}{3}\right) \langle 4f^n \alpha J || \Sigma r_i^2 C_i^{(2)} || 4f^n \alpha' J' \rangle \ . \tag{A-80}$$

Further reduction, and transformation to the form including the angular unit tensor operator gives the final form

$$f^{eq} = T_2' \sigma^3 \ \frac{|\langle 4f^n \alpha J || \overleftrightarrow{U}^{(2)} || 4f^n \alpha' J' \rangle|^2}{(2J+1)} \tag{A-81}$$

where

$$T_2' \equiv \left[\frac{16\pi^4 mc}{45h}\right] |\langle 1||C'^{(2)}||1'\rangle|^2 |\langle nl|r^2|n'l'\rangle|^2 \ \chi \ . \tag{A-82}$$

It is possible to follow the same formalism to develop the line strengths and other terms, but they play no useful roll in evaluating the spectra of rare earth doped materials. At the present time, there have been no true direct electric quadrupole transitions observed in the rare earth spectra. However, from theoretical estimates (87), the oscillator strengths for electric quadrupole transitions should be of the order:

$$f^{eq} \simeq 2 \times 10^{-9} \ . \tag{A-83}$$

This weak of a transition would be highly difficult to detect and label.

Conclusions

From the information given in this Appendix, I would hope that this has provided an enlightenment into the possibilities of predicting theoretically how the different experimentally measurable parameters should appear. Many spectroscopists publish papers on rare earth spectra with the Judd-Ofelt parameters included, and, for most ions,

there is actually very good agreement between theory and experiment. Also, this formalism is fairly easy to use since all parameters can be computed from basic absorption and fluorescence spectra, and, the theoretical predictions can be calculated using a Gaussian fitting program. The basics of the Judd-Ofelt theory are most important to all spectroscopists dealing with rare earth compounds.

VITA

GREGORY JAMES QUARLES

Candidate for the Degree of

Doctor of Philosophy

Thesis: LASER SPECTROSCOPIC STUDIES OF EUROPIUM-DOPED GLASSES AND EMERALD

Major Field: Physics

Biographical:

Personal Data: Born in Tulsa, Oklahoma, May 11, 1961, the son of Rodger L. and Darlene E. Quarles. Married to Connie M. Dickson on August 7, 1982, with one child, Brandon J. Quarles.

Education: Graduated from Skiatook High School, Skiatook, Oklahoma, in May, 1979; received Bachelor of Science degree from Oklahoma State University in December, 1983, with a double major in Physics and Mathematics; received Master of Science degree from Oklahoma State University in May, 1985; completed the requirements for the Doctor of Philosophy degree at Oklahoma State University in December, 1987.

Professional Experience: Undergraduate Laboratory and Lecture Demonstration Assistant, Oklahoma State University, August 1980 to May, 1981; Undergraduate Intern Position, Phillips Petroleum Company, May, 1981 to August, 1981; Undergraduate Research Assistant, Oklahoma State University, August, 1981 to May, 1983; American Physical Society Summer Intern, IBM May, 1983 to August, 1983; Undergraduate Research Assistant, Oklahoma State University, August, 1983 to December, 1983; Graduate Research Assistant, January, 1984 to present. Air Force Weapons Laboratory Graduate Research Fellow, August, 1986 to present; Member of the American Physical Society, Optical Society of America, and Sigma Xi.